Weighted Sliding Empirical Mode Decomposition and its Application to Neuromonitoring Data

Dissertation

zur Erlangung des Doktorgrades
der Naturwissenschaften (Dr. rer. nat.)
der Naturwissenschaftlichen Fakultät II - Physik -
der Universität Regensburg

vorgelegt von

Angela Zeiler

aus Weiden

im Jahr 2012

Promotionsgesuch eingereicht am 18. Dezember 2012.

Die Arbeit wurde durchgeführt am Institut für Biophysik
und physikalische Biochemie unter der Anleitung von
Prof. Dr. Elmar W. Lang.

In Zusammenarbeit mit der Klinik und Poliklinik für
Neurochirurgie des Universitätsklinikums Regensburg
unter Anleitung von Prof. Dr. Alexander Brawanski

Prüfungsausschuss:

Vorsitzender : Prof. Dr. Josef Zweck
1. Gutachter : Prof. Dr. Elmar W. Lang
2. Gutachter : Prof. Dr. Alexander Brawanski
3. Gutachter : Prof. Dr. Thomas Niehaus

Contents

1 Introduction **1**

2 Biomedical Background **5**

2.1 Physiological Fundamentals of Severe Brain Trauma 5

2.2 Neuromonitoring 7

2.2.1 Partial Oxygen Pressure in Brain Tissue 8

2.2.2 Intracranial Pressure 9

2.2.3 Arterial Blood Pressure 9

3 Empirical Mode Decomposition **11**

3.1 The Principle of EMD 12

3.2 Hilbert-Huang Transform 13

3.3 Mathematical Properties 15

3.3.1 Completeness 16

3.3.2 Orthogonality 16

3.3.3 Uniqueness 17

3.3.4 Linearity and Stationarity 17

3.4 Implementation and Properties of EMD 18

3.4.1 Requirements of the Data 18

3.4.2 Variable Methods of the EMD Implementation 21

3.4.3 Range of the Boundary Artifacts 24

3.4.4 Shortcomings of EMD 27

3.5 Recent Extensions to EMD 28

3.5.1 Ensemble EMD 29

3.5.2 Local EMD 30

3.5.3 On-line EMD 32

4 Sliding Empirical Mode Decomposition **33**

4.1 The Principle of SEMD 34

4.2 Properties of SEMD . . . 37
4.3 Weighted Sliding EMD . . . 39
4.3.1 Weighted Estimates Sliding EMD . . . 39
4.3.2 Weighted Window Sliding EMD . . . 39
4.4 Comparison between weSEMD and wwSEMD . . . 41
4.4.1 Implementation of the Weighting Processes . . . 42
4.4.2 Example of Weights used for weSEMD and wwSEMD . . . 44
4.4.3 Comparison between the Performance of weSEMD and wwSEMD . . . 45
4.4.4 Difficulties of Weighted Estimates SEMD . . . 48

5 Application of wSEMD to Toy Data 57
5.1 Toy Data . . . 58
5.2 Completeness and Numerical Accuracy . . . 58
5.3 Examination of the IMF Criteria . . . 59
5.3.1 Mean Value . . . 59
5.3.2 Number of Extrema and Zero Crossings . . . 61
5.4 Influence of Window and Step Size . . . 61
5.5 Influence of the Window Size on the Oscillations in the Residuum . . . 64
5.6 Performance Evaluation . . . 65
5.7 Computational Load . . . 67
5.7.1 Ensemble Size . . . 67
5.7.2 Data Length . . . 69

6 Application of wSEMD to Homeostatic Brain Status Data 73
6.1 Data Set . . . 74
6.2 Multi-Taper Method . . . 75
6.3 Completeness and Numerical Accuracy . . . 76
6.4 Selecting the Window Size . . . 76
6.4.1 Mean Reconstruction Error between Residuum and Original Data . . . 77
6.4.2 Toy Data Experiment . . . 78
6.4.3 Medical Data . . . 79
6.5 Significance Test for Correlation Coefficients . . . 80
6.5.1 Variation of the Segment Size . . . 82
6.5.2 Variation of the Significance Limit . . . 83
6.6 Analyzing Neuromonitoring Time Series . . . 84

6.6.1 Comparison to MTM Analyses . . . 85
6.6.2 Analysis of the Segment Size . . . 88
6.6.3 Correlations in Neuromonitoring Data . . . 90

7 Application of wSEMD to Pulsatile Brain Status Data 93
7.1 Data Set . . . 94
7.2 Singular Spectrum Analysis Preprocessing . . . 94
7.2.1 The Principle of SSA . . . 95
7.2.2 SSA Parameters . . . 97
7.2.3 SSA Applied to Brain Status Data . . . 102
7.3 Completeness and Numerical Accuracy . . . 103
7.4 Examination of the IMF Criteria . . . 104
7.4.1 Mean Value . . . 105
7.4.2 Number of Extrema and Zero Crossings . . . 105
7.5 Influence of the Ensemble Size . . . 108
7.6 Separating Heartbeat and Breathing Mode . . . 111
7.6.1 Arterial Blood Pressure . . . 111
7.6.2 Intracranial Pressure . . . 114
7.6.3 Analysis of the Separability . . . 116
7.7 Examination of the Heartbeat Amplitude . . . 122
7.7.1 Amplitude of the Heartbeat Periods . . . 122
7.7.2 Mean Amplitude of the Heartbeat . . . 126

8 Conclusion and Outlook 129

Bibliography 134

Chapter 1

Introduction

The human brain is a remarkable organ: Although it only amounts to about 2 % of the body weight of an adult, it consumes around 20 % of the incorporated oxygen and 25 % of the glucose. As the brain tissue is not able to store those vitally important substances, a sufficient supply, and thus the cerebral blood flow, has to be maintained permanently. Even a short interruption of the cerebral perfusion can lead to brain damage.

Several regulatory mechanisms in the human brain help ensuring an adequate provision of oxygen and glucose over a wide blood pressure range. However, a severe traumatic brain injury can partially or even completely suspend them, causing an altered reaction of the brain to therapeutic procedures.

In intensive care units during the so-called *neuromonitoring* different brain status parameters of patients with a dangerous concussion are measured, which may allow to draw conclusions about the functionality of the regulatory mechanisms and the general state of the patient. The neuromonitoring time series include recordings of, amongst others, the partial oxygen pressure in brain tissue (TPO), the intracranial pressure (ICP) and the arterial blood pressure (ABP). The physiology of a severe brain trauma and the neuromonitoring data and sensors will be described in detail in chapter 2.

By means of the recorded data an insufficient supply of the brain is supposed to be recognized as early as possible before irreversible brain damage emerges. Furthermore, the data may allow for a judgment on the individual reaction of a patient to therapeutic treatments and effects can be avoided, which would hinder the recovery. Yet, the increasing intensity of neuromonitoring leads to a load of data. Their interpretation challenges the attending physician, due to the complexity of the cerebral physiology and the partly nonlinear coupling of the individual parameters [1].

Thus, present-day intensive care attempts to extract medically relevant information from the data by means of suitable time series analysis techniques and consequently to facilitate the interpretation of cerebral dynamics. Real data recordings are always afflicted with noise which is to be removed. In addition it is adjuvant to decompose the brain status data into their underlying modes, with which it is possible to make statements about the brain.

The main difficulty of the analysis constitutes the fact that biomedical data mainly consist of nonlinear and nonstationary time series. The application of common analysis methods to these data may be problematic due to their nonstationarity. Hence, in this thesis *Empirical Mode Decomposition* (EMD) is used, which will be described in detail in chapter 3. EMD, which was recently developed by Norden E. Huang, is a new and adaptive data analysis method, that is able to decompose nonlinear and nonstationary data into so-called Intrinsic Mode Functions (IMFs), since the algorithm is based on the local properties of the time series. Empirical Mode Decomposition has been successfully applied to data in the medical field [2, 3, 4, 5, 6, 7]. Therefore, EMD will be applied to the neuromonitoring data sets in this thesis.

One of the problems concerning time series analysis arises as the information contained in the brain status data is generally found on very diverse time scales. In order to be able to investigate upon the heartbeat or breathing mode, the parameters have to be recorded with a high sampling rate. Additionally, processes lasting minutes, like the so-called Mayer waves, or low-frequency, often non-stationary, nonlinear oscillations lasting for several hours or even days, have to be observed to gain information about the patient's status. This yields the problem of extensive amounts of data one is forced to deal with.

Conventional analysis tools are not able to deal with those massive quantities of time series and cannot analyze the entire data in acceptable time for practical applications. Moreover, it is essential for the medical care of the patients to conduct data acquisition and processing simultaneously, since the results are needed instantly. Real-time analysis is necessary for the patients in intensive care units as they usually reside in a critical condition. That way diagnoses can quickly be provided and therapeutic interventions seized during the recording when modifications of the monitored parameters occur.

On this account a new method the so-called *Sliding Empirical Mode Decomposition* (SEMD) will be introduced in chapter 4 together with an improved version, namely *weighted Sliding Empirical Mode Decomposition* (wSEMD), in which the suppression of so-called boundary artifacts is enhanced. The presented new approaches offer

the possibility to use Empirical Mode Decomposition – in contrast to the original technique – for time series of arbitrary duration in an *online* modality and, thereby, allows for real-time analysis.
In chapter 5 the new methods SEMD and wSEMD are applied to toy data examples to evaluate their functionality, properties and performance. The adherence of the algorithms to the basic principles of the original method is tested and additionally, an examination of their computational demand is performed.
Chapters 6 and 7 finally provide the applications of wSEMD to brain status data acquired during neuromonitoring in the Department of Neurosurgery of the University Hospital Regensburg.
On the one hand the property of wSEMD to serve as a low-pass filter is used to extract slowly varying oscillations from the brain status data in chapter 6, in order to diagnose brain swelling as early as possible via correlations between the different time series of the neuromonitoring data sets. With the aid of a mathematical model [8, 9] it can be shown that correlations will occur, if certain cerebral regulatory systems start to fail. This may disturb the cerebral perfusion severely and, hence, has to be detected promptly. Up to now this can only be done reliably by repetitive CT-scans, a very stressful procedure for the instable patient. A recent method based on Fast Fourier Transform [10] detects such interdependencies but has a crucial drawback as it needs more than 2.8 hours of observation time for the detection. The use of wSEMD drastically reduces the amount of monitoring time, demanded to detect the correlations.
After a preprocessing with Singular Spectrum Analysis to remove noise, in chapter 7 wSEMD is, on the other hand, utilized to decompose neuromonitoring time series to extract oscillations like the heartbeat and breathing mode. These oscillations are of interest for numerous further investigations since they are featured in the arterial blood pressure and the intracranial pressure time series of the neuromonitoring data set and promise to uncover the underlying processes and modalities in the brain. Therefore, a closer look will be taken on the heartbeat mode and its development over time.

The work in this thesis was conducted in close collaboration with the Department of Neurosurgery of the University Hospital Regensburg.

Chapter 2

Biomedical Background

In this chapter a short overview of the physiological fundamentals of the human brain in case of a severe head trauma will be given. Different cerebral regulatory mechanisms, to maintain its vital functions, will be described in this context. Thereby, the selection and significance of those parameters will be presented, that are recorded during neuromonitoring. In addition, the basic physical principles of the measurement of the cerebral partial oxygen pressure (TPO), the intracranial pressure (ICP) and the arterial blood pressure (ABP) will be explained in the following. Furthermore, some characteristics of the recorded data will be analyzed.

2.1 Physiological Fundamentals of Severe Brain Trauma

Since the human brain consumes a large amount of glucose and oxygen and is not able to store those substances, an adequate blood supply has to be maintained constantly. Interruptions of the cerebral perfusion can result in severe damage of the brain tissue. Diverse cerebral regulatory mechanisms help to support a sufficient supply of the vital substances over a wide blood pressure range. Yet, it is possible that those mechanisms can partially or completely be suspended by a traumatic brain injury.

An example for such a regulatory system is the so-called cerebral autoregulation. The blood flow is not to fall underneath a certain, individual boundary, which is also dependent on the momentary demand of glucose and oxygen of the human brain. Therefore, it is regulated autonomously via constriction and dilation of the arteries and arterioles to keep an appropriate blood flow over a wide blood pressure range.

Because the arteries and arterioles have a muscular layer unlike any other type of blood vessel, they can change their diameter actively to control the blood flow. In case of a raising blood pressure the vascular resistance is enlarged by constricting the vessels and vice versa. However, the change in diameter, and as a result the autoregulation, is limited. If the maximal variation is obtained, it will not be possible to actively alter the blood flow further. A failure of this regulatory mechanism can have a vast impact on the treatment of a patient and therefore has to be detected as soon as possible.

The cerebrospinal fluid flow represents another cerebral regulatory system that helps to stabilize the intracranial pressure. The cerebrospinal fluid (CSF) itself is produced in the ventricles at the center of the brain, whereby the amount depends on the pressure gradient between the ABP and ICP. At the upper part of the brain, where a vein called sinus sagittalis superior is located, the main part of the CSF is reabsorbed. In figure 2.1 the whole CSF circulation is pictured. The reabsorption is also a passive process and functions through a pressure gradient between the CSF and the venous blood. An increase of the ICP can be diminished by this reduction of CSF volume. Therefore, in case of an increasing intracranial pressure the CSF production is reduced and the CSF absorption is enhanced. This regulatory mechanism helps stabilizing the intracranial pressure. However, if the CSF is completely depleted, for example in case of a brain swelling, further adjustment will no longer be possible.

The driving force of both circulations – blood and CSF flow – is the heart, respectively, the heartbeat.

To better understand the human brain and its behavior in case of a traumatic brain injury a mathematical model has been developed by the Computational Intelligence and Machine Learning Group of the University of Regensburg in cooperation with the Department of Neurosurgery at the University Hospital Regensburg. With the help of this model [8, 9] it could be shown that correlations between the low-frequency oscillations of the arterial blood pressure (ABP), the intracranial pressure (ICP) and the cerebral partial oxygen pressure (TPO) (for details see section 2.2) will appear, if the cerebral regulatory mechanisms are failing. Particularly a negative correlation between the ABP and ICP and the TPO and ICP indicates a diminished cerebral compliance caused by a severe brain swelling (see [8] for details). From a model point of view, the occurrence of these interdependencies can only be reproduced, if the CSF compartment is completely depleted, due to a swelling, and the autoregulation mechanism is restricted.

Such a lesion may alter the cerebral perfusion and has to be detected as early as possible which, up to now, can only be done dependably by repetitive CT-scans.

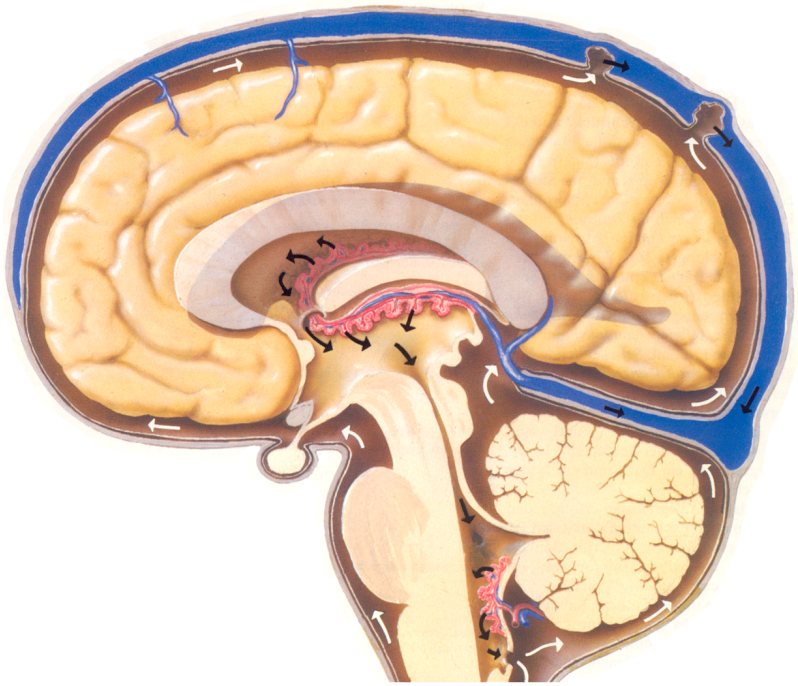

Figure 2.1 Cerebrospinal fluid is produced in the ventricles located at the center of the brain. Most of the produced CSF flows upwards and is absorbed mainly in the sagittal sinus, a big venous blood vessel at the top of the brain. The rest flows downwards the spinal cord (adapted from [11]).

However, this constitutes a very stressful procedure for the, mostly instable, patients. Faltermeier *et al.* [10] presented a method based on Fast Fourier Transform to reliably find such correlations within the data. The drawback of this approach is, however, that it needs more than 2.8 hours of monitoring time for the detection. In this thesis an alternative approach to detect interdependencies within the data with a higher temporal resolution will be presented (see chapter 6).

2.2 Neuromonitoring

In neurosurgical intensive care it meanwhile is state of the art to monitor patients with severe brain trauma thoroughly via measurement of different brain status parameters, which is called multimodal neuromonitoring. Such neuromonitoring primarily focuses on: first, the oxygen supply of the brain tissue, through the cerebral partial oxygen pressure. Second, the intracranial pressure and the arterial blood pressure, which are recorded continuously and with a high sampling rate characterizing the cerebral hemodynamics.

The time series may include high-frequency, stationary, nonlinear parts, e.g. the heartbeat and the breathing mode and low-frequency, often nonstationary, nonlinear oscillations. The slowly oscillating modes or the trend of the data mostly reflect the homeostasis of a person. The homeostasis signifies the ability of the body to adapt to external factors or circumstances by regulation of its physiology to sustain a stable state. In the following the measured variables relevant for this thesis are described.

2.2.1 Partial Oxygen Pressure in Brain Tissue

The partial oxygen pressure in brain tissue ($TiPO_2$ or TPO) which corresponds to the oxygen supply of the brain is measured with a Licox sensor placed about 2.7 cm deep into the brain tissue. It detects the amount of available oxygen for the nerve cells, which they receive by diffusion from the capillary blood. That makes the partial oxygen pressure directly proportional to the available oxygen for the cells. The functionality of the sensor is based on a polarographic Clark-type probe placed into the frontal part of the brain. The oxygen diffuses – depending on its partial pressure – through a diffusion membrane (a polyethylene tube) into the inner chamber. Inside of the sensor a silver anode and a gold cathode are located and connected via a KCl electrolyte solution with a voltage of 0.8 V applied. The oxygen is reduced at the cathode and therefore an electric current flows – proportional to the oxygen concentration in the electrolytic chamber – based on the following chemical reaction:

- $O_2 + 2\,H_2O + 4\,e^- \rightarrow 4\,OH^-$
- $4\,Ag + 4\,Cl^- - 4\,e^- \rightarrow 4\,AgCl$

For every O_2 molecule a current of four electrons occurs. In figure 2.2 the basic configuration of a Licox sensor is depicted.
The recorded values depend on the temperature due to the type of the sensor. More oxygen is able to enter the probe, as the permeability of the membrane increases with temperature. In order to be able to compensate this effect the temperature is measured simultaneously by the Licox probe. A temperature compensation is applied to the monitored values to avoid a systematic error.
The surface of the diffusion membrane of a Licox sensor typically amounts to 14 mm^2, therefore the contribution of thousands of capillaries are measured assuming a capillary density of around 300-1000 capillaries/mm^3. Though monitoring an average partial oxygen pressure, one can only speak of the monitoring of a local $TiPO_2$, considering the size of the human brain. Normal values for the partial oxygen pressure

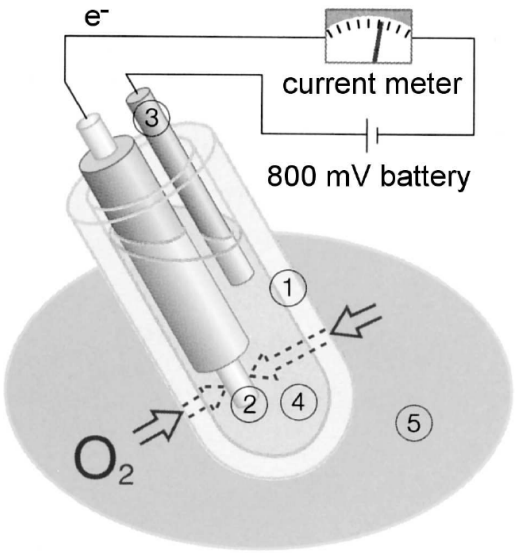

Figure 2.2 The Licox sensor consists of: (1) polyethylene diffusion membrane, (2) gold cathode, (3) silver anode, (4) electrolytic chamber with KCl and (5) brain tissue (figure adapted from Gesellschaft für Medizinische Sondentechnik).

of the brain lie between 25 mmHg and 40 mmHg. A critical situation for the patient emerges for values below 10 mmHg [12].

2.2.2 Intracranial Pressure

To continuously measure the intracranial pressure (ICP), a sensor is inserted into the brain tissue in a depth of around 1 - 2 cm. The measurement is done using the piezoresistive effect. Therefore, after calibration with the external air pressure, the piezo element with a membrane attached to it is exposed to the brain tissue. The resulting pressure and therefore potential difference indicates the ICP value. ICP values typically range between 5 mmHg and 20 mmHg, however values over 40 mmHg are presumed to be dangerous [12].

2.2.3 Arterial Blood Pressure

The arterial blood pressure (ABP) accounts for the blood pressure monitored in a central artery. Equivalent to the ICP it is measured via a piezo element after the calibration with the external air pressure. In intensive care units of hospitals the arterial blood pressure is usually recorded with a very high sampling rate. The high resolution ABP curve can adopt values between 60 mmHg and 200 mmHg [12].

Chapter 3

Empirical Mode Decomposition

Empirical Mode Decomposition (EMD) was pioneered by Norden E. Huang *et al.* [13] in 1998 as an adaptive time series analysis method. EMD is designated for the analysis of nonlinear and nonstationary data. The method was developed from the assumption that any time series consists of different simple intrinsic modes of oscillation, called Intrinsic Mode Functions (IMFs). The essence of the method is to empirically identify these intrinsic oscillatory modes by their characteristic time scales in the data, and then decompose the data accordingly. The empirical nature of EMD offers the advantage over other signal decomposition techniques of not being constrained by conditions, which often only apply approximately.

Since EMD was originally developed to provide suitable functions for the Hilbert transform, the latter will additionally be introduced in the following. The Hilbert transform of the IMFs, called Hilbert-Huang transform, offers exact time-frequency spectra and their related instantaneous amplitudes and energies. This could offer new insights since most classical time series analysis methods are not prepared to deal with nonstationary signals.

After presenting the working principle of Empirical Mode Decomposition and, additionally, the Hilbert-Huang transform, the mathematical properties of EMD will be discussed in the following. In addition, implementation details and variants of the algorithm as well as properties of the method are discussed. Presented are, moreover, a few shortcomings, above all, errors corrupting the decomposition at the borders of the time series stemming from boundary artifacts. Furthermore, an overview over recent extensions of Empirical Mode Decomposition, e.g. Ensemble Empirical Mode Decomposition [14] and on-line EMD [15], will be given in this chapter.

3.1 The Principle of EMD

The EMD algorithm considers signal oscillations at a very local level and separates the data into locally non-overlapping, zero-mean, stationary time scale components by the so-called sifting process. It is designated for the analysis of nonlinear and non-stationary time series. The method assumes that any data is composed of different simple oscillations called Intrinsic Mode Functions (IMFs). EMD is a heuristic technique based on the properties of the data on a local scale and represents a fully data-driven, unsupervised signal decomposition without the need of an *a priori* defined basis system, in which the signal is expressed. Via the constrain to have a zero-mean, so-called riding waves, i.e. oscillations with no zero crossing between the extrema can be eliminated, rendering the wave profiles more symmetric. EMD breaks down a signal $x(t_n)$ into its component Intrinsic Mode Functions, obeying two properties:

1. An IMF has only one extremum between two subsequent zero crossings, i.e. the number of local extrema and zero crossings differs at most by one.

2. The local average of the upper and lower envelopes of an IMF has to be zero.

Note that the second condition may imply that an IMF is stationary, as long as the local mean estimation with envelopes does not deviate from the true local mean. Dealing with stationary data simplifies their analysis. But an IMF may have amplitude modulation and also changing frequency as is shown in figure 3.1. However, riding waves are excluded.

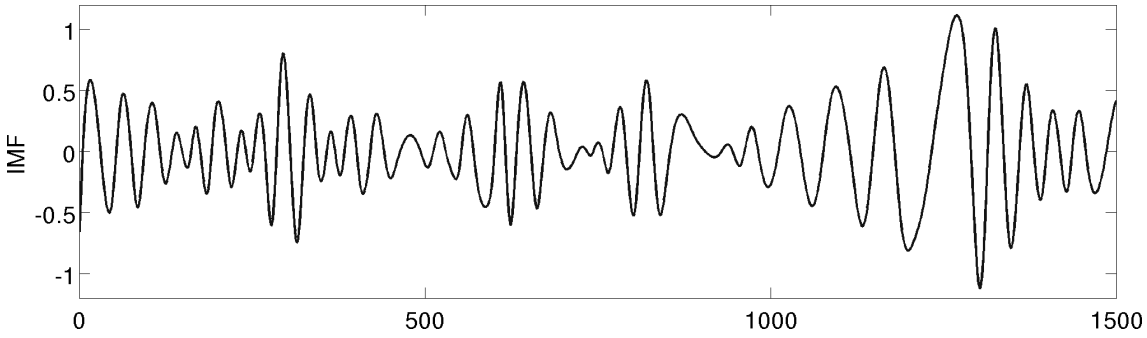

Figure 3.1 Illustration of an Intrinsic Mode Function with amplitude and frequency modulation but no riding waves.

The sifting process locally filters pure oscillations, starting with the highest frequency oscillation in an iterative procedure [13]. Hence, the sifting algorithm decomposes a data set $x(t_n)$ into $l = 1, \ldots, L$ individual IMFs denoted by $x_l(t_n)$ and

a residuum $r(t_n)$, which is the monotonic or non-oscillating trend of the data, such that the signal can be represented as

$$x(t_n) = \sum_l c_l(t_n) + r(t_n) \tag{3.1}$$

The index n indicates that t_n consists of n discrete samples, which applies generally in this thesis.
The sifting process can be summarized in the following algorithm:

- Step 0: Initialize $l := 1$ and $r_0(t_n) = x(t_n)$
- Step 1: Extract the l-th IMF as follows:
  a) Set $h_0(t_n) := r_{l-1}(t_n)$ and $k := 1$
  b) Identify all local maxima and minima of $h_{k-1}(t_n)$
  c) Construct, by cubic splines interpolation, for $h_{k-1}(t_n)$ the envelope $U_{k-1}(t_n)$ defined by the maxima and the envelope $L_{k-1}(t_n)$ defined by the minima
  d) Determine the mean $m_{k-1}(t_n) = \frac{1}{2}\big(U_{k-1}(t_n)+L_{k-1}(t_n)\big)$ of both envelopes of $h_{k-1}(t_n)$. This running mean is called the low-frequency local trend.
  e) Form the k-th component $h_k(t_n) := h_{k-1}(t_n) - m_{k-1}(t_n)$
     1) If $h_k(t_n)$ is not in accord with all IMF criteria, increase $k \to k+1$ and repeat the sifting process starting at step (b)
     2) If $h_k(t_n)$ satisfies the IMF criteria then set $c_l(t_n) := h_k(t_n)$ and $r_l(t_n) := r_{l-1}(t_n) - c_l(t_n)$
- Step 2: If $r_l(t_n)$ represents a residuum, stop the sifting process; if not, increase $l \to l+1$ and start at step 1 again.

The sifting process is illustrated for convenience in figure 3.2. Note that the number of IMFs extracted from a time series is roughly equal to $L \approx \log_2 N$ with N denoting the number of samples of the time series [14].

3.2 Hilbert-Huang Transform

After having extracted all IMFs $c_l(t_n)$, they can be analyzed further by processing them in any other suitable way or applying the Hilbert transform [16, 17]. The

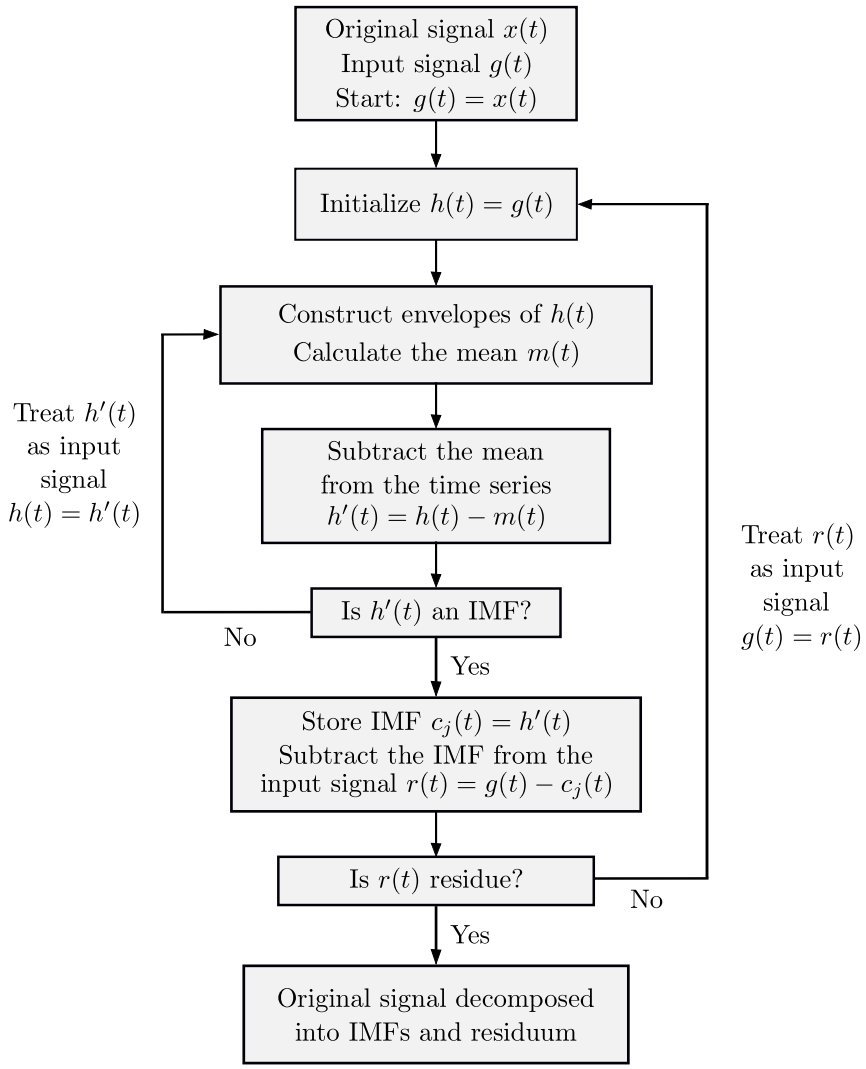

Figure 3.2 Flow diagram of the EMD algorithm

Hilbert transform of the time series $c_l(t_n)$ is defined as [13]:

$$H\{c_l(t_n)\} = \frac{1}{\pi} P \left\{ \int_{-\infty}^{\infty} \frac{c_l(\tau)}{(t_n - \tau)} d\tau \right\} \tag{3.2}$$

where P indicates the Cauchy principal value. This way an analytical signal $z_l(t_n)$ can be defined as

$$z_l(t_n) = c_l(t_n) + iH\{c_l(t_n)\} = a_l(t_n) \exp\left(i\theta_l(t_n)\right) \tag{3.3}$$

with amplitude $a_l(t_n)$ and instantaneous phase $\theta_l(t_n)$ given by

$$a_l(t_n) = \sqrt{c_l^2(t_n) + H\{c_l(t_n)\}^2} \tag{3.4}$$

$$\theta_l(t_n) = \arctan\left(\frac{H\{c_l(t_n)\}}{c_l(t_n)}\right) \tag{3.5}$$

The instantaneous frequency $\omega_l(t_n)$ of the signal can be obtained by the derivative of the instantaneous phase

$$\omega_l(t_n) = \frac{d\phi_l(t_n)}{dt_n} \tag{3.6}$$

The combination of EMD decomposition of a signal into its IMFs plus residuum and a subsequent Hilbert spectral analysis to extract instantaneous frequencies and phases is called Hilbert-Huang transform (HHT) [18, 19].

Hilbert-Huang Transform vs. Fourier Transform

After the Hilbert-Huang transform each IMF can now be expressed as

$$c_l(t_n) = Re\left[a_l(t_n)\exp\left(i\int \omega_l(t_n)dt_n\right)\right] \tag{3.7}$$

The signal can then be written as

$$x(t_n) = Re\left\{\sum_{l=1}^{L} a_l(t_n)\exp\left(i\int \omega_l(t_n)dt_n\right)\right\} + r(t_n) \tag{3.8}$$

An IMF expansion, thus, provides a generalized Fourier expansion.
Compared with a Fourier representation with constant a_l and fixed ω_l

$$x(t_n) = \sum_{l=1}^{\infty} a_l \exp\left(i\omega_l t_n\right) \tag{3.9}$$

the time-dependent amplitude and instantaneous frequency clearly constitute an advantage. A Fourier transform, however, decomposes any time series into simple harmonic components with globally constant amplitudes and frequencies.

3.3 Mathematical Properties

Empirical Mode Decomposition is completely determined by its algorithm as no mathematical basis of the method exists yet. The mathematical properties of EMD,

namely completeness, orthogonality and uniqueness, can therefore only be reviewed numerically. In this context a short overview of the terms linearity and stationarity are given.

3.3.1 Completeness

Completeness of the decomposition process is automatically achieved by the algorithm as

$$x(t_n) = \sum_{l=1}^{L} c_l(t_n) + r(t_n) \tag{3.10}$$

represents an identity. Completeness can also easily be proven numerically by reconstruction. If the sum of all extracted IMFs is subtracted from the original signal, for a complete decomposition, the reconstruction error will normally yield

$$\epsilon = x(t_n) - \sum_{l=1}^{L} c_l(t_n) + r(t_n) \leq 10^{-14} \tag{3.11}$$

as is stated in [13].

3.3.2 Orthogonality

The EMD algorithm produces locally orthogonal IMFs [13]. However, orthogonality cannot be guaranteed theoretically but is often met in practice. Global orthogonality is not warranted as neighboring IMFs might have identical frequencies at different points in time (typically in less than 1% of the cases [13]).
Orthogonality can be tested numerically [13]. To test this a posteriori, simply rewrite the data decomposition according to

$$x(t_n) = \sum_{l=1}^{L} c_l(t_n) + r(t_n) = \sum_{j=1}^{L+1} X_j(t_n) \tag{3.12}$$

Next, consider the square of the signal

$$x^2(t_n) = \sum_{j=1}^{L+1} X_j^2(t_n) + 2 \sum_{j=1}^{L+1} \sum_{k=1}^{L+1} X_j(t_n) X_k(t_n) \tag{3.13}$$

If the basis is orthogonal, all terms in the second part of the right hand side with different indices should vanish. Thus, the overall index of orthogonality IO is defined

as:

$$IO = \sum_{t_n=1}^{N} \left(\sum_{j=1}^{L+1} \sum_{k=1}^{L+1} X_j(t_n) X_k(t_n) / x^2(t_n) \right) \tag{3.14}$$

3.3.3 Uniqueness

The resulting Intrinsic Mode Functions of a decomposition are deterministic as long as all the modalities and implementation variants of the EMD algorithm are kept constant, respectively, are not changed. Altering parts of the algorithm like the stopping criterion or the boundary condition (described in section 3.4.2) generally produces quantitatively but not qualitatively different results.

3.3.4 Linearity and Stationarity

In the context of the mathematical properties of Empirical Mode Decomposition also a short overview of the terms linearity and stationarity is provided, since they will be used very often in this thesis.

Linear Systems

A linear system follows a linear superposition principle, i.e. the following relation $f(t) + g(t)$ describes a linear system despite $f(t)$ and $g(t)$ being nonlinear functions of the variable t [20].
Most natural systems, like biomedical time series, are nonlinear and can only approximately be represented by a linear system. However, EMD can deal with nonlinear data.

Stationarity

A time series of a random variable $X(t)$

$$X(t) = [X(t_0), X(t_1), \ldots, X(t_{N-1})] \tag{3.15}$$

is called strongly stationary if the joint probability

$$P(X(t)) = P(X(t_N - t_{N-1}, \ldots, t_1 - t_0)) \tag{3.16}$$

does not depend on time t itself but only on time differences $\tau = t_{n+1} - t_n \; \forall \; n = 0, \ldots, N-1$ [20]. Correspondingly, a time series is called weakly or wide-sense stationary if every data point has a finite variance. That means $E(|X(t)^2|) < \infty$,

the mean is constant everywhere, so $E(X(t)) = m$ and the covariance only depends on τ, i.e.

$$cov(X(t_1), X(t_2)) = cov(X(t_1), X(t_1 + \tau)) = cov(X(0), X(\tau)) \tag{3.17}$$

Weak stationarity, thus, only requires the first (mean) and second (variance) moment of the data distribution $P(X(t))$ to be constant at all times.

Real physical data sets, like neuromonitoring data, usually do not fulfill such conditions because of noise and/or transient signal components. One of the great advantages of EMD is, that nonstationary signals can be decomposed without difficulty by the algorithm. Furthermore, the resulting Intrinsic Mode Functions can be considered stationary, as long as the local mean estimated by the envelopes does not deviate from the true local mean.

3.4 Implementation and Properties of EMD

For Empirical Mode Decomposition to work properly some requirements have to be fulfilled by the data. Obtaining good results in terms of amplitude and frequency resolution requires certain conditions to be met. As a heuristic decomposition method the EMD algorithm leaves room for variable implementation variants. They ask for some care in using them properly and will briefly be discussed in this section. Additionally, the configuration of the user-defined components of the algorithm implemented in the Empirical Mode Decomposition and employed in this thesis will be presented, whereby the algorithm itself is based on [21]. Furthermore, the artifact range of the IMFs stemming from the boundary effects will be analyzed in the following. It will demonstrate how much of a time series is defected because of the boundary artifacts arising at the ends of the data and some shortcomings of EMD will be explained.

3.4.1 Requirements of the Data

Among the demands concerning the decomposability with EMD are the sampling rate of the time series, the frequency content and the amplitudes of the signal components. Those requisites for a satisfactory signal decomposition will be discussed shortly.

Sampling

The calculation of the local mean is based on the correct detection of the extrema as knots for the spline interpolation. The sampling rate must follow the Nyquist theorem and the digitalized signal should have the same number of extrema as its continuous counterpart. Additionally, for good results, the Hilbert transform needs at least 5 samples per (shortest) period [13]. Over-sampling improves the results considerably, as it is more likely that the exact location of the extrema is met by the discrete signal. In [22, 23] a quantitative analysis of the influence of different sampling rates on the decomposition results is applied.

Frequency

Concerning frequency resolution, EMD behaves like a dyadic filter bank [24, 25, 26]. Filters overlap and the number of extrema will be reduced by one half from one IMF to the next, if EMD is applied to white noise. Rilling *et al.* [15, 27] showed empirically applying EMD to a toy signal

$$f(t_n) = a_i \cos(2\pi \cdot \omega_i \cdot t_n) + a_j \cos(2\pi \cdot \omega_j \cdot t_n) \tag{3.18}$$

that for every signal frequency ω_i exists a frequency band

$$B(\omega_i) = [\alpha_\rho \omega_i, \omega_i]$$
$$0 < \alpha_\rho < 1 \quad \text{and} \quad \rho = a_i/a_j$$

which is dependent on the amplitude quotient ρ of the signals, with a_i and a_j being the signal amplitudes, such that every frequency $\omega_j \in B(\omega_i)$ is indistinguishable from ω_i, hence, cannot be resolved. If two frequencies are filtered by the same filter, they will be represented by the same IMF.
In figure 3.3 an example for mode mixing caused by two signals, which feature too similar frequencies, is shown. The time series consists of two sinusoid components:

- $x_1(t_n) = \sin(8 \cdot t_n)$
- $x_2(t_n) = \cos(0.4 \cdot t_n^2)$

with $t_n = 0, \ldots, 19.9995$, a step of $\Delta t_n = 0.0005$ between the samples and a total of $N = 40\,000$ data points. The second original mode $x_2(t_n)$ changes its frequency depending on time. Thus, in the middle part of the time series the local frequen-

cies of both components are alike and mode mixing appears, since they cannot be distinguished by the EMD algorithm.

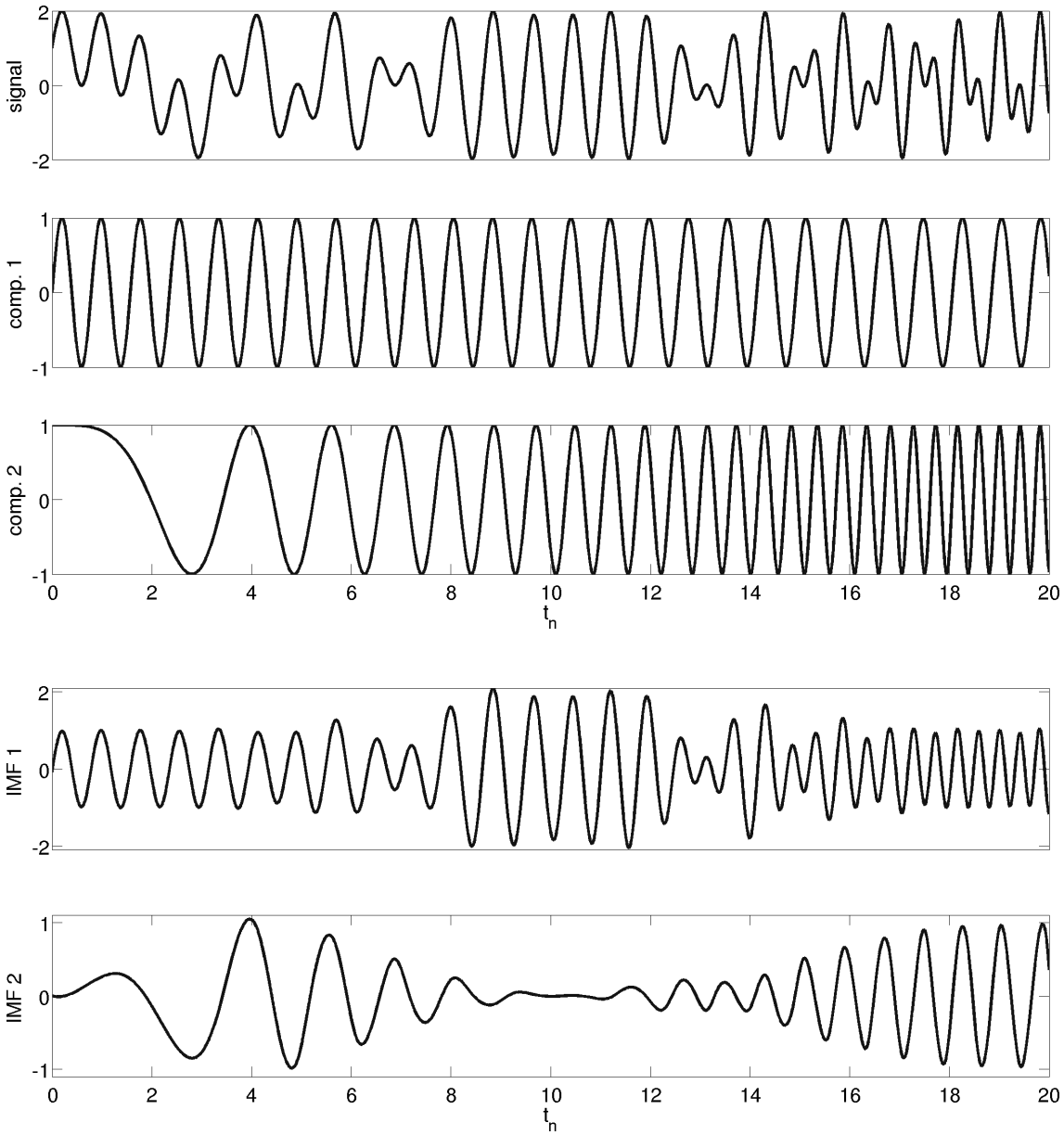

Figure 3.3 The first plot depicts the original signal composed of the two sinusoidal components below. The two graphs on the bottom illustrate IMF 1 and 2 after the decomposition with EMD, exhibiting mode mixing caused by the occurrence of very similar frequencies in both components.

Amplitude

Concerning amplitude resolution, oscillations with very small amplitude, compared to the other modes contained in the signal, cannot be extracted by Empirical Mode Decomposition, as it is not possible to detect the extrema of such small amplitude oscillations, especially in case of additional noise. As a result, the related time series will not be decomposed correctly (for an example see [28]).

3.4.2 Variable Methods of the EMD Implementation

Being a heuristic, several parts of the Empirical Mode Decomposition algorithm can be implemented diversely. The decomposition depends on the choice of implementation variants of the algorithm, hence uniqueness of the decomposition cannot be guaranteed. Among the critical options are the envelope construction, the boundary conditions and the stopping criterion. In the following section several techniques, which can be applied, will be introduced. Some of these matters are shortly discussed in [15, 29] and will be summarized in the following. Being a heuristic method the decomposition quality of EMD for the implementation of the different approaches can only be tested empirically using toy data experiments. It is not possible to show improvements mathematically but only numerically.
In this context the implemented version of the algorithm used throughout this thesis will be presented.

Envelope Construction

A major point concerns the way how the envelopes are estimated. To create the envelopes first the maxima and minima of the date are localized. Then the maxima are connected by a function producing the upper envelope $U(t_n)$. This is equivalently done for the minima generating the lower envelope $L(t_n)$. The mean of both envelopes

$$m(t_n) = \frac{1}{2}\big(U(t_n) + L(t_n)\big) \tag{3.19}$$

is supposed to reflect the pointwise local mean of the signal as precise as possible.
Spline interpolation is the most often used technique to create the envelopes. Splines represent functions which are piecewise composed of polynomials of order k. At their knots, splines obey certain conditions like continuity or being k-1-times continuously differentiable. The envelopes are needed – as an auxiliary construction – to estimate the local mean at every sample point. It is thus essential to precisely determine the local extrema of the function $x(t_n)$. To locate extrema precisely, over-sampling is

generally advisable. Most often cubic splines are used to interpolate maxima respectively minima [13, 15], as well as in this thesis. Cubic splines represent the functions $U(t_n)$ and $L(t_n)$ by a cubic polynomial between any two knots t_k, t_{k+1}.They generally provide good results, but are computationally costly. However, cubic splines are a good trade-off for practical applications, in contrast to the more precisely tunable higher order splines, which demand an even higher computational load.
Alternative interpolation schemes have been proposed using taut [13] or rational [30] splines, which allow, depending on an extra parameter, a smooth transition between a linear and a cubic spline. These attempts provided only marginal improvement and often induce too many IMFs or increase the required number of sifting iterations. Also linear or polynomial splines were tried [15], but they also tend to increase the essential sifting steps and to "over-decompose" the signals. Furthermore, quadratic cost functions were proposed which had to be optimized to determine the envelopes, but these approaches are numerically very costly and show only moderate improvement [31]. Chen *et al.* show that B-splines deliver similar results as cubic splines, however a larger number of IMFs is produced [32].
As a further alternative, not the extrema of the time series but the maxima and minima of the high-pass filtered data are used as knots for the spline interpolations. For interpolation Hermite polynomials have been suggested [33, 34]. Recently, there have been attempts also to estimate local means directly and give up of the idea of using envelopes [35, 36]. First results are encouraging but the technique needs to be developed further.

Boundary Conditions

The boundary conditions create artifacts which need to be avoided. Spline interpolation induces mismatch at the boundaries of the intervals, hence leads to large fluctuations at the beginning and the end of the data set (extrema are hardly met at borders). If the first and last data point are considered knots of the upper and lower envelope, un-physical results will be created. Such defects propagate to signal components extracted later (see [29] for an example).
Several procedures like padding the ends with typical waves [13], mirroring the extrema closest to the end [15], using the average of the two closest extrema for the maximum or minimum spline [37] or the SZero method [38] have been proposed. Periodic boundary conditions also seem useful as long as there are no abrupt changes in the time series or strong time-dependent changes of frequency and amplitude. An alternative is the omitting of the first samples of the decomposition regarding

them defective. As long as the data set is extensive enough, this approach seems reasonable. However, none of those methods seem optimal.

The EMD algorithm applied in this thesis treats the boundaries of the time series as follows: As a start the first sample of the data is specified as first maximum (and minimum) $m_1 = t_1$. Then the slope between the second $(m_2 \mid x_{m2})$ and third $(m_3 \mid x_{m3})$ maximum is calculated

$$\delta_{23} = \frac{x_{m2} - x_{m3}}{m_2 - m_3} = \frac{\Delta x_{m23}}{\Delta m_{23}} \tag{3.20}$$

With the computed slope a straight line is constructed crossing the second and third maximum. Now the intersection point $\delta_{23}(m_1 - m_2) + x_{m2}$ of the straight line with the vertical line at m_1 is calculated and will be used as the new first maximum $(m_1 \mid x_{m1})$, if the value is larger than the x-value of the first sample $x(m_1)$.

$$x_{m1} = \max \left[\delta_{23}(m_1 - m_2) + x_{m2},\ x(m_1)\right] \tag{3.21}$$

This procedure is applied equivalently for the minima at the beginning and the extrema at the end of the time series.

However, in chapter 4 an alternative way of dealing with boundary effects will be introduced called weighted Sliding EMD.

Stopping Criterion of the Sifting Process

Plain EMD continues the sifting process on the full signal as long as there exist local segments with means not yet close to zero. An unsuitable stopping criterion easily leads to over-sifting which means it tends to split meaningful IMFs into meaningless fragments. Criteria for stopping the sifting process often depend on signal changes during the sifting. A common stopping criterion is based on the total variance [13]:

$$\sigma_{i,k}^2 = \sum_{n=1}^{N} \frac{\left(h_{i,k-1}\left(t_n\right) - h_{i,k}\left(t_n\right)\right)^2}{h_{i,k-1}^2(t_n)} \tag{3.22}$$

The first IMF is obtained whenever $\sigma_i^2 < \delta$ holds for some appropriately chosen threshold δ and so on. The whole procedure stops when the residuum $r(t_n)$ is either a constant, a monotonic slope or contains only one extremum. This Cauchy-like convergence criterion, however, does not explicitly take into account the two IMF conditions and can be satisfied without adhering to the latter [13]. Instead, Rilling

et al. [15] introduced an evaluation function

$$\sigma(t_n) = \frac{U(t_n) + L(t_n)}{U(t_n) - L(t_n)} \tag{3.23}$$

depending on the upper $U(t_n)$ and lower $L(t_n)$ envelope and proposed two thresholds δ_1, δ_2. The sifting process is then iterated until $\sigma(t_n) < \delta_1$ for a prescribed fraction $(1 - \alpha)$ of the total duration of the time series and $\sigma(t_n) < \delta_2$ for the rest. Typical values are $\alpha \approx 0.05$, $\delta_1 \approx 0.05$ and $\delta_2 \approx 10 \cdot \delta_1$. However, this introduces three new parameters which the user has to fix and which might influence the resulting IMFs. Wu and Huang state in [26], that about 5 sifting iterations are sufficient to satisfy the stopping criterion proposed by Huang *et al.* in [13] (see equation (3.22)). In order to guarantee the convergence and stability of the resulting IMFs, the number of sifting steps is predefined to 10. The compliance of the IMF criteria is also not guaranteed for this particular stopping criterion, deviations should be small, though. The latter stopping criterion is also used for the EMD algorithm applied to all decompositions in this thesis. Additionally, it has the advantage of putting modes with similar frequency content always in the same IMF in the windowed decomposition method Sliding EMD presented in chapter 4.

3.4.3 Range of the Boundary Artifacts

In the following, the range of the boundary artifacts of EMD is studied depending on the frequency of the underlying components and the sample size [39]. In order to be able to quantify the reconstruction error, toy data examples are used. The results obtained using the toy example illustrated in figure 3.4 are depicted in this section. The toy signal consists of

- a sawtooth wave $x_1(t_n) = 0.6366 \cdot \arcsin\big(\sin(699 \cdot t_n)\big)$,
- a sinusoid $x_2(t_n) = \sin(327 \cdot t_n)$,
- a cosine function with a time-dependent frequency $x_3(t_n) = \cos\big(2 \cdot (t_n + 20)^2\big)$,
- and a monotonous trend $x_4(t_n) = 0.1 \cdot t_n - 1$

which renders the superposition of the signals nonstationary. Thereby, $t_n = 0, \ldots, 19.9995$ with an interval of $\Delta t_n = 0.0005$ between the samples.
After the decomposition of a segment of the time series with EMD, the evolution of the reconstruction error is calculated in the chosen segment by subtracting the

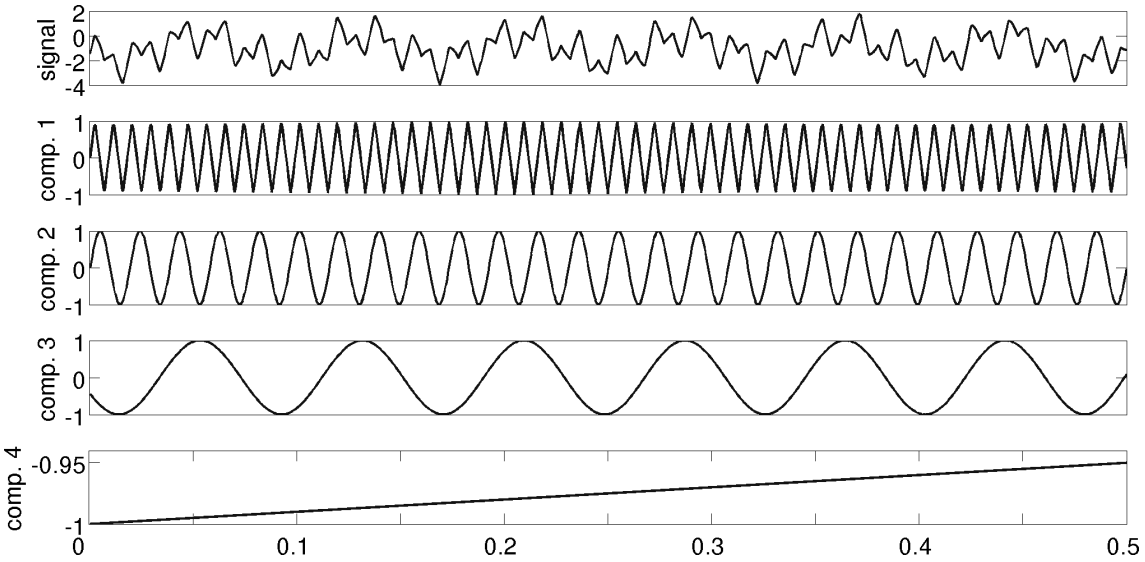

Figure 3.4 For better visualization only a detail of the toy signal (top trace) consisting of a sawtooth wave, a sinusoid, a cosine function with time-dependent frequency and a monotonic function (lower traces) is illustrated.

original component and the corresponding IMF, and recording the absolute of the resulting values. The resulting error time series is smoothed by averaging, which is presented in figure 3.5. The gray crosses mark the range of the boundary artifacts which is defined in the following way: As a limiting value for the artifact reach, 2.5 times the average error of the middle part of the reconstruction error time series is defined. In this case, the middle part of the time series means the time series without the first and last 200 data points, respectively.

As the reconstruction error for the monotonous trend is lowest where the two lines intersect, an artifact reach cannot be defined in that case. Thus, only components $1 - 3$ are used for the analysis. The sample sizes $N = 500$, 1000, 1500, 2000, 2500, 3000, 4000 and 5000 are considered. For every IMF and all sample sizes 1000 different fragments of the data are tested regarding their boundary artifact range.

The diagram figure 3.6 illustrates the average artifact ranges and their standard deviations at the beginning of the time intervals as function of the sample size. They are almost identical to the artifact ranges at the rear ends, which, therefore, are not depicted.

For IMF 1 and 2 (not depicted) of the example, the boundary artifact ranges remain constant, whereas for IMF 3 they are smaller for smaller sample sizes, which is apparent in figure 3.6. That behavior can be caused by the evaluation method, since the reconstruction error is generally larger for smaller sample sizes. Hence,

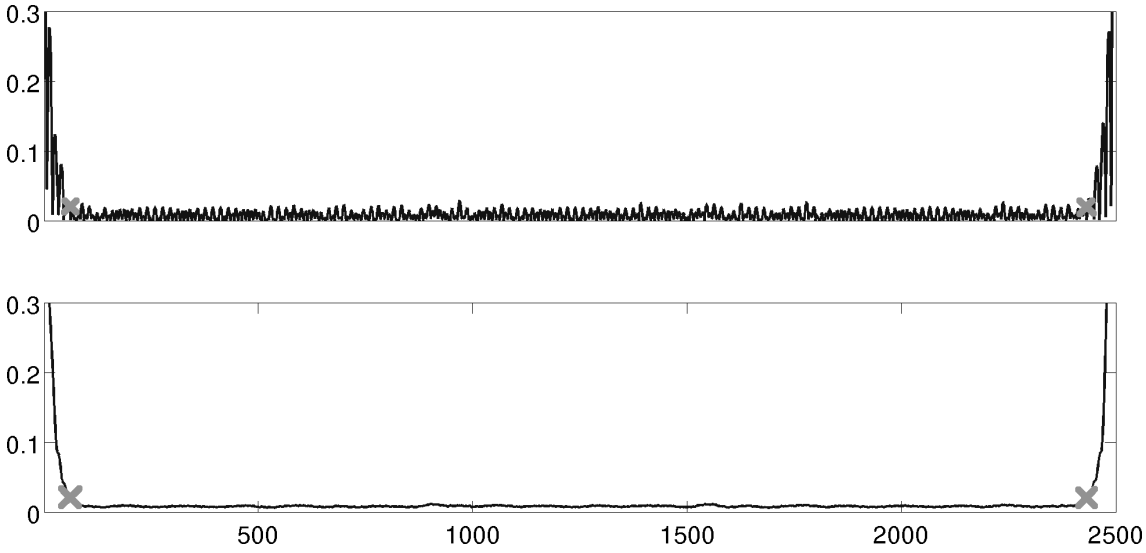

Figure 3.5 The time series depicts the reconstruction error of the first component after EMD is applied to a segment of size $N = 2500$, depending on the position within the segment (upper trace) and the same time series after smoothing (bottom trace). The gray crosses mark the range of the artifacts from the boundaries.

the limit value for the artifact range is higher. Further, it can be noted, that the lower the frequency, the wider the artifacts spread from the boundaries towards the center of the segment.

Figure 3.7 (top) shows the artifact range at the beginning and end of the segments for all studied IMFs, respectively, frequencies with a fixed sample size $N = 3000$.

Again the frequency dependence of the artifact range is apparent. Presumably, the reason for this effect is that for higher frequencies fewer extrema and accordingly knots for the spline interpolation are available, i. e. the signal reconstruction is less accurate and the inaccurate, guessed boundary extremum is more important.

In figure 3.7 (bottom) the artifact spread is shown as average number of periods of the corresponding frequency component which is affected for sample sizes $N = 2000, 2500$ and 3000.

The boundary artifact range is weaker than linearly dependent on the frequency and the number of periods affected by the boundary artifacts is not constant. Furthermore, it is only marginally dependent on the sample size. The frequency of the third component changes over time. Therefore, as a reference period of the original component, the average period of the time series was used. Due to the fact that the whole time series or all periods, respectively, were used for the calculation of the artifact spread.

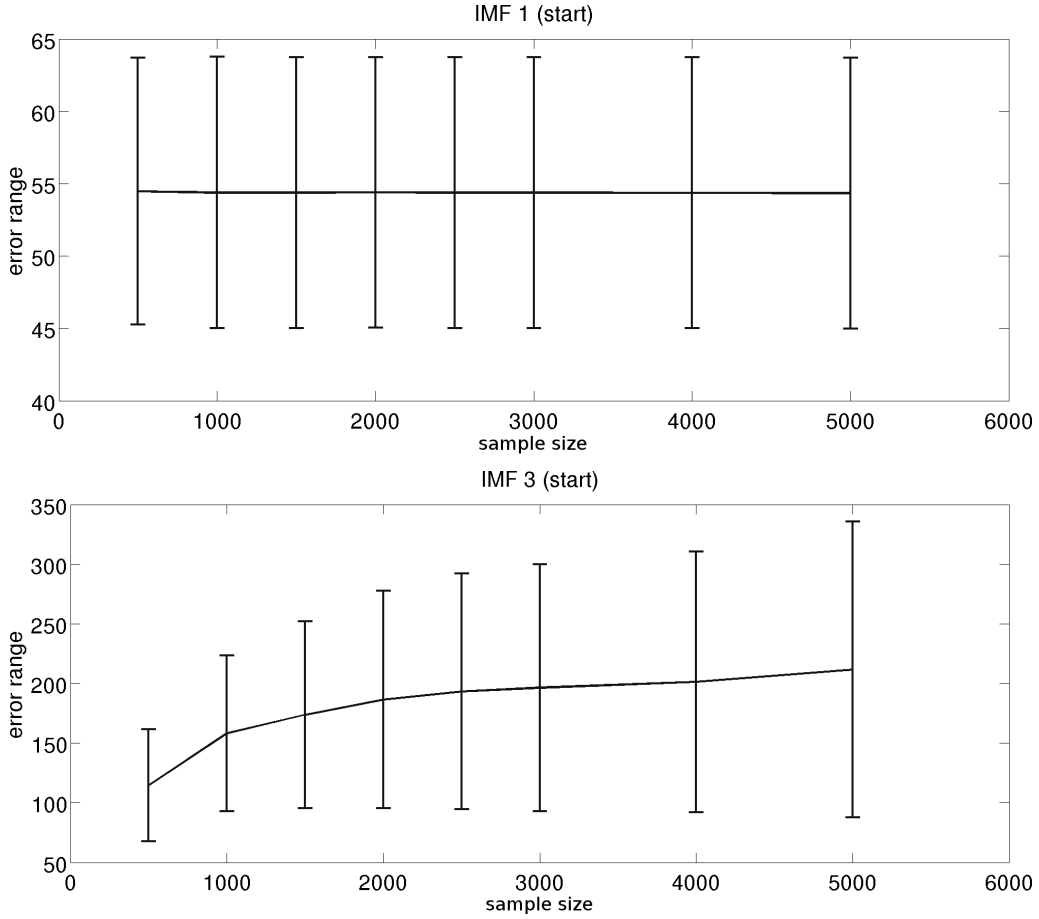

Figure 3.6 The average artifact ranges and their standard deviations at the beginning of the segments for different sample sizes and IMFs 1 and 3.

Considering all results it can be concluded that the use of a too small amount of samples is not recommended for EMD. The data set to be decomposed should always be sufficiently long, since for smaller sample sizes, the boundary artifacts affect a too large part of the time series.

3.4.4 Shortcomings of EMD

As EMD is a completely empirical method, any physical meaning of the extracted IMFs cannot be guaranteed. This is, of course, also true for most applications of time series analysis methods, especially using those with a fixed basis system. However, IMFs preserve their amplitude modulation and changing frequency and also keep their nonlinearity. As stated above, uniqueness of the decomposition cannot be guaranteed. Hence, depending on the set of parameters applied, IMFs

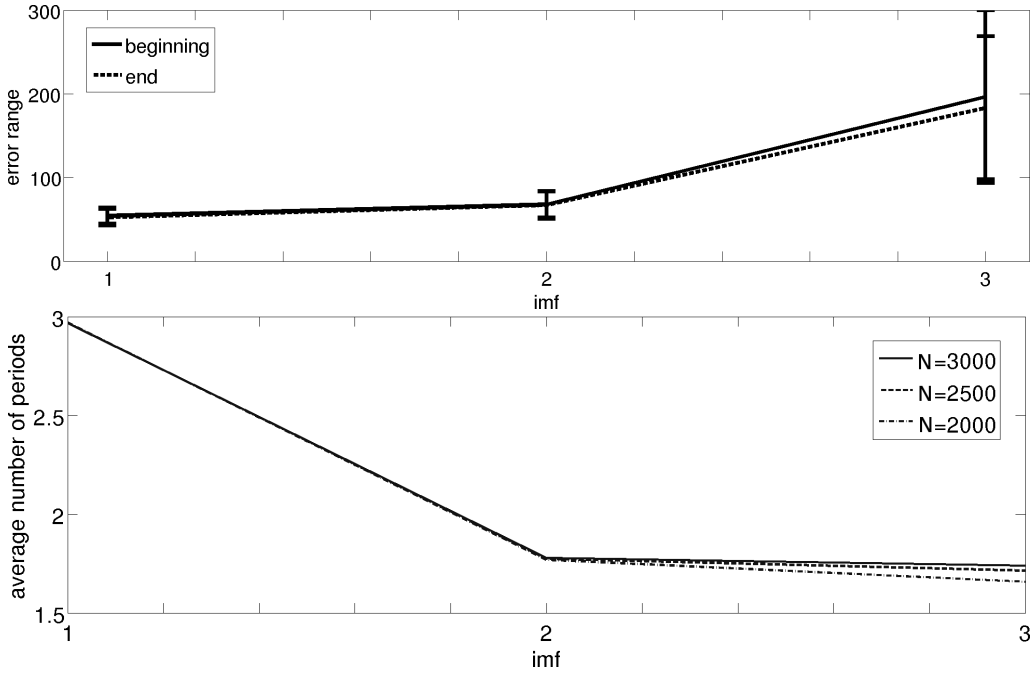

Figure 3.7 The average artifact ranges and their standard deviations at both ends of the segments for a constant sample size $N = 3000$ and IMFs $1 - 3$ are presented(top). The average number of periods of the corresponding components affected by the artifact range for the sample sizes $N = 2000, 2500$ and 3000 are illustrated (bottom). As the frequency of component 3 changes with time, its average period was considered as reference.

may be extracted which differ in their appearance and characteristics.
The most serious drawback of the method is certainly its lack of any theoretical basis which would allow to evaluate the performance of the algorithm in objective terms. Hence, to do so one needs to employ complex, carefully designed toy data to simulate the decomposition process into single modes and the impact of the various parameters and constraints onto the sifting process. Despite all this, EMD has been used successfully for many practical applications (see for example [40, 41, 42, 4, 43, 44]).

3.5 Recent Extensions to EMD

A number of extensions to plain EMD have been proposed in recent years to broaden the fields of application, adapt to specific data or improve the method. Among them even several two-, respectively, multi-dimensional EMD techniques were introduced in [45, 46, 47]. Some of the extensions, namely Ensemble Empirical Mode Decomposition, Local EMD and on-line EMD will be discussed shortly in the following.

3.5.1 Ensemble EMD

Ensemble Empirical Mode Decomposition (EEMD) is a noise-assisted method to enhance and improve sifting [14]. It is based upon investigations of the statistical properties of white noise [48]. It was shown there, that EMD is equivalent to an adaptive dyadic filter bank with overlapping bandpass filters with constant quality factor [49, 26].
An ensemble of $k = 1, \ldots, K$ data sets $x_k(t_n)$ is created by adding white noise $\epsilon_k(t_n)$ (finite amplitude, zero mean, constant variance) to the original time series $x(t_n)$

$$x_k(t_n) = x(t_n) + \epsilon_k(t_n) \tag{3.24}$$

Decomposing the noisy data sets slightly different IMFs, respectively, residua are generated:

$$x_k(t_n) = \sum_{l=1}^{L} c_{lk}(t_n) + r_k(t_n) \tag{3.25}$$

EEMD considers true IMFs $c_l(t_n)$ and residua $r(t_n)$ as an ensemble average of extracted IMFs according to

$$c_l(t_n) = \frac{1}{K} \sum_{k=1}^{K} c_{lk}(t_n) \tag{3.26}$$

$$r(t_n) = \frac{1}{K} \sum_{k=1}^{K} r_k(t_n) \tag{3.27}$$

In practice EEMD works as follows:

- Add white noise to the data set
- Decompose the noisy data into IMFs
- Repeat these steps and at each iteration add white noise
- Calculate an ensemble average of the respective IMFs to yield the final result

Through averaging the respective IMFs, noise contributions will cancel out leaving only the true IMFs. Noise amplitudes can be chosen relatively high, but the ensemble number K should be large. The number of sifting steps and the number of IMFs has to be fixed in advance to render extracted IMFs truly comparable. This manner of stopping the sifting process does not take the adherence of the IMF criteria into account though. However, mode mixing is reduced in EEMD and an improved separation of modes with similar frequencies results. Due to the added

noise, the time series contains a lot more local extrema, which renders the estimation of the envelopes computationally much more demanding. Also more high frequency components result, naturally, since the white noise is not canceled out completely in practical applications. In summary, EEMD is computationally costly but a promising additional EMD technique.

An illustrative example of the performance of EEMD compared to EMD is given in figure 3.8. Two signals, $x_1(t_n) = 0.1 \cdot \sin(20\, t_n)$ and $x_2(t_n) = \sin(t_n)$, are superimposed whereby in signal $x_1(t_n)$ the oscillation is interrupted for certain time spans to simulate a situation which often happens with biomedical signals. Figure 3.8 b) illustrates the first two IMFs obtained with standard EMD while figure 3.8 c) depicts IMFs obtained with EEMD using $K = 15$ different noisy signals to build an ensemble starting from the original signal. Clearly, standard EMD exhibits strong mode-mixing in this case while EEMD copes quite well with this complicated signal.

3.5.2 Local EMD

To satisfy the stopping criterion of sifting, the mean of both envelopes needs to be close to zero everywhere. Local EMD [15] pursues the idea that, during sifting, in some parts of the signal the mean might already be zero, whereas in other parts it is not yet close enough to zero (see [28] for an example). Hence, it could be advantageous to iterate the sifting process only in regions, where the mean is still finite to finally meet the stopping criterion everywhere. Local EMD, thus, identifies regions with large mean values and continues sifting there, while in other regions the IMF is already achieved. Localization can be implemented via a weighting function $w(t_n)$, which is $w(t_n) = 1$ in regions in which sifting is still necessary and decays to zero at the boundaries. This can easily be integrated into the EMD algorithm via

$$h_{j,k}(t_n) = h_{j,k-1}(t_n) - w_{j,k}(t_n) \cdot m_{j,k}(t_n) \tag{3.28}$$

However, one has to be careful with discontinuities at the edges of the intervals which are treated differently. This procedure essentially improves the sifting process and tries to avoid over-sifting, yet, complicates the sifting process with more parameters to be controlled.

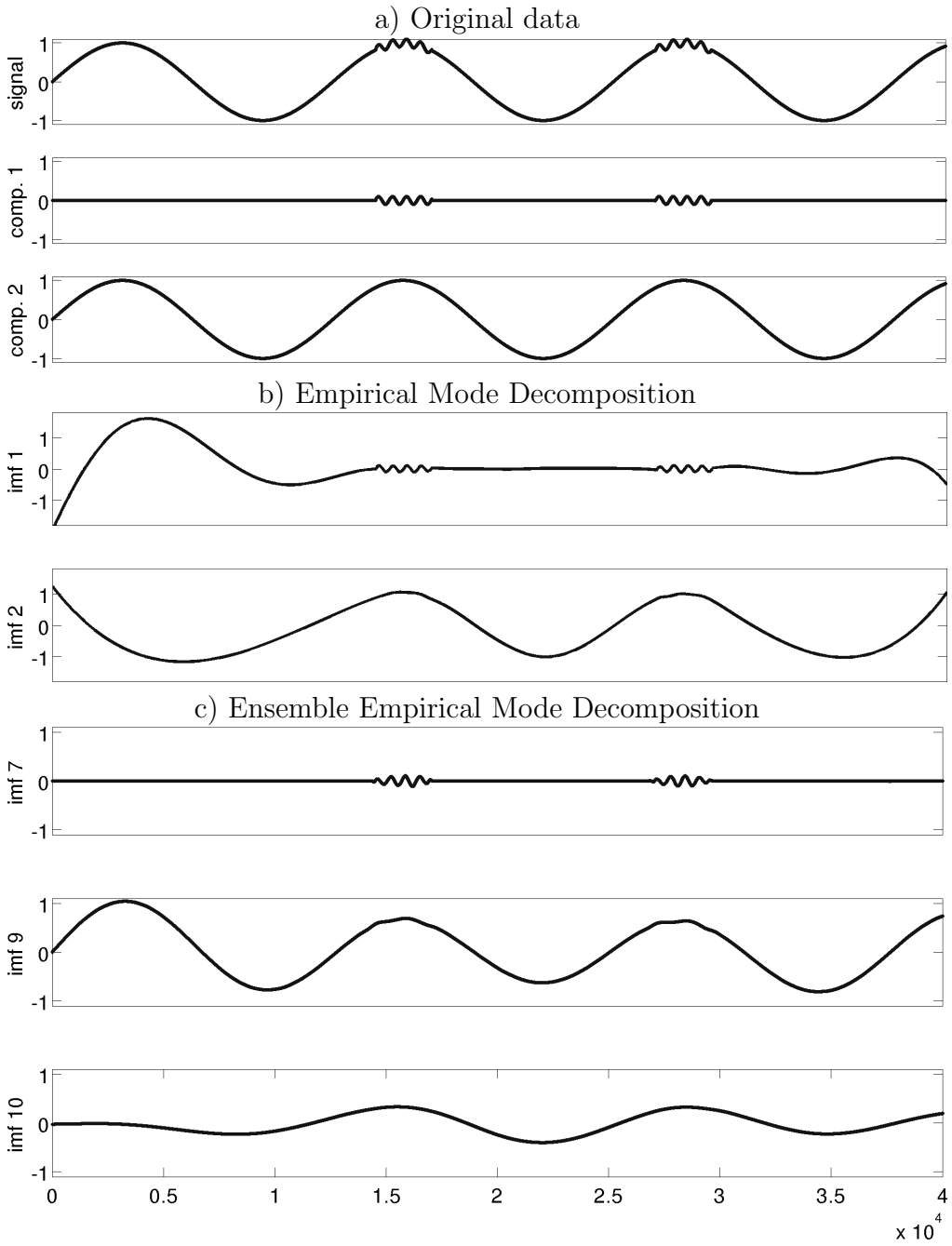

Figure 3.8 a) Original data: superposition of the signals $x(t_n) = x_1(t_n) + x_2(t_n) = 0.1\sin(20 \cdot t_n) + \sin(t_n)$ denoted by *comp. 1* and *comp. 2*. Note that signal $x_1(t_n)$ is constant for a large part of the total time span. b) The first two IMFs obtained with an EMD analysis. Mode mixing is clearly visible due to the partial absence of oscillations within component $x_1(t_n)$. c) The relevant IMFs resulting from an EEMD analysis. The component signals underlying the original signal are extracted almost perfectly.

3.5.3 On-line EMD

The application of EMD to e.g. biomedical time series is limited by the size of the main memory of the computer. Hence, in practical applications only relatively short time series can be studied. However, many practical situations like continuous patient monitoring ask for an online processing of the recorded data.
Recently, on-line EMD has been proposed by Rilling *et al.* [15]. It starts the decomposition before the complete data set is available, hence, simultaneously recording and decomposing data becomes possible that way. On-line EMD is supposed to work on segments of the data. This is possible as EMD is based on the construction of envelopes which need only a few extrema to yield a reasonable estimate of the interpolating polynomial. Thus, a time series could be worked up step by step, applying EMD to segments of the total data set only. To stay consistent, the number of sifting steps needs to be identical in every window, of course. The further advantage is a reduced computational load as the memory demand increases stronger for plain EMD (in contrast to on-line EMD) with the number of time points over which the data are sampled. In [15] it is proposed to fix the number of sifting steps a priori. The algorithm works via enlarging the window on the forefront whenever new data appear and reducing the size of the window on the back whenever the stopping criterion is reached.
This approach, however, has some drawbacks related to the discontinuities occurring at the boundaries. Furthermore, the question, which information remains in the residuum also strongly depends on the size of the window so that the signal decomposition as a whole strongly depends on the window size. Imagine long wavelength changes which would appear as monotonous trends in windows with a length small compared to the wavelength but would be recognized as oscillations and extracted as an IMF with sufficiently large window sizes. Due to the changing window size of the on-line EMD algorithm problems could arise. In summary, on-line EMD presents a good idea, however, results leave room for improvements. The method is still in its infancy and needs yet to be developed further, as well as the proposal in [50].
Also in [51, 52, 53, 54, 55, 56, 57] some very recent suggestions of an online implementation of EMD are given. However, they are still to be evolved further, since they often lack in suggesting a sophisticated solution to problems e.g. arising due to boundary artifacts. Additionally, in some of the suggested approaches the results differ depending on the used method: plain or online EMD.
In chapter 4 (see also [58, 59]) an alternative, robust and efficient online technique, called Sliding Empirical Mode Decomposition, is presented.

Chapter 4

Sliding Empirical Mode Decomposition

Plain EMD is applied to the complete signal which, in view of limited resources like computer memory and CPU, also limits the length of the time series to be dealt with. This is an especially serious problem in dealing with biomedical time series, which often are recorded over very long time spans with high sampling rates. Brain status data, for example acquired during neuromonitoring in clinical intensive care units, accumulate to huge amounts of data when monitoring patients over days with appropriate signal sampling rate (up to 1 kHz).

Analyzing such large data sets all at once is hardly possible because of the computational load involved when using conventional EMD [58, 29]. Even more important, however, is the fact that data analysis has to wait until monitoring is finished. The patients usually reside in critical condition, hence, an immediate online analysis of such time series is of utmost importance. One possible solution would be to cut the data into several distinct pieces and apply EMD to these segments. But in this case, due to the well known boundary problem of EMD, discontinuities will occur as depicted in figure 4.2. The impact of the boundary artifacts has already been discussed in section 3.4.3. In the following an online implementation of EMD called *Sliding Empirical Mode Decomposition* or SEMD will be proposed [60]. This algorithm will decompose time series of arbitrary length into a residuum and IMFs. In the subsequent paragraphs the operating mode of SEMD and some characteristics of the IMFs and the residuum will be explained. Furthermore, a more sophisticated version of SEMD called weighted Sliding EMD will be introduced, which reduces the impact of the boundary artifacts even more, and two different implementation techniques will be discussed, compared and evaluated.

4.1 The Principle of SEMD

In a first step, the recorded time series is split into segments which can be analyzed with Empirical Mode Decomposition. Simply adding the IMFs extracted from the different segments together, would induce boundary artifacts, however. This is illustrated in a simple example in figure 4.1 and figure 4.2, respectively. The original data (see figure 4.1, top trace) is split into 4 segments, which are decomposed separately with conventional EMD. Discontinuities appear at the ends of the segments, namely at $t_n = 0.25,\ 0.5$ and $t_n = 0.75$, when joining the resulting IMF segments together (see the IMFs in figure 4.2). Thus, simply segmenting a time series into non-overlapping windows for further analysis leads to strong boundary artifacts which can be avoided using Sliding Empirical Mode Decomposition (SEMD), which works as follows.

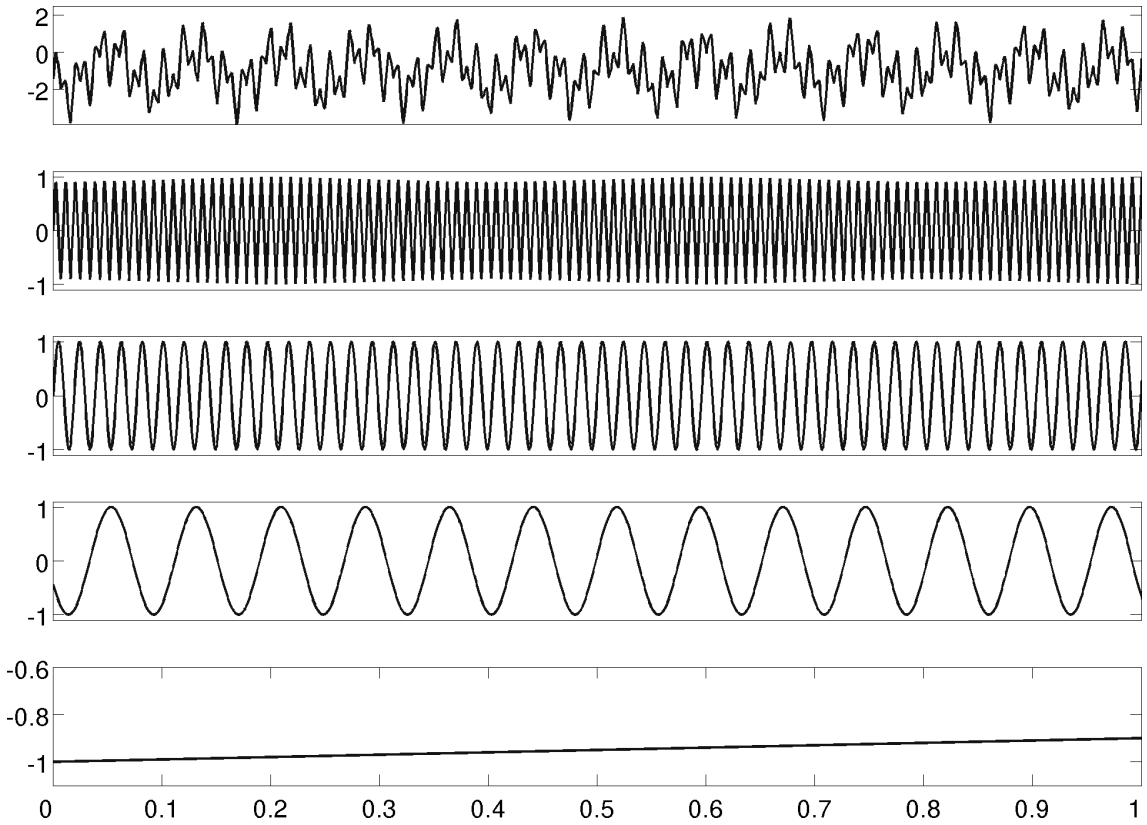

Figure 4.1 For better visualization only a detail of the toy data signal (top trace) and its underlying signal components is illustrated. It consists of: a sawtooth wave $x_1(t_n) = 0.6366 \cdot \arcsin\big(\sin(699 \cdot t_n)\big)$ (second trace), a sinusoid $x_2(t_n) = \sin(327 \cdot t_n)$ (third trace), a cosine function with a time-dependent frequency $x_3(t_n) = \cos\big(2 \cdot (t_n + 20)^2\big)$ (fourth trace) and a monotonic trend $x_4(t_n) = 0.1 \cdot t_n - 1$ (bottom trace), whereas $t_n = 0, \ldots, 19.9995$ with $\Delta t_n = 0.0005$.

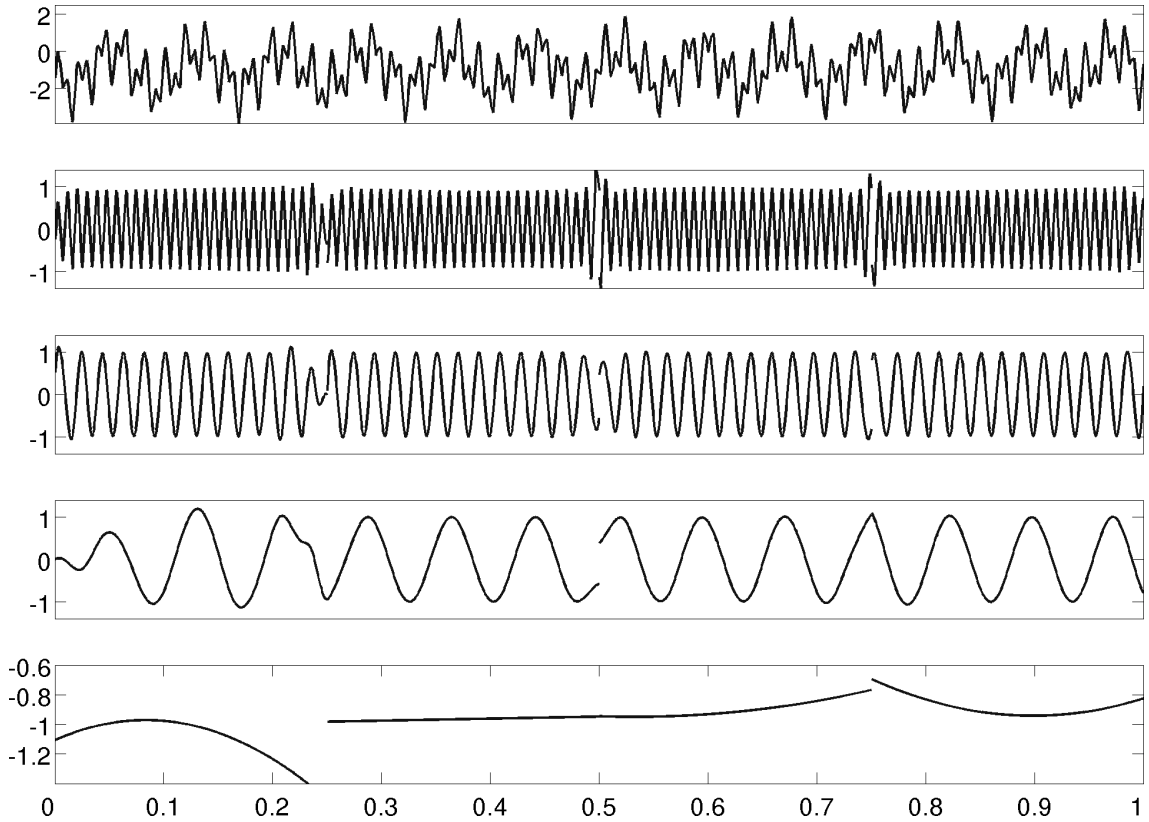

Figure 4.2 EMD decomposition of the toy signal in figure 4.1. The time series has been segmented into 4 parts and decomposed with EMD. After joining the resulting IMFs together, boundary effects become clearly visible at $t_n = 0.25,\ 0.5$ and $t_n = 0.75$.

Using Sliding Empirical Mode Decomposition the recorded time series is split into overlapping segments, which can be analyzed with conventional EMD. The segment size M has to be a multiple of the step size K with which the subsequent segments are shifted relative to each other. Thus, if $\frac{M}{K} \in \mathbb{N}$ holds, all windows can be assembled as is depicted in figure 4.3. Since M is a multiple of K in the illustrated example, window number 5 can subsequently be joined after window 1. Thereby the last sample of window 1 could be denoted with t_M and the first data point of window 5 with t_{M+1}, which corresponds to the subsequent sample of the time series. Hence, neighboring segments can be joined without resulting gaps and for every sample the same amount of estimates is obtained. Every data point is, thus, represented equally often, namely $E = \frac{M}{K}$ - times, in the overlapping segments for a later estimation of the corresponding mean sample value. The time series in every segment w is decomposed by EMD into $l = 1, \ldots, L$ individual IMFs, denoted by

$c_{l,w}(t_n)$, and a local residuum, denoted by $c_{L+1,w}(t_n) \equiv r_w(t_n)$, according to

$$x_w(t_n) = \sum_{l=1}^{L} c_{l,w}(t_n) + r_w(t_n) \tag{4.1}$$

whereby the number of sifting steps is kept equal in all segments w.

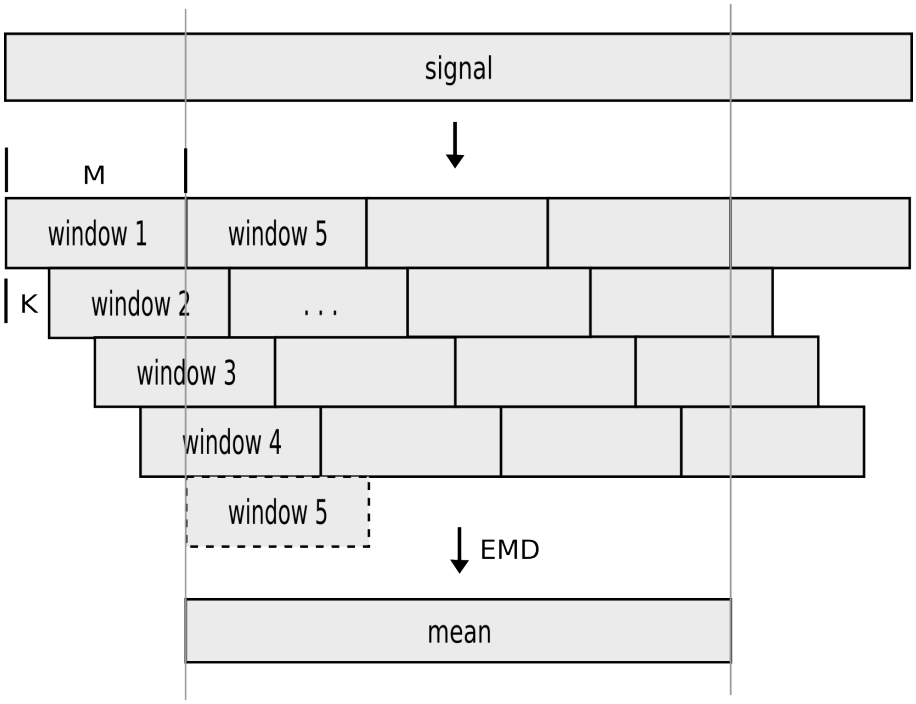

Figure 4.3 The scheme depicts the principle of Sliding EMD, whereas M denotes the size of the window and K the step size.

The total number of windows W to be decomposed is given by

$$W = \frac{N - M}{K} + 1 \tag{4.2}$$

with N denoting the total number of time samples t_n in the time series. Resulting IMFs are collected in a matrix with corresponding sample points forming a column of the matrix with $E = \frac{M}{K}$ rows. Only columns which contain an identical number of entries are used to estimate average IMF amplitudes at every point in time t_n in each segment. Consequently, the first and last $M - K$ samples (respectively M samples for convenience) of the time series are omitted (see gray vertical lines in figure 4.3).

This finally yields for the IMFs $c_l(t_n)$ and the residuum $r(t_n)$ with $t_n > M$ and the

window number $h = \lfloor \frac{t_n - M}{K} \rfloor + 2$ (whereby the brackets denote the floor function, which rounds a real number down):

$$c_l(t_n) = \frac{1}{E} \sum_{w=h}^{h+E-1} c_{w,l}(t_n) \tag{4.3}$$

$$r(t_n) = \frac{1}{E} \sum_{w=h}^{h+E-1} r_w(t_n) \tag{4.4}$$

with $h \in \mathbb{N}$. By construction SEMD fulfills the condition to be complete, as much as plain Empirical Mode Decomposition does:

$$x(t_n) = \frac{1}{E} \sum_{w=h}^{h+E-1} \Big(\sum_{l=1}^{L} c_{w,l}(t_n) + r_w(t_n) \Big) \tag{4.5}$$

For every sample $x(t_n)$ the mean values of the E decompositions, done by conventional EMD, form the result of the SEMD decomposition. As all of these EMD decompositions are complete, this equally holds for the mean value. Thus, the most important defining criterion of EMD, which ensures a decomposition without loss of information, is fulfilled by SEMD.
If the number of IMFs in the single windows changed from segment to segment, problems would arise. Therefore, as practical constraints of SEMD the number of sifting steps and IMFs (e.g. $L = \lfloor \log_2 N \rfloor$) is kept constant for all decompositions. Since for the stopping criterion of the decomposition a constant number of steps is chosen, the compliance of the IMF criteria cannot be warranted. Aberrations should, however, be small. Except for the stopping criterion, which here amounts to keeping the number of sifting steps fixed, any EMD algorithm can be applied in the individual windows. A schematic diagram of the SEMD procedure is presented in figure 4.3.

4.2 Properties of SEMD

Because of the segmentation involved, contrary to global EMD the local residua estimated with SEMD for every segment may contain low-frequency oscillations instead, when joined together. The residuum is only non-oscillating in every single window, but not in the resulting global residuum. Figure 4.4 depicts a sinusoid portraying an exemplary global SEMD residuum partitioned into several local residua by vertical lines illustrating examples of local residua.

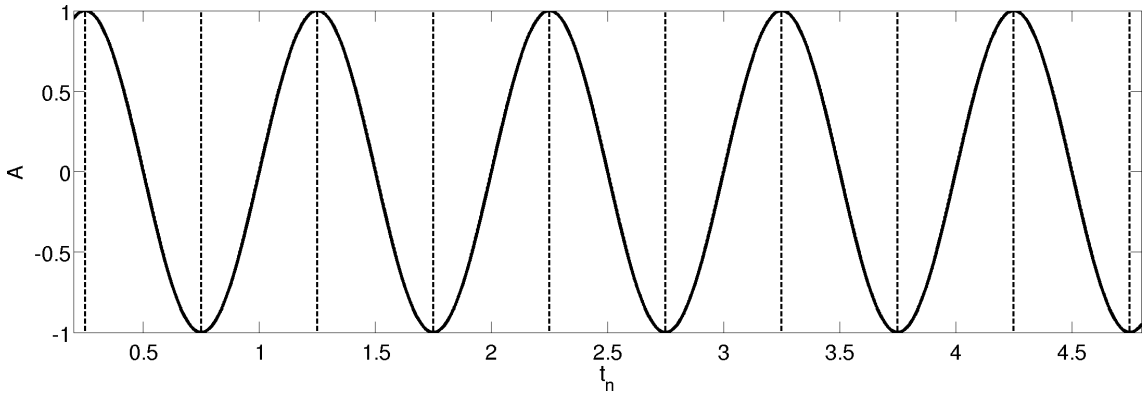

Figure 4.4 A sinusoid exemplifying a global SEMD residuum is depicted partitioned into several windows of 1000 samples by vertical lines illustrating examples of local residua. The ordinate illustrates the amplitude A and the abscissa the temporal scale t_n of the data with an interval between the samples of $\Delta t_n = 0.0005$ s.

By choosing the segment size properly, it may be determined which oscillations should appear as distinct IMFs and which should be absorbed as apparent local trends into the respective residua. These apparent local trends, which combine to low-frequency oscillations in the final average global residuum, may be down-sampled, because of the high sampling rate, to a useful time resolution and subsequently analyzed with SEMD again. This process can be repeated until finally a truly non-oscillating trend remains resulting in a cascaded application of SEMD.

On the other hand, that characteristic can be exploited to filter slowly varying oscillatory modes of the time series. Hence, SEMD acts as a low-frequency filter for long-term oscillations and trends in biomedical time series.

Similar to Ensemble Empirical Mode Decomposition (EEMD) [14], Sliding EMD also achieves an averaging over differently decomposed data sets. While due to added noise, for EEMD a given sample is associated with different amplitudes, for Sliding EMD the same amplitude is associated with various samples in different shifted segments. This latter behavior alleviates effects related with a non-unique data decomposition via EMD. Furthermore, artifacts resulting from end effects loose their impact via averaging.

The number of sifting steps is kept constant for every window, rendering it more likely to find similar modes in the single IMFs. Finally, note that, due to the fixed number of sifting steps, the IMF criteria are not necessarily fulfilled by the resulting modes of the EMD decompositions in the individual windows. Aberrations are supposably small, which should equally hold for the IMFs of SEMD after averaging.

4.3 Weighted Sliding EMD

Despite the averaging operations involved in SEMD, reconstruction errors due to the boundary effects remain to be observed in SEMD. In order to diminish the impact of the latter, a *weighted Sliding EMD* (wSEMD) was developed recently [59, 39]. Two different possibilities to weight the individual windows will be introduced: weighted estimates SEMD (weSEMD) and weighted window SEMD (wwSEMD). Furthermore, the implementation of weSEMD and wwSEMD will be described in detail in section 4.4, where both techniques will also be compared.

4.3.1 Weighted Estimates Sliding EMD

The weighted estimates SEMD works as follows: Every value of the ensemble E of samples, whose average forms the final time series' value, is weighted by a coefficient from a predefined distribution of weights. These coefficients become larger when the estimated data point origins from the middle of the window, and smaller when it is located near one of the boundaries. The coefficients are assumed to form a discrete Gaussian distribution $p_G^{(E)}(t_e)$ with E samples $e = 1, \ldots, E$. Using such weights, boundary effects are strongly suppressed. Considering the windows of the SEMD decomposition, weighted estimates SEMD multiplies every K successive values of the window with the same weight.
Figure 4.5 exhibits an example of an IMF, namely IMF 1, of a toy data example composed of a beating wave and a trend. The time series was decomposed by SEMD with a window size of $M = 15\,000$ and an ensemble size of $E = 30$ and IMF 1 is denoted by the green line. The dark lines originate from the EMD decompositions in all the single windows, which form the ensemble. The results shown in the image corroborate that a weighted form of SEMD is clearly necessary, as the ends of many windows correspond to outliers.

4.3.2 Weighted Window Sliding EMD

In this section we consider an alternative way of applying weights to the time series, in order to suppress boundary artifacts [61]. It amounts to applying a weight to every sample of a window rather than weighting the estimates. Thus, every window of the resulting IMFs and the residuum is multiplied by the weighting function. The latter, again, is assumed to form a discrete Gaussian distribution $p_G^{(M)}(t_m)$. But instead of weighting the estimates, every sample point inside the window is weighted according to its distance to the closest border of the window, which effectively

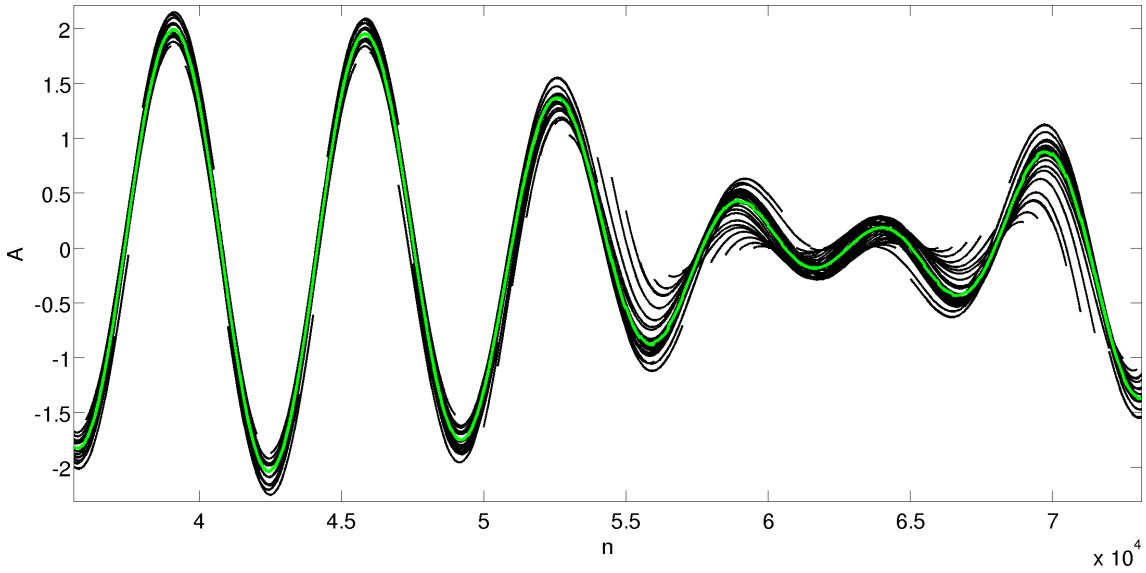

Figure 4.5 The green line depicts IMF 1 of a toy data example consisting of a beating wave and a trend decomposed with SEMD (window size $M = 15\,000$, ensemble size $E = 30$), whereas the dark lines show the EMD decompositions in all the windows, that form the ensemble, which the SEMD decomposition is based on. The ordinate gives the amplitude A of the time series and the abscissa depicts the samples n.

suppresses samples near the boundaries. Therefore, the weighting function consists of M samples, instead of E. Furthermore, the Gaussian distribution is shifted along the ordinate via $p_G^{(M)}(t_m) - p_G^{(M)}(t_1)$, so that $p_G^{(M)}(t_1) = 0$ and $p_G^{(M)}(t_M) = 0$, respectively.

This technique produces a more sophisticated and precise weighting of the estimates as several similar distributions $p_G^{(M)}(t_{m,e})$ with $t_{m,e} \in [1, M]$ and $e = 1, \ldots, E$ are utilized to weight the estimates according to their distance to the window boundaries. After the calculation of the ensemble mean of K data points, every sample position t_m, with $m = 1, \ldots, M$, and therefore point of the weighting function of the window $p_G^{(M)}(t_m)$, has been used exactly once for averaging, as $K = \frac{M}{E}$ (see schemes in figure 4.6).

Hence, K shorter and slightly different distributions $p_G^{(M,i)}(t_{m,e})$ with $i = 1, \ldots, K$ are picked out of the weighting function and are used to weight the estimates, whereas all picked out samples for one ensemble weighting function have a distance of K points, respectively. The K different distributions $p_G^{(M,i)}(t_{m,e})$ can be described as "part" of $p_G^{(M)}(t_m)$ using the following set of samples:

$$\left\{ p_G^{(M,i)}(t_{m,e}) | t_{m,e} = i + 0K,\ \ i + 1K,\ \ldots,\ i + (E-1)K \right\} \tag{4.6}$$

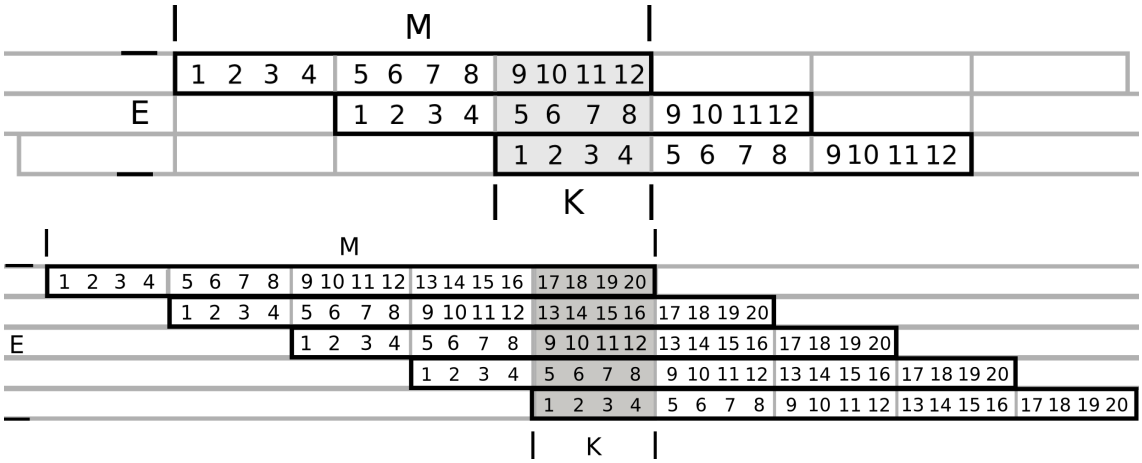

Figure 4.6 The schemes show two examples, which of the samples of the weighting function are used for averaging to obtain the resulting IMF or residuum depending on their position (illustrated by the numbers $1, \ldots, 12$ (top) respectively $1, \ldots, 20$ (bottom)) in the window. In this case the parameters are chosen in the following way $M = 12$, $K = 4$ and $E = 3$ (top), $M = 20$, $K = 4$ and $E = 5$ (bottom).

To calculate the final result for a specific sample of an IMF or the residuum, the sum over E estimates multiplied by E weighting coefficients is computed and the value is normalized by the reciprocal sum of all used factors for that particular data point, so that the amplitude of the signal is preserved.
For a step size of $K = 1$ both methods, the weighted estimates and the weighted window SEMD, are the same, since $E = M$. Otherwise both approaches differ in that a specific set of weights for one data point is repeatedly used again – and only again – after K samples. In the following a thorough comparison between weighted estimates and weighted window SEMD will be conducted.

4.4 Comparison between Weighted Estimates SEMD and Weighted Window SEMD

As the ensemble size equals the window size $E = M$ when the step size $K = 1$, no difference exists between both implementation methods, weighted estimates and weighted window SEMD, in that case. However, in all other circumstances both techniques differ. In the following a comparison will be conducted. First of all the practical implementation of the weighting processes will be presented in detail. A small example of weights will clarify the difference between both weighting methods further and after a comparison of the performance of both techniques, problems

arising under certain circumstances using weighted estimate SEMD will be explained and discussed.

4.4.1 Implementation of the Weighting Processes

For the practical application of the weighting, the normalization of the data is done at the same time as the weighting itself, rendering the process easier to handle. A normalization during the Sliding EMD algorithm is not necessary, since the weights already provide the conservation of the data amplitudes, as their sum equals 1.

Weighted Estimates SEMD

To apply the weighting for weighted estimates SEMD, the sum of all E weights of the discrete Gaussian distribution $p_G^{(E)}(t_e)$ is calculated

$$W^{(E)} = \sum_{e=1}^{E} p_G^{(E)}(t_e) \tag{4.7}$$

yielding the normalization coefficient $W^{(E)}$, while E denotes the ensemble size. Afterwards every weight is multiplied by the reciprocal of this sum.

$$p_G^{(E_W)}(t_e) = \frac{1}{W^{(E)}} \cdot p_G^{(E)}(t_e) \tag{4.8}$$

To be able to easily multiply the E weights with the IMF windows with M samples, the function with the weights has to be extended to a step function with M values. In the example in figure 4.7 with $M = 200$, $K = 4$ and $E = 50$, the normalized discrete Gaussian distribution with $E = 50$ weights is dispersed to a step function with $M = 200$ samples. Now, it can easily be multiplied with the IMFs. This is possible, as all K consecutive data points, respectively, are weighted with the same coefficient. For the example in figure 4.6 (bottom) it would mean, that samples $1, 5, 9, 13$ and 17 form an ensemble of estimates, as well as $2, 6, 10, 14$ and 18 and so on. Therefore, sample numbers $1-4$, $5-8$, $9-12$, $13-16$ and $17-20$ would be multiplied by the same factor. Hence, the extension of the weighting distribution to a step function can be implemented.

All in all no further normalization is needed after the multiplication of the weights with the IMFs. The normalization is already included since the weights all add up to 1.

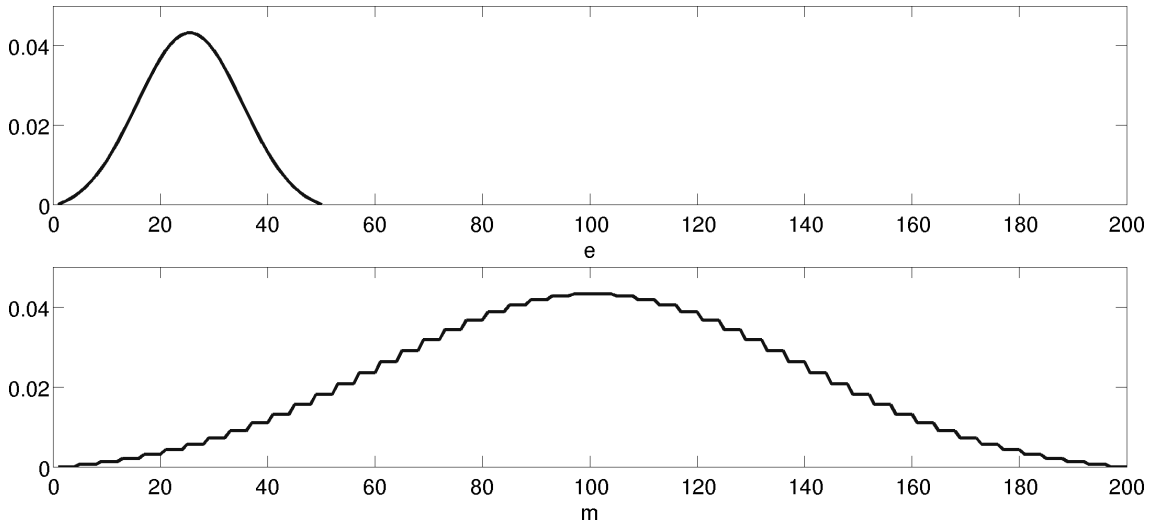

Figure 4.7 Normalized discrete Gaussian distribution containing 50 weights for all $e = 1, \ldots, E$ estimates (top) and the extended step function to fit the $m = 1, \ldots, M$ samples of the window with $M = 200$ (bottom).

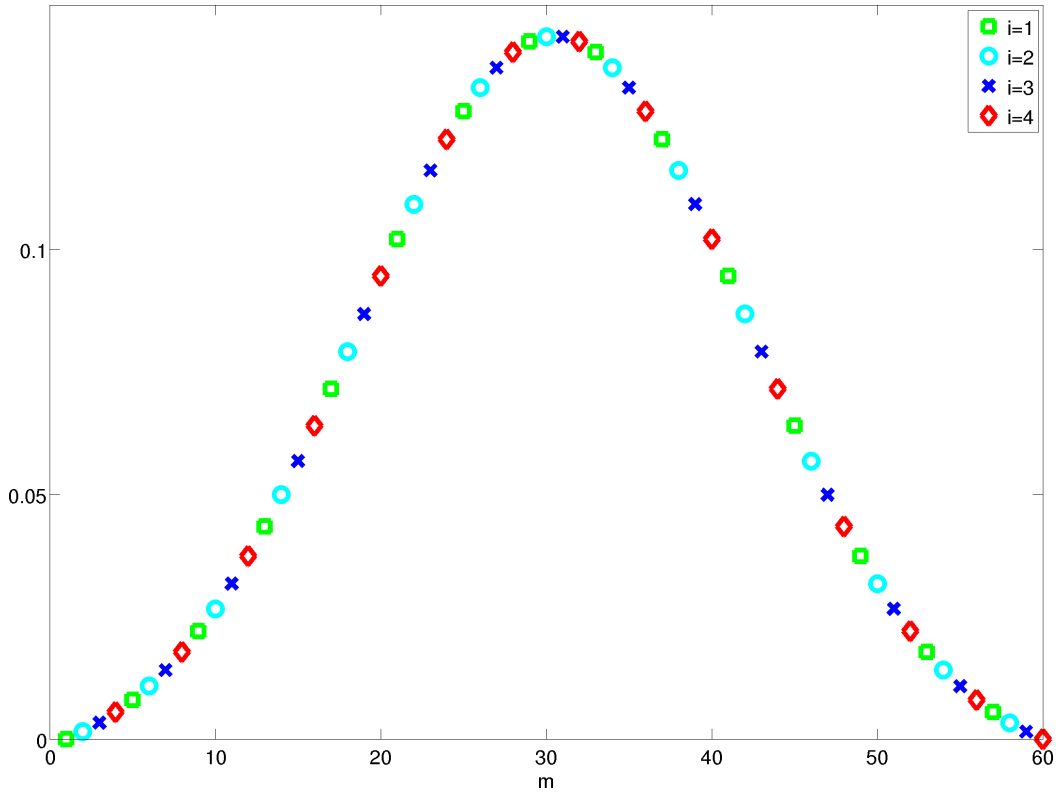

Figure 4.8 Normalized discrete Gaussian distributions containing a total of $K \cdot E = 60$ (with $K = 4$ and $E = 15$) weights to form $i = 1, \ldots, K$ different intertwining weighting functions (highlighted by the various colors). The function has $m = 1, \ldots, M$ samples and thus the same length as the window with $M = 60$.

Weighted Window SEMD

Also for weighted window SEMD the normalization is already included in the weights. As a reminder, the weighting for the weighted window SEMD consists of $i = 1, \ldots, K$ different discrete Gaussian distributions $p_G^{(M,i)}(t_{m,e})$ containing $e = 1, \ldots, E$ weights respectively. Intertwined, the K graphs form the weighting function $p_G^{(M)}(t_m)$ with $m = 1, \ldots, M$ samples as illustrated in figure 4.8 for $M = 60$, $K = 4$ and $E = 15$. The different colors highlight the K weighting functions, which are already normalized in the illustration.
Since we have K different weighting functions $p_G^{(M,i)}(t_{m,e})$ with $i = 1, \ldots, K$, also K different normalization coefficients $W_i^{(M)}$ have to be calculated:

$$W_i^{(M)} = \sum_{e=1}^{E} p_G^{(M,i)}(t_{m,e}) \tag{4.9}$$

In this case, too, the K weighting functions are multiplied by the reciprocal of the corresponding normalization coefficient:

$$p_G^{(M_W,i)}(t_{m,e}) = \frac{1}{W_i^{(M)}} \cdot p_G^{(M,i)}(t_{m,e}) \tag{4.10}$$

The sum of all weights for a particular sample possesses the value 1, so that no further normalization is necessary.

4.4.2 Example of Weights used for weSEMD and wwSEMD

An example will be given in the following to show the differences between both weighting techniques more clearly. In tables 4.1 and 4.2 a short quantitative example illustrates how the samples in the gray area of figure 4.6 (bottom) with $M = 20$, $K = 4$ and $E = 5$ would be weighted with the two methods, namely weighted estimates and weighted window SEMD.
The sum of all values in every column is 1, therefore the normalization is automatically executed during the weighting process. In the weighted window process all samples are multiplied by a specific factor according to their distance within the step size (the rows of the example in the tables). On the other hand, the samples within the step size are weighted equally using the weighted estimates SEMD technique. The 20 weights of wwSEMD arranged according to their sample positions would result in a normalized discrete Gaussian distribution with window length $M = 20$.
As a means of comparison, both methods will, in the following, be applied to toy

	k = 1	**k = 2**	**k = 3**	**k = 4**
e = 1	0	0	0	0
e = 2	0.23202	0.23202	0.23202	0.23202
e = 3	0.53596	0.53596	0.53596	0.53596
e = 4	0.23202	0.23202	0.23202	0.23202
e = 5	0	0	0	0

Table 4.1 Weights of weighted estimates SEMD example for the parameters $M = 20$, $E = 5$ and $K = 4$ (see gray area of fig. 4.6 (bottom)). The normalization is already included, as the weights of every column add up to 1.

	k = 1	**k = 2**	**k = 3**	**k = 4**
e = 1	0.08779	0.04596	0.01771	0
e = 2	0.35631	0.28435	0.21060	0.14361
e = 3	0.41229	0.44138	0.44138	0.41229
e = 4	0.14361	0.21060	0.28435	0.35631
e = 5	0	0.01771	0.04596	0.08779

Table 4.2 Weights of weighted window SEMD example for the parameters $M = 20$, $E = 5$ and $K = 4$ (see gray area of fig. 4.6 (bottom)). The normalization is already included, as the weights of every column summarized yield 1.

data, in order to asses their reconstruction quality. A thorough examination of the (weighted) Sliding EMD algorithm with toy data will be performed in chapter 5.

4.4.3 Comparison between the Performance of weSEMD and wwSEMD

In this section the performance of weighted estimates and weighted window SEMD will be compared. Therefore, toy data given by $x(t_n)$ will be decomposed with both methods and the IMFs $c_l(t_n)$ will be compared to the original components $x_l(t_n)$ via the mean squared error (MSE):

$$MSE = \frac{1}{N}\sum_{n=1}^{N}\big(x_l(t_n) - c_l(t_n)\big)^2 \tag{4.11}$$

As the original components have to be known for a quantitative analysis, two different sets of toy data will be analyzed in this section.

The first toy data example, which has already been presented in section 4.1, is

composed of a superposition of four components: a sawtooth wave, a sinusoid, a cosine function with time-dependent frequency content and a monotonous trend (illustrated in fig. 4.1). The time series is formed by $N = 40\,000$ samples and the time scale is $t_n = 0, \ldots, 19.9995$ with $\Delta t_n = 0.0005$. The toy example is decomposed by weSEMD and wwSEMD with a window size $M = 2500$ and varying step size K covering all divisors of M.

In figure 4.9 the MSE averaged over component $1 - 3$ between the original components and the IMFs is displayed with respect to the ensemble size of the decomposition with wwSEMD and weSEMD. For small ensemble sizes an increase of the MSE for the wwSEMD decomposition method is observable. Beginning with $E = 20$ the reconstruction quality of wwSEMD and weSEMD remains continuously high. Supposedly the MSE of wwSEMD raises for small ensemble sizes in contrast to weSEMD, because in that case the ends are suppressed better with the latter technique. Since weSEMD multiplies the first and last K samples of every window with the weighting factor 0.

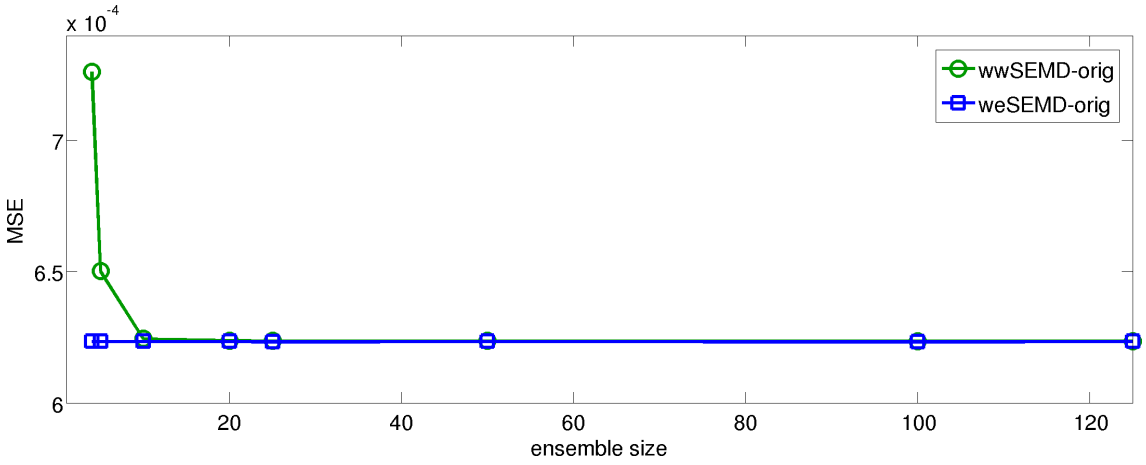

Figure 4.9 The MSE between the original components and the IMFs averaged over components $1 - 3$ is illustrated depending on the ensemble size of the decomposition with wwSEMD and weSEMD ($M = 2500$).

The second toy example consists of three components that will be treated as two, because component 1 and 2 have a very similar frequency in order to create a beating wave. The components are: the sum of two sine functions

- $x_1(t_n) = \sin(2 \cdot t_n)$,
- $x_2(t_n) = \sin(1.7 \cdot t_n)$

and a monotonous trend:

- $x_3(t_n) = 0.04 \cdot t_n - 1$

The time series is formed by $N = 100\,000$ samples and the temporal scale is $t_n = 0, \ldots, 49.9995$ with an interval of $\Delta t_n = 0.0005$ between the samples. The toy data time series is chosen longer in this case, due to its low frequency, to capture more periods of the function, but maintain the sampling rate. The toy data example is illustrated in figure 4.10.

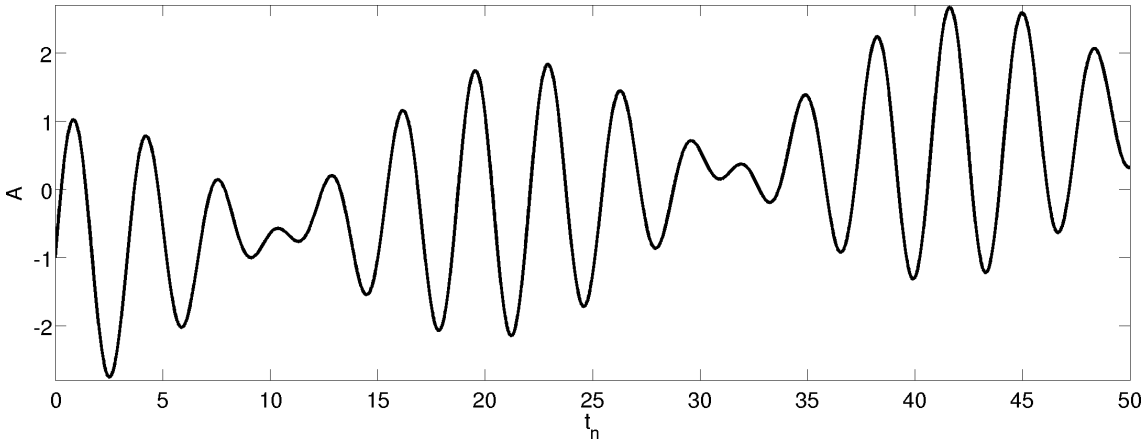

Figure 4.10 The second toy data example consisting of two oscillating components $x_1(t_n) = \sin(2 \cdot t_n)$ and $x_2(t_n) = \sin(1.7 \cdot t_n)$, which together form a beating wave, and a trend $x_3(t_n) = 0.04 \cdot t_n - 1$. The ordinate gives the amplitude A of the time series and the abscissa depicts the temporal scale t_n.

The toy example is decomposed with wwSEMD as well as with weSEMD with $M = 15\,000$ applying a multitude of ensemble sizes, namely all divisors of M. The window size is selected longer as well in this case, due to the lower frequency of the data. In figure 4.11 the MSE between the sum of the original components 1 and 2 and IMF 1 is visualized. The MSE is presented with respect to the ensemble size for both decomposition methods wwSEMD and weSEMD. In this example – except for ensemble size $E = 3$ – the situation is now reversed. For small ensemble sizes the MSE of the IMF decomposed with weSEMD is not constant any more, however it is even higher than the one of the wwSEMD decomposition. Also in this toy data example the reconstruction quality remains uniformly high beginning with an ensemble size of about $E = 30$.

The main difference between the two toy data examples is their frequency content. The first example exhibits high-frequency components, whereas the second example

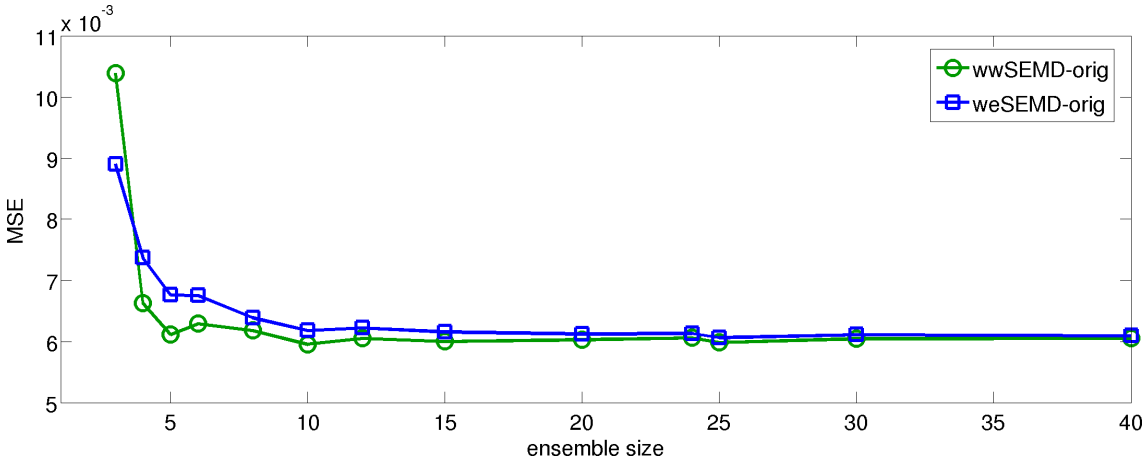

Figure 4.11 The MSE between the original components and IMF 1 of the second toy data example is illustrated depending on the ensemble size of the decomposition with wwSEMD and weSEMD ($M = 15\,000$).

features a low-frequency component together with a trend. The explanation for the relatively high MSE of the IMFs of weSEMD will be given in the following section.

4.4.4 Difficulties of Weighted Estimates SEMD

In this section some problems of weighted estimates SEMD arising under certain circumstances will be illustrated and analyzed. The toy data example utilized for this examination consists of a beating wave and a trend and has already been presented in the previous section (visualized in fig. 4.10). A very similar frequency was chosen for components 1 and 2 in order to create a beating wave with only little slope in certain sections of the time series. Therefore, the two modes are regarded as one component. The signal length is $N = 100\,000$ and $t_n = 0, \ldots, 49.9995$ with an interval of $\Delta t_n = 0.0005$ between the samples. The example is decomposed with weighted estimates and weighted window SEMD, respectively, using a window size of $M = 15\,000$ and a step size of $K = 3000$ resulting in an ensemble size of $E = 5$. The small ensemble size is selected in order to be able to investigate the problems emerging for weighted estimates SEMD for small amounts of estimates and data with only sparse slope. In figure 4.12 IMF 1 of the decomposition with weighted estimates and weighted window SEMD is illustrated giving an overview and a detailed impression of the graph.

It is ostentatious that in intervals of $t_n = 1.5$ (which results in $n = t_n/\Delta t_n = 3000$ samples) discontinuities occur in different magnitudes in the plotted IMF of

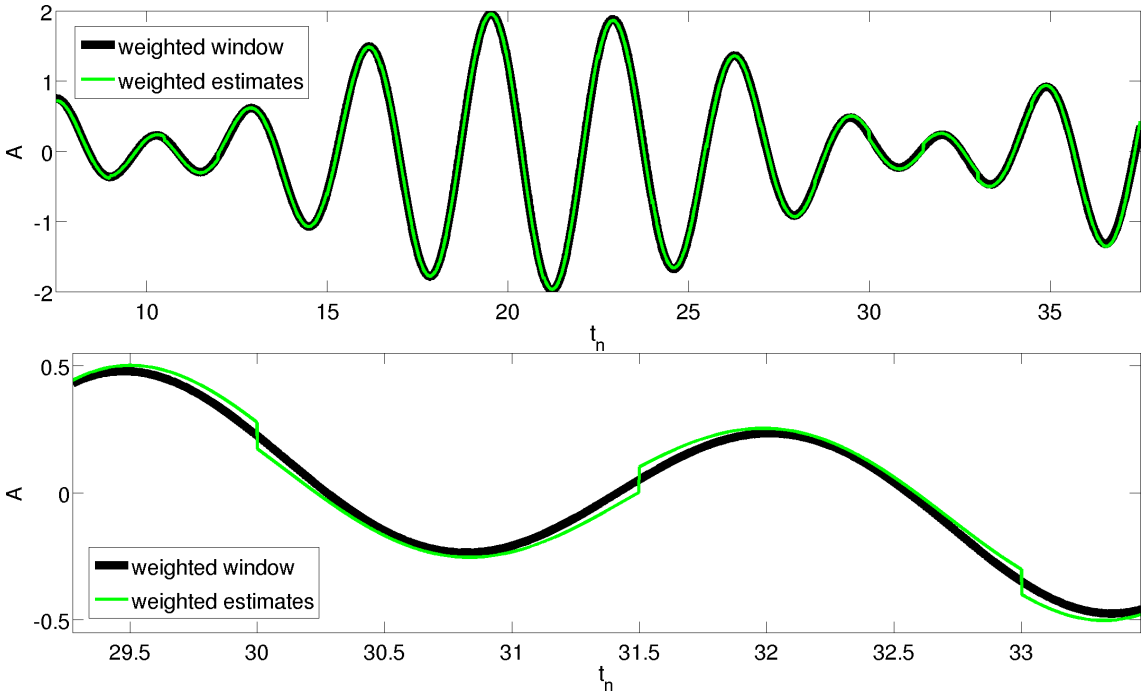

Figure 4.12 IMF 1 of the toy data example decomposed with weighted estimates (green) and weighted window (black) SEMD. In the top plot one can observe discontinuities occurring regularly after multiples of $t_n = 1.5$, respectively, $n = 3000$ samples. In the bottom graph a detail of the two IMFs displays that fact more clearly. The ordinate gives the amplitude A of the time series and the abscissa depicts the time scale t_n.

the weighted estimates SEMD decomposition, whereas the weighted window SEMD decomposition yields a smooth time series in this area. The amount of 3000 samples complies with the step size K.

To further investigate that behavior, a closer look at the first discontinuity at $t_n = 9$ is taken (see figure 4.13). Note that the first and last M samples are omitted by any SEMD algorithm because of the incomplete ensemble of estimates.

Apparently the break stems from the weighted estimates weighting process. Therefore, the single windows, hence the various estimates, will be surveyed thoroughly. In figure 4.14 the first IMFs of the single windows decomposed with EMD are displayed. The different colors denote the various windows, while at $t_n = 9$ window 2 ends and window 7 starts (green lines). The samples $7.5 < t_n \leq 9$ stand for the first $K = 3000$ time points of the data and the samples $9 < t_n \leq 10.5$ for the second K time points.

In figure 4.15 the different windows are illustrated more closely at $t_n = 9$. Additionally, the weights of every sample at the point $t_n = 9$ ($n = 3000$) and at $t_n = 9.0005$

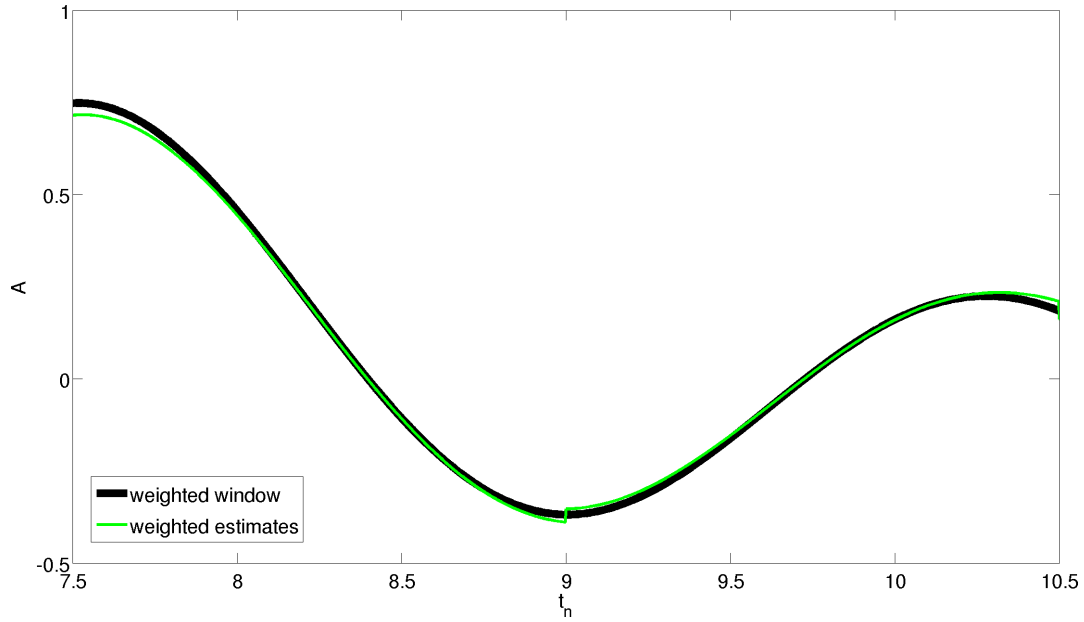

Figure 4.13 The first discontinuity of IMF 1 of the toy data example decomposed with weighted estimates (green) and weighted window (black) SEMD with $M = 15\,000$ and $K = 3000$ after $t_n = 9$ time points, respectively, $n = 18\,000$ samples (note that the first window is omitted completely by any SEMD decomposition). The ordinate gives the amplitude A of the time series and the abscissa depicts the temporal scale t_n.

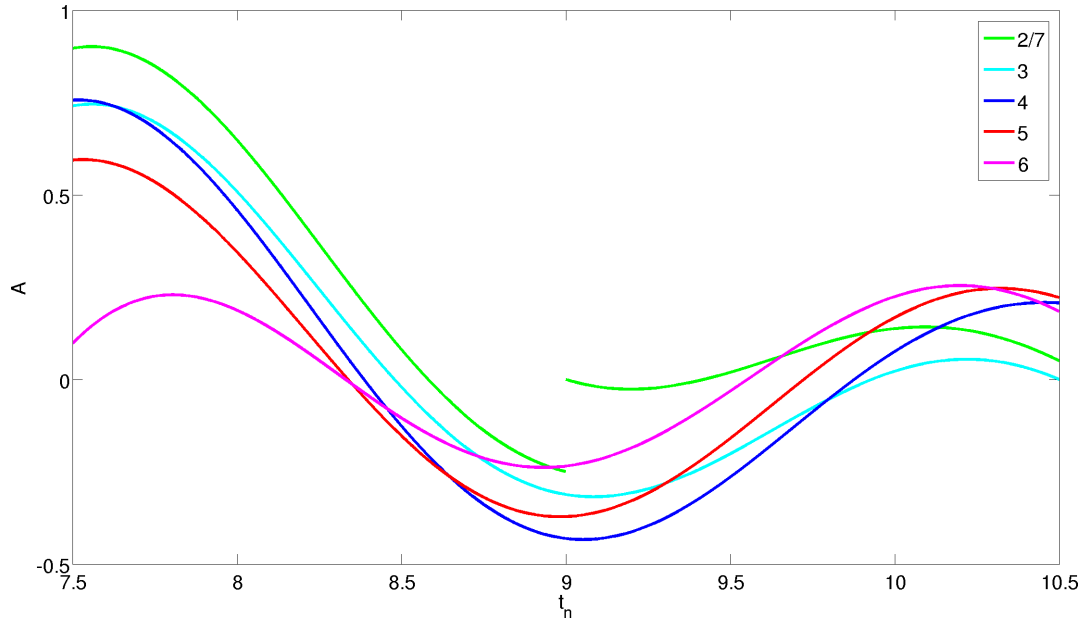

Figure 4.14 The first IMFs of the single windows decomposed with EMD. The colors highlight the different windows. At $t_n = 9$ the end of window 2 is reached and window 7 starts. At any time point $E = 5$ different estimates are present. The ordinate gives the amplitude A of the time series and the abscissa depicts the temporal scale t_n.

($n = 3001$) are displayed in black for weighted estimates (see fig. 4.15, top) and weighted window (see fig. 4.15, bottom) SEMD. In both cases the end of window 2 and the beginning of window 7 are weighted with the factor:

$$p_G^{(E_W)}(t_1) = p_G^{(E_W)}(t_E) = p_G^{(M_W,1)}(t_{m,1}) = p_G^{(M_W,K)}(t_{m,E}) = 0$$

Because within K data points all samples are equally weighted by weighted estimates SEMD, window 2 is suppressed by the factor 0 in the complete first half of the plot and the same applies for window 7 and the second half.
The K subsequent data points of the window will in the following be denoted as parts 1-5 depending on their position within the window as illustrated in figure 4.16. Figure 4.15 (top) shows, that in the second half of the plot the weighting factors switch from 0 to 0.23202 in window 6. That means, that in the second half of the plot part 2 of window 6, instead of part 1 like in the first half of the plot, is now present. The values of the estimates in part 2 of the window are given more weight, than the estimates in part 1.
An overview of the switch of the parts of the windows and their corresponding switch of the weighting factors is given in table 4.3 for weighted estimates SEMD and in table 4.4 for weighted window SEMD. In the case of weSEMD this switching results in an abrupt change of the factors, when multiplying the weighting factors with the amplitude values $A(t_n)$.

window 2/7	part 5 → part 1	0.00000 → 0.00000
window 3	part 4 → part 5	0.23202 → 0.00000
window 4	part 3 → part 4	0.53595 → 0.23202
window 5	part 2 → part 3	0.23202 → 0.53595
window 6	part 1 → part 2	0.00000 → 0.23202

Table 4.3 The table shows an overview of the weighting process by weSEMD of the individual parts of the windows with their specific weights and the abrupt switch after $K = 3000$ samples.

The calculation of $A_{\text{final}}(9)$ and $A_{\text{final}}(9.0005)$ yields:

$$\begin{aligned} A_{\text{final}}(9) &= 0 \cdot (-0.24953) + 0.23202 \cdot (-0.31159) + 0.53595 \cdot (-0.43069) + \\ &\quad 0.23202 \cdot (-0.37143) + 0 \cdot (-0.23471) = -0.38930 \\ A_{\text{final}}(9.0005) &= 0 \cdot (0.00013) + 0 \cdot (-0.31166) + 0.23202 \cdot (-0.43074) + \\ &\quad 0.53595 \cdot (-0.37142) + 0.23202 \cdot (-0.23465) = -0.35345 \end{aligned}$$

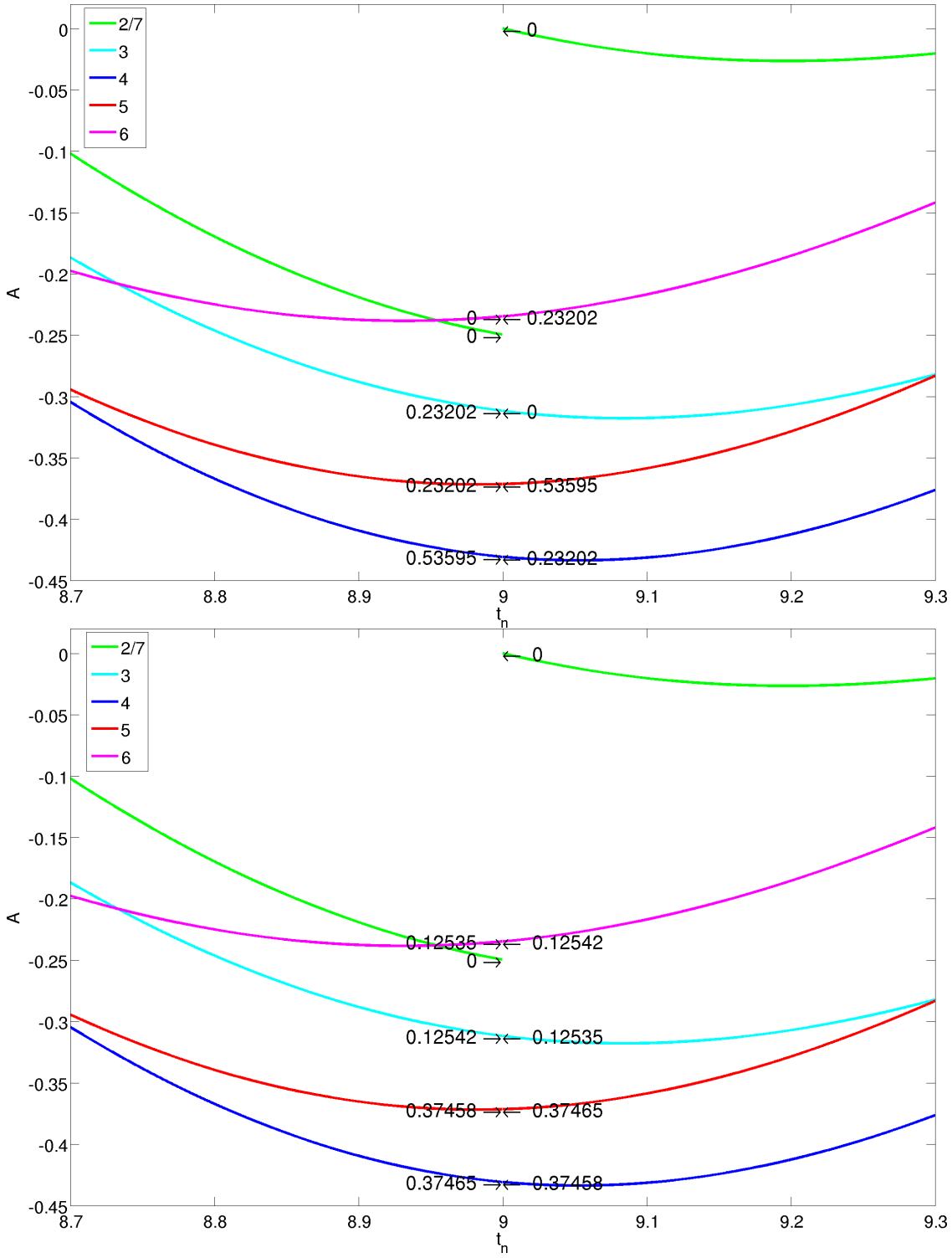

Figure 4.15 Depicted are the weights of weighted estimates (top) and weighted window (bottom) SEMD used to multiply with the values $t_n = 9$ and $t_n = 9.0005$ of the IMF. The ordinate gives the amplitude A of the time series and the abscissa depicts the temporal scale t_n.

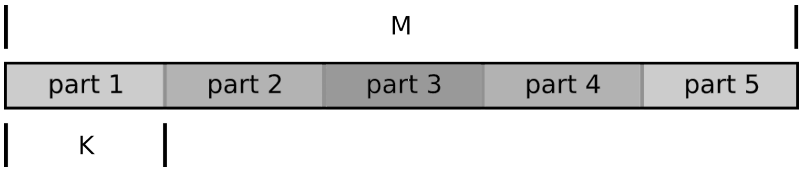

Figure 4.16 The window ($M = 15\,000$) is partitioned into $E = 5$ parts with a sample size of $K = 3000$, respectively.

window 2/7	part 5 → part 1	0.00000 → 0.00000
window 3	part 4 → part 5	0.12542 → 0.12535
window 4	part 3 → part 4	0.37465 → 0.37458
window 5	part 2 → part 3	0.37458 → 0.37465
window 6	part 1 → part 2	0.12535 → 0.12542

Table 4.4 The table presents an overview of the weighting process by wwSEMD of the individual parts of the windows with their particular weights and the smooth transition after $K = 3000$ samples.

Since the two neighboring data points of weSEMD at $A_{\text{final}}(9) = -0.38930$ and at $A_{\text{final}}(9.0005) = -0.35345$ differ strongly, the discontinuity is obtained and yields $\Delta A = \mid A_{\text{final}}(9) - A_{\text{final}}(9.0005) \mid = 0.03585$.

Looking at weighted windows SEMD the switch of weighting factors is done smoothly according to the position of the particular sample in the specific window. The amplitude $A(t_n)$ of the end result is thus computed at the points $t_n = 9$ and $t_n = 9.0005$ like this:

$$\begin{aligned} A_{\text{final}}(9) = 0 \cdot (-0.24953) + 0.12542 \cdot (-0.31159) + 0.37465 \cdot (-0.43069) + \\ 0.37458 \cdot (-0.37143) + 0.12535 \cdot (-0.23471) = -0.36899 \\ A_{\text{final}}(9.0005) = 0 \cdot (0.00013) + 0.12535 \cdot (-0.31166) + 0.37458 \cdot (-0.43074) + \\ 0.37465 \cdot (-0.37142) + 0.12542 \cdot (-0.23465) = -0.36900 \end{aligned}$$

The two neighboring data points of wwSEMD at $A_{\text{final}}(9) = -0.36899$ and at $A_{\text{final}}(9.0005) = -0.36900$ do not differ much. Their difference amounts to $\Delta A = \mid A_{\text{final}}(9) - A_{\text{final}}(9.0005) \mid = 0.00001$, and thus the weighting does not yield a discontinuity.

The abrupt change of weighting factors, respectively, the sudden new assignment of weighting factors to different windows yields a discontinuity for weighted estimates SEMD in the end result.

For data with a steep slope these discontinuities are hardly visible. These severe problems only arise with slowly varying data. Looking at figure 4.5 it is obvious that especially in intervals with only little slope, and thus often a small amount of extrema to construct the splines, the estimates contain more outliers than in areas with a steep slope. In these segments of the time series, which mostly exhibit a relatively small amplitude as well, also the boundary effects have a higher impact on the reconstruction of the components. Figure 4.17 illustrates, that the discontinuities do not only appear in decompositions with small ensemble sizes. The decomposition was done with weSEMD and wwSEMD with a window size of $M = 15\,000$ and an ensemble size of $E = 1500$. The differences of the amplitudes at the discontinuities $\Delta A = | A(t_n) - A(t_n + \Delta t_n) |$ are only tiny, hence less noticeable. Again it is obvious that ΔA is larger in areas with only few slope.

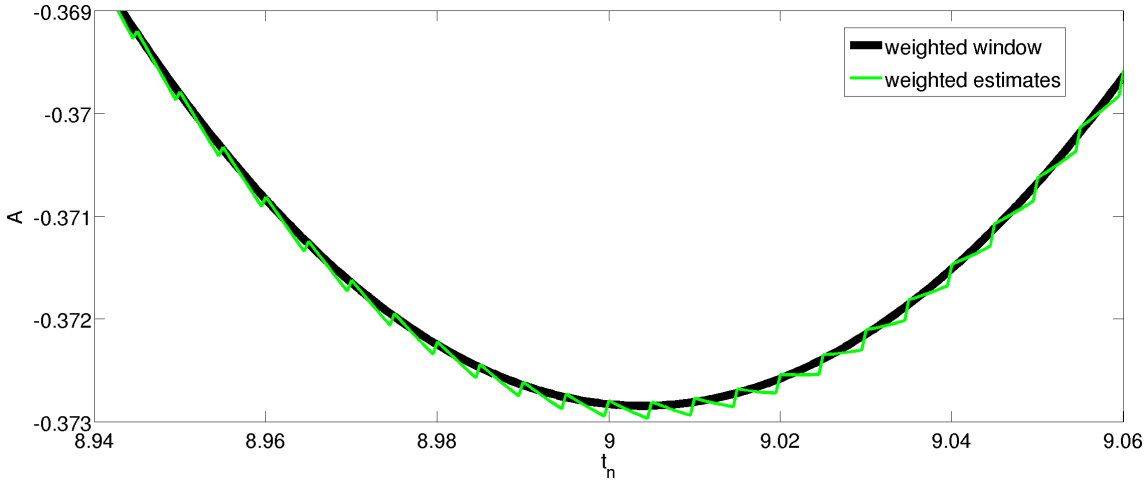

Figure 4.17 Discontinuities of IMF 1 of the toy data example decomposed with weighted estimates (green) and weighted window (black) SEMD with $M = 15\ 000$ and $K = 10$ around $t_n = 9$. The ordinate gives the amplitude A of the time series and the abscissa depicts the temporal scale t_n.

This characteristic of the decomposition is also the reason for the worse performance of weSEMD in contrast to wwSEMD for small ensemble sizes as seen in section 4.4.3.

Although conveniently the decompositions are operated with an ensemble size large enough to keep that problem marginal, those discontinuities cannot be allowed to emerge in the decomposition results. Furthermore, that defect creates a number of additional extrema compromising the compliance of the first IMF criterion. Since Empirical Mode Decomposition is a heuristic algorithm and only few general requirements are defined, it is of importance to adhere to those. The definition of an

IMF to have only one extremum between two subsequent zero crossings can only be obeyed by weighted window SEMD.

Therefore, weighted window SEMD will be used for all further analyses. For convenience it will, from now on, be denoted generally as weighted Sliding Empirical Mode Decomposition (wSEMD).

Chapter 5

Application of wSEMD to Toy Data

After the mechanism and properties of SEMD and wSEMD were introduced, the quality of the methods for practical applications will be proofed by means of toy examples and accordingly with neuromonitoring time series in the next chapter. To be able to assess the behavior, performance and characteristics of SEMD and wSEMD quantitatively, investigations are conducted using toy data at the beginning. By comparing the IMFs and the residuum to the original data components quantitative information, e.g. about the reconstruction quality, can be given.

Several different investigations and tests will be performed in this chapter. SEMD and wSEMD analyses concerning the numerical accuracy, the compliance of the IMF criteria and the influence of window and step size will be conducted. The oscillatory content of the residuum, depending on the window size, and additionally the reconstruction quality with respect to the employed ensemble size will give more information about the characteristics of the newly proposed algorithms. Further, in order to perform a thorough comparison, (w)SEMD will also be examined in contrast to on-line EMD, EEMD (introduced in section 3.5) and conventional EMD to assess their reconstruction quality. Moreover, analyses will be conducted to evaluate the computational load of SEMD and wSEMD quantitatively.

Most of the analyses will be performed in comparison to plain EMD and EEMD. For better comparability the utilized (E)EMD algorithm is identical to the one SEMD uses to decompose the individual windows, which is mainly based on the algorithm that can be found in [21].

5.1 Toy Data

In the following nearly all analyses – if not stated otherwise – are conducted with the toy data example $f(t_n) = x_1(t_n) + x_2(t_n) + x_3(t_n) + x_4(t_n)$, which is depicted in figure 4.1, consisting of:

- $x_1(t_n) = 0.6366 \cdot \arcsin\big(\sin(699 \cdot t_n)\big)$, a sawtooth wave,
- $x_2(t_n) = \sin(327 \cdot t_n)$, a sinusoid,
- $x_3(t_n) = \cos\big(2 \cdot (t_n + 20)^2\big)$, a cosine function with time-dependent frequency, and
- $x_4(t_n) = 0.1 \cdot t_n - 1$, a monotonous trend.

The time series is formed by $N = 40\,000$ samples and the temporal scale amounts to $t_n = 0, \ldots, 19.9995$ with an interval of $\Delta t_n = 0.0005$ between the samples.
All tests will be done for the first 3 IMFs individually and the mean of the results is calculated afterwards. If not stated otherwise, the results will be given averaged over component $1 - 3$ to get an overview over a wider range of the data at once.

5.2 Completeness and Numerical Accuracy

One of the mathematical properties of EMD (see section 3.3.1) and (w)SEMD (see section 4.1) is completeness. As for all numerical applications, an absolutely complete reconstruction cannot be achieved. However, the accuracy of the decomposition can be evaluated apart from numerical errors. The precision of the algorithm is tested, summing up all IMFs $c_l(t_n)$ and the residuum $r(t_n)$

$$x(t_n) = \sum_{l=1}^{L} c_l(t_n) + r(t_n) \tag{5.1}$$

and comparing the result to the original data. The mean squared error (MSE) is used to compute the difference between the original data and the output of the SEMD method. The investigations are implemented with the toy data example $f(t_n)$ introduced before. The MSE is calculated as:

$$MSE = \frac{1}{N} \sum_{n=1}^{N} \big(f(t_n) - x(t_n)\big)^2 \tag{5.2}$$

whereas N denotes the sample size. To be able to compare the results to other EMD techniques the decomposition is calculated with SEMD, wSEMD and EMD. For different decompositions with varying window ($M = 1000, \ldots, 5000$ in steps of 500) and ensemble sizes ($E = 2$, 4, 5, 10, 20, 25, 50, 100, 125, 250, 500) only a very small MSE between the original data and the reconstructed signal is found. The MSE ranges between 10^{-31} and 10^{-28} for SEMD, between 10^{-31} and 10^{-29} for wSEMD and amounts to about 10^{-31} for EMD. These values originate from numerical errors and are many orders of magnitude below the precision of the measured data used later on in this thesis. The decomposition can, thus, be regarded precise aside from those numerical inaccuracies. Since (w)SEMD requires much more individual decompositions it is more prone to error than EMD. All the more the obtained results for this new technique are very good. The basic requirement for the EMD decomposition is, therefore, fulfilled by SEMD and wSEMD.

5.3 Examination of the IMF Criteria

Due to the averaging, which is performed by (w)SEMD to obtain the resulting IMFs, the adherence of the IMF criteria (see section 3.1) is not guaranteed. Moreover, the use of a constant number of sifting steps, instead of a more adaptive stopping criterion, does not take the adherence of the IMF criteria into account. Therefore, it has to be verified experimentally, if the IMFs obey the conditions which have to be fulfilled. In order to evaluate the wSEMD algorithm, first, the local average of the upper and lower envelopes of the IMFs and second, the number of extrema and zero crossings is tested. To illustrate the findings, again the toy data example of section 5.1 is used. The results of the examination of the IMF criteria are shown averaged over the first three components of the used data set and with respect to the ensemble size. For both investigations an exemplary window size of $M = 2500$ and ensemble sizes of $E = 2$, 4, 5, 10, 20, 25, 50, 100, 125, 250, 500 are utilized. In order to be able to compare the results to other techniques, the investigations are also executed with plain EMD and Ensemble EMD (for the used algorithm see [21]) using the same ensemble sizes as for (w)SEMD.

5.3.1 Mean Value

The local average of the upper $U(t_n)$ and lower $L(t_n)$ envelopes $m(t_n)$

$$m(t_n) = \frac{1}{2}\big(U(t_n) + L(t_n)\big) \tag{5.3}$$

is utilized to check, if the mean value is zero, respectively, close to zero. For a meaningful evaluation of the mean value of the IMFs the average of the *absolute* values of $m(t_n)$, for convenience called S

$$S = \frac{1}{N} \sum_{n=1}^{N} \mid m(t_n) \mid \tag{5.4}$$

are depicted in the following, whereas N denotes the number of samples. For a comparison between SEMD, wSEMD, EMD and EEMD figure 5.1 shows S averaged over the first three components which is computed depending on the ensemble size. The results for the EEMD decomposition are worse than those of the other methods, which perform consistently better. SEMD as well as wSEMD show a lower value of S than EMD for all used ensemble sizes. While the parameter S of the SEMD decomposition decreases with increasing E, the mean of the absolute values of $m(t_n)$ of the wSEMD decomposition remains very low throughout all ensemble sizes. Considering the individual IMFs, $\overline{S}$ is calculated averaging S over all ensemble sizes for one particular IMF. The largest $\overline{S}$ for SEMD is obtained by IMF 3 with $\overline{S} = 0.0069$ and by IMF 1 with $\overline{S} = 5.4 \cdot 10^{-4}$ for wSEMD.

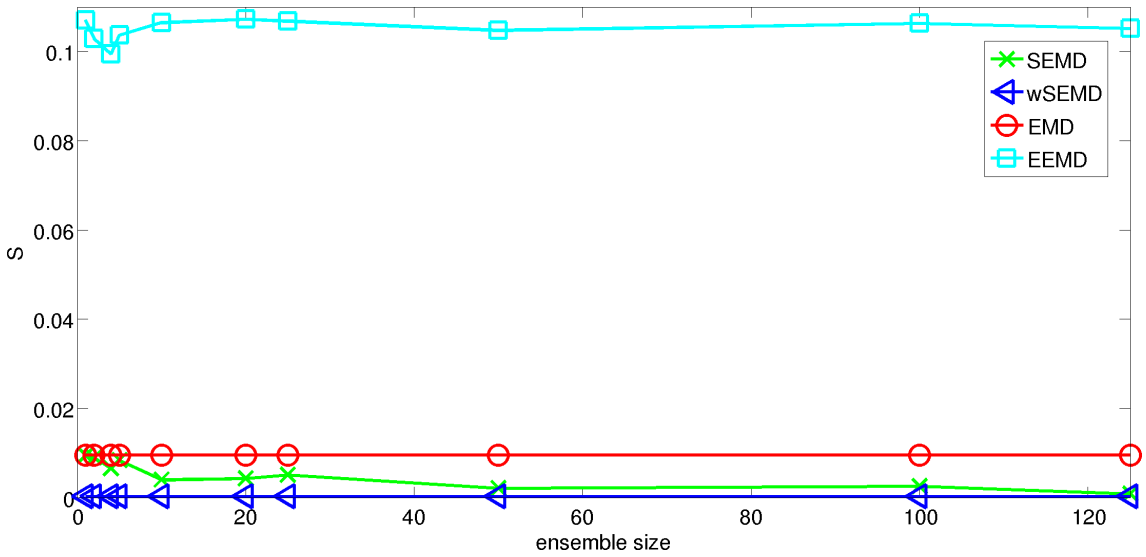

Figure 5.1 The mean of the absolute values of $m(t_n)$, denoted by S, is shown for the SEMD, wSEMD, EMD and EEMD decomposition averaged over the first three components with respect to the ensemble size E.

Comparing the results to EMD one can say, that the first criterion for an IMF is fulfilled for the SEMD and wSEMD decomposition. This toy data example, further-

more, illustrates the high quality of wSEMD stemming from the weighting, which improves the SEMD technique significantly.

5.3.2 Number of Extrema and Zero Crossings

The absolute difference between the number of extrema and zero crossings, depending on the ensemble size, is depicted in figure 5.2, averaged over IMFs $1-3$ of the toy data example. Again results of the SEMD, wSEMD, EMD and EEMD decomposition are plotted, to be able to compare the different techniques. While the EMD decomposition generally fulfills the second defining criterion of an IMF for the displayed toy example, EEMD shows a large difference between extrema and zero crossings (> 75) throughout the ensemble size (see top of fig. 5.2), which is even increasing for larger ensembles. Looking at the more detailed plot it is obvious that the second criterion is not fulfilled for the decomposition with SEMD, however the deviations are only small especially for larger ensemble sizes. The difference between extrema and zero crossings for wSEMD deviates only slightly from the one of EMD, especially for smaller ensemble sizes. These minor differences originate from the potential ruggedness of the signals after the calculation of the average time series. Considering the IMFs individually all exhibited a very similar behavior.
All in all the second IMF criterion is fulfilled by EMD, SEMD and wSEMD except for minor deviations.

5.4 Influence of Window and Step Size

The two parameters of wSEMD, namely the window size M and the step size K, which combine to the ensemble size $E = \frac{M}{K}$, naturally influence the decomposition. Toy data enables a quantitative analysis of their impact. Again the toy example of section 5.1 is employed to visualize the effect of those parameters. The mean squared error (MSE) of one of the original components of the toy data set and the associated resulting IMF of the decomposition with SEMD and wSEMD is computed for different combinations of both parameters. Thus, M ranges from 1000 to 5000 in steps of 500, whereas E varies from 2 to 500, while all values of M are multiples of E. Figure 5.3 illustrates the error dependence on the two parameters demonstrated by the MSE of the comparison between the IMFs of SEMD and wSEMD and original components of the data. The average MSE of the comparisons between the first 3 components to their corresponding IMFs yield the depicted values calculated for every combination of the window and step size.

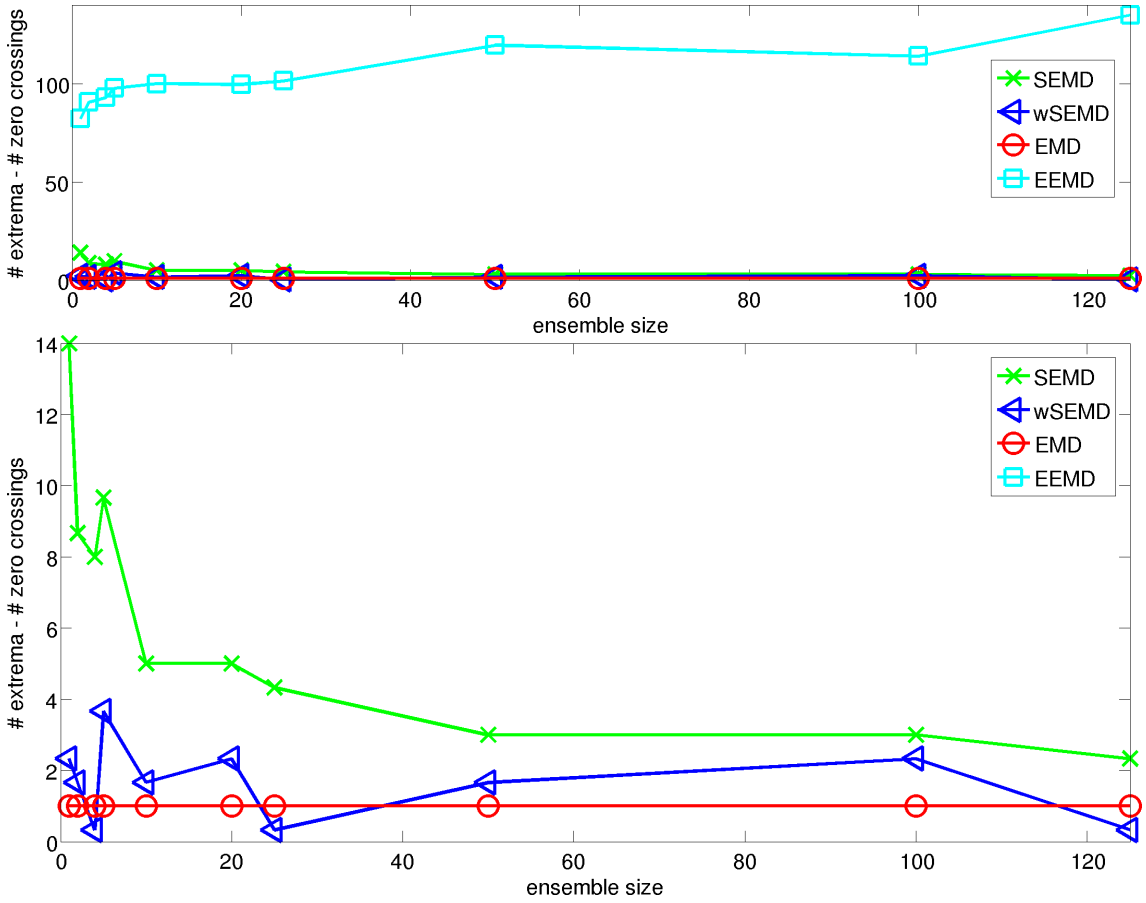

Figure 5.2 The difference between the zero crossings and extrema is shown for the SEMD, wSEMD, EMD and EEMD decomposition averaged over the first three components with respect to the ensemble size E (top) and depicting the SEMD, wSEMD and EMD decomposition in detail (bottom).

The dependence of the MSE on the window and ensemble size is obvious for the SEMD decomposition (fig. 5.3 top). For increasing ensemble size E the mean squared error decreases, as one averages over more data points for the resulting sample and thus more suggestions are available. For larger window sizes the reconstruction of the original components is more precise. That behavior stems form the fact, that in smaller windows the boundary effects take up a larger percentage of the window (see section 3.4.3) and therefore the reconstruction quality worsens. Averaged over all tested combinations of window and ensemble sizes the mean MSE of the SEMD decomposition amounts to $9.7 \cdot 10^{-4}$. Regarding all IMFs individually the hightest mean MSE is calculated for IMF 2, namely $15 \cdot 10^{-4}$.

For the wSEMD decomposition (fig. 5.3 bottom) one can observe that the window size as well as the ensemble size have nearly no effect on the MSE values which are

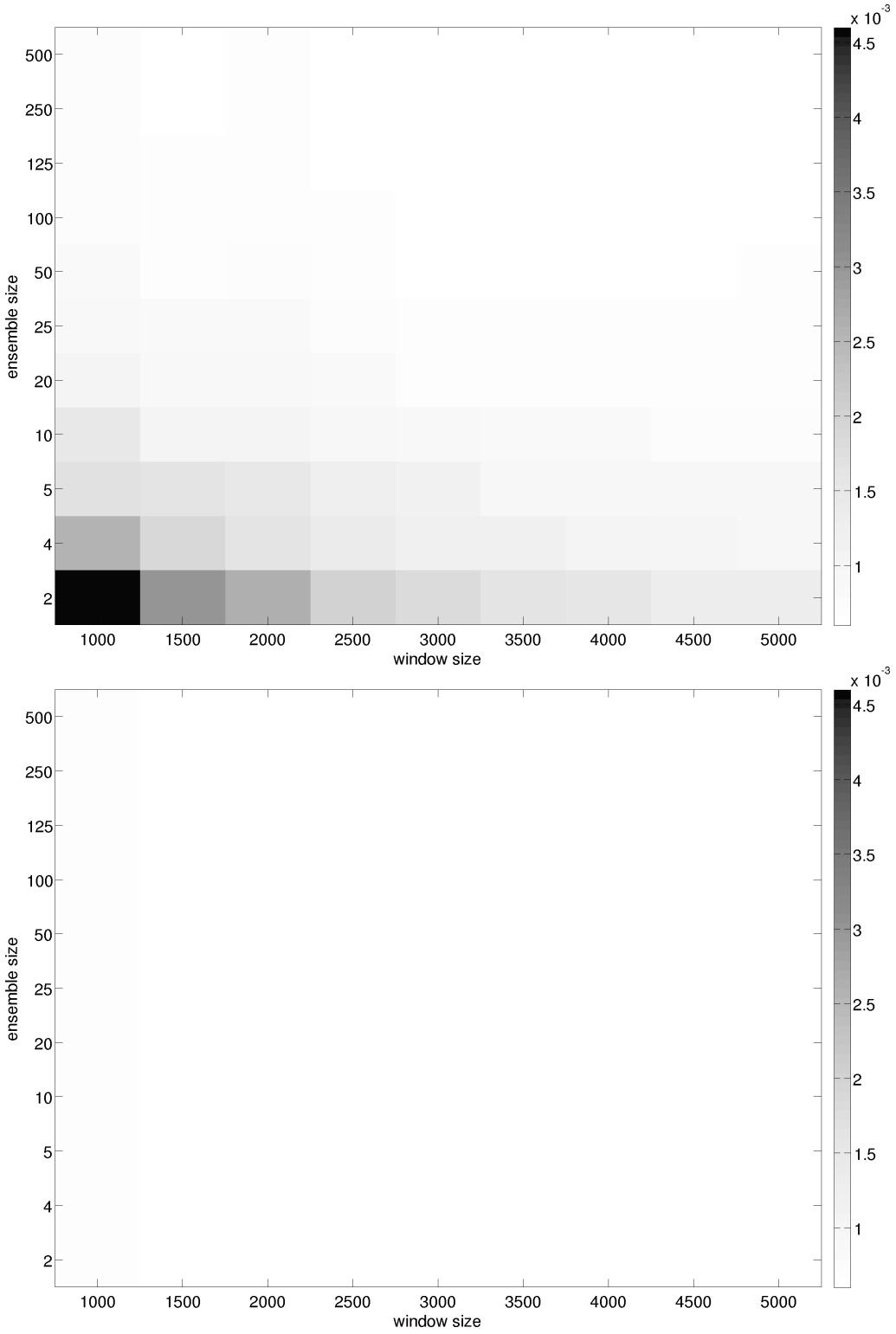

Figure 5.3 MSE between the original components and the IMFs of SEMD (top) and wSEMD (bottom) for different combinations of window and ensemble sizes averaged over the first three IMFs. The MSE of wSEMD is very small and stable compared to SEMD.

generally very small. Averaged over all combinations of window and ensemble sizes, the mean MSE yields $6.2 \cdot 10^{-4}$. For the single IMFs, again, IMF 2 reaches the worst mean MSE, namely $9.5 \cdot 10^{-4}$. The weighted version of the algorithm enhances the reconstruction quality by far. Comparing the mean MSEs of both techniques, the one produced by wSEMD amounts only to 64 % of the one of SEMD. As the ensemble size hardly affects the MSE, for practical applications a smaller ensemble size can be selected and thus computational load can be decreased. Since the computing time is reduced and the reconstruction quality is, in general, increased, wSEMD is to be preferred over SEMD.

5.5 Influence of the Window Size on the Oscillations in the Residuum

The residua of SEMD and wSEMD may contain periodic components, if the periodicity is larger than the selected window size. Components with a periodicity smaller than the window size are extracted as respective IMFs. To be able to evaluate the behavior of wSEMD in an intermediate range of periodicities, a different set of toy data is selected as an example.

The toy signal $x(t_n) = \sin(2\pi \cdot t_n)$ with an interval of $\Delta t_n = 0.0005$ between the samples consists of a sinusoid with a period of $T = 2000$ data points. Additionally, a time series of uniformly distributed noise consisting of random numbers $-0.1 \leq n(t_n) \leq 0.1$ with an amplitude corresponding to 10 % of the maximal amplitude of the sinusoid is created. It is added to the toy example to simulate real data and add more extrema. Subsequently, the data is decomposed with wSEMD. Different segment sizes $M = 50, \ldots, 5000$ are considered, whereas the ensemble size $E = 50$ is kept constant for all runs of the algorithm, and the central 30 000 data points (of 40 000 originally) are considered for the analysis. Eventually, the mean squared error (MSE) of the residuum compared to the sine function is computed as can be seen in figure 5.4.

With increasing window size the MSE increases discontinuously, because the amplitude of the sine function decreases as it is split up into the residuum and an IMF. Three sectors of the graph are observable: The sinusoid resides entirely in the residuum for window sizes $0 < M \leq 1000$, corresponding to $0 < M \leq 0.5 \cdot T$, approximately. The sinusoidal component is recovered completely in an IMF for roughly $M \geq 2000$, corresponding to $M \geq T$. In the intermediate sector, where $1000 < M < 2000$, respectively, $0.5 \cdot T < M < T$, mode mixing appears, so that

part of the sinusoid is found in an IMF while the rest of the oscillation resides in the residuum.

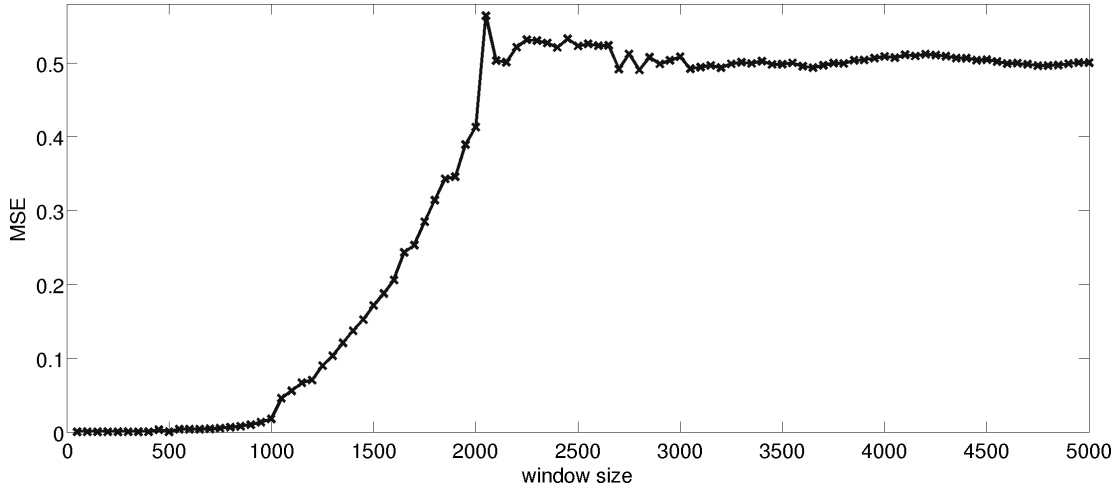

Figure 5.4 Mean squared error (MSE) of the residuum compared to the sinusoidal toy data as a function of the window size. The number of estimates for every wSEMD decomposition amounts to $E = 50$.

Depending on which oscillatory components of the original signal are supposed to appear in the IMFs, an appropriate window size has to be chosen when applying (w)SEMD. The two limits for the window size roughly amount to $0.5 \cdot T$ and T. If oscillations with period T are supposed to be found in the residuum, the window size should be smaller than $0.5 \cdot T$, and larger than T, if the latter are supposed to remain in an IMF. However, they should be experimentally verified for the specific practical application.
Applying the window size parameter carefully, the SEMD/wSEMD decomposition can be employed as a low-frequency filter and potentially the residuum can be utilized as the resulting component for further analyses instead.

5.6 Performance Evaluation

With toy data examples the possibility to examine the decomposition quality of an algorithm is given. Hence, the performance evaluation of SEMD and wSEMD compared to EMD, on-line EMD and EEMD is conducted using the toy example superposing a sawtooth, a sine and a cosine function with changing frequency and additionally a monotonous trend, which was already introduced in detail in section 5.1. As pointed out before, an early on-line version of EMD exists and was briefly

mentioned by Rilling *et al.* in [15]. Therefore, SEMD and wSEMD are compared to this on-line EMD as well (for the algorithm see [62]).
After the decompositions implemented with different ensemble sizes $E = 2$, 4, 5, 10, 20, 25, 50, 100, 125, 250, 500 and an exemplary window size of $M = 2500$ the mean squared error (MSE) between the IMFs and the corresponding signal component is calculated. This test is performed in order to quantify the reconstruction error of the specific oscillating mode. Figure 5.5 shows the findings averaged over IMFs, respectively, components $1 - 3$.

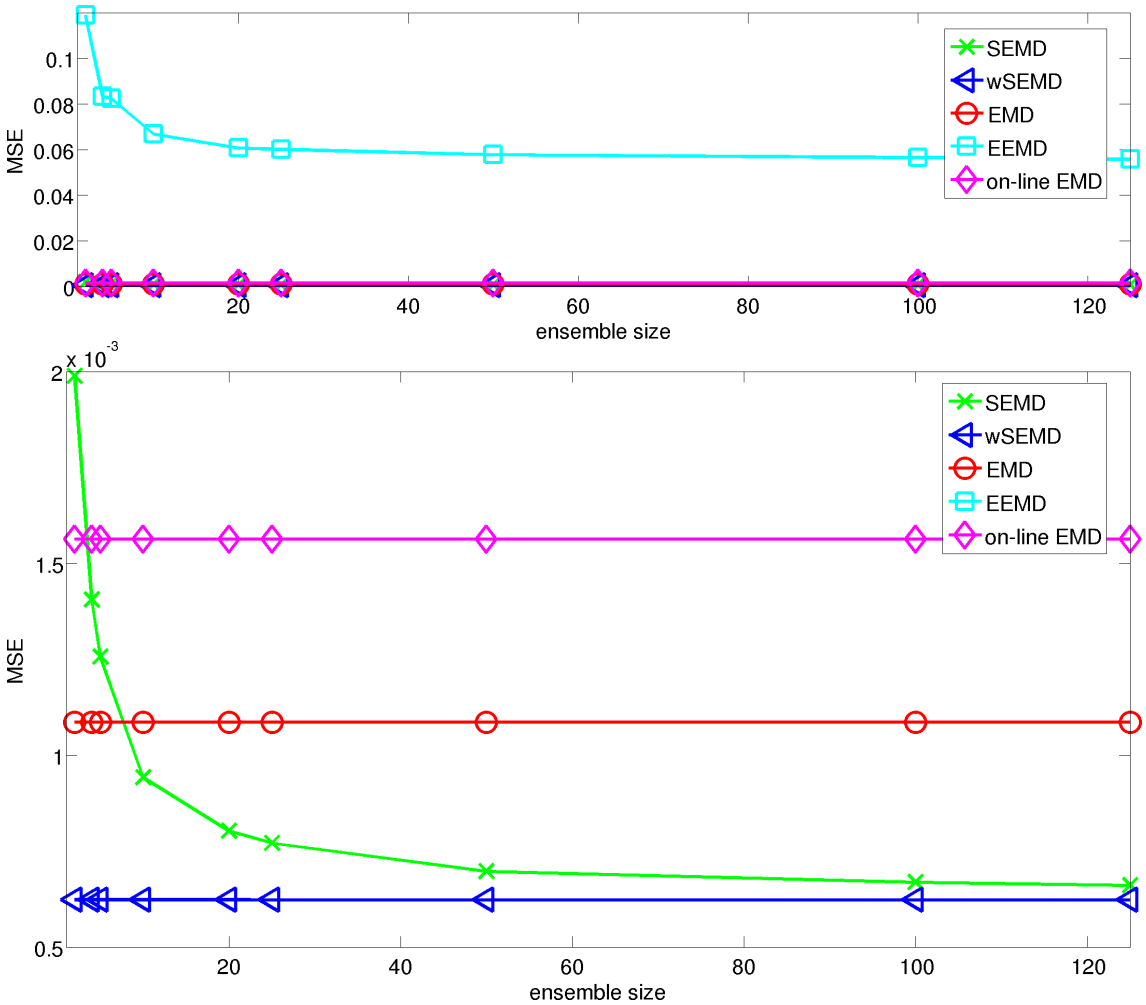

Figure 5.5 MSE between the original components and IMFs averaged over component $1 - 3$ for the SEMD, wSEMD, EMD, on-line EMD and EEMD decomposition (top) and a detailed view (bottom).

Again, the EEMD decomposition lacks reconstruction quality with respect to the other EMD techniques. Also on-line EMD performs worse than EMD. For

SEMD – as expected – the decrease of the MSE is obvious with increasing ensemble size, whereas for wSEMD it is low for all values of E. Especially for small ensemble sizes the improvement of wSEMD in contrast to SEMD is evident.
The wSEMD and for larger ensemble sizes ($E > 10$) also the SEMD method yield even better results than EMD and they, therefore, perform also better than on-line EMD, while the reconstruction quality is clearly best for the decomposition with wSEMD. For online applications SEMD/wSEMD should, thus, be preferred over on-line EMD, since it clearly seems problematic.
Taking the individual IMFs into account, their mean MSEs are computed averaged over all ensemble sizes. For SEMD the highest value is reached for IMF 2, namely $14 \cdot 10^{-4}$ (in contrast to $9.4 \cdot 10^{-4}$ for all three IMFs) and for wSEMD it amounts to $9.6 \cdot 10^{-4}$ also for IMF 2 (with $6.2 \cdot 10^{-4}$ for all three IMFs).
For ensemble sizes beginning with $E = 50$ the MSE of both methods SEMD and wSEMD remains approximately constant representing a good trade-off between reconstruction quality and computational load. All in all one can say, that the performance of the new methods SEMD and especially wSEMD is very good.

5.7 Computational Load

Another characteristic of the new techniques worth exploring is the computational load necessary to obtain results. To be able to classify the computing time a comparison between SEMD, wSEMD, EMD and EEMD is performed as before. Again the toy data example introduced in this chapter is utilized for this investigation and all results are presented averaged over IMFs $1 - 3$.
All programs were run on the same machine under equivalent circumstances on only one processor core. All calculations depend on computational power (processor, main storage, etc.), the implementation (programming language, skillful coding, parallelization, measuring time itself, parameters etc.) and, of course, on the data itself (amount of noise, intrinsic frequencies, etc.). Thus, not the absolute run times, but only the relation between them is of interest and significance. Therefore, all results are compared only qualitatively in the following.

5.7.1 Ensemble Size

First, the attention is turned to the influence of the ensemble size on the computational load. It is expected, that the calculating period increases linearly with the ensemble size for EEMD. Further, it is anticipated that it depends on M and as well

linearly on K, respectively, E for SEMD and wSEMD, since the number of windows W to be decomposed is

$$W = \frac{N - M}{K} + 1 \tag{5.5}$$

for a fixed data length. The latter is set to $N = 40\,000$ for these analyses with SEMD, wSEMD, EMD and EEMD. Several decompositions with different ensemble sizes ($E = 1, 2, 4, 5, 10, 20, 25, 50, 100, 125, 250, 500, 625, 1250, 2500$) are done using a fixed window size of $M = 2500$ for SEMD and wSEMD. All decompositions with the different parameters are executed eight times and the average duration is presented in figure 5.6. The error bars mark the standard deviation of the computation times. Because SEMD, wSEMD and EEMD are ensemble based methods, only a comparison between those is truly equivalent.

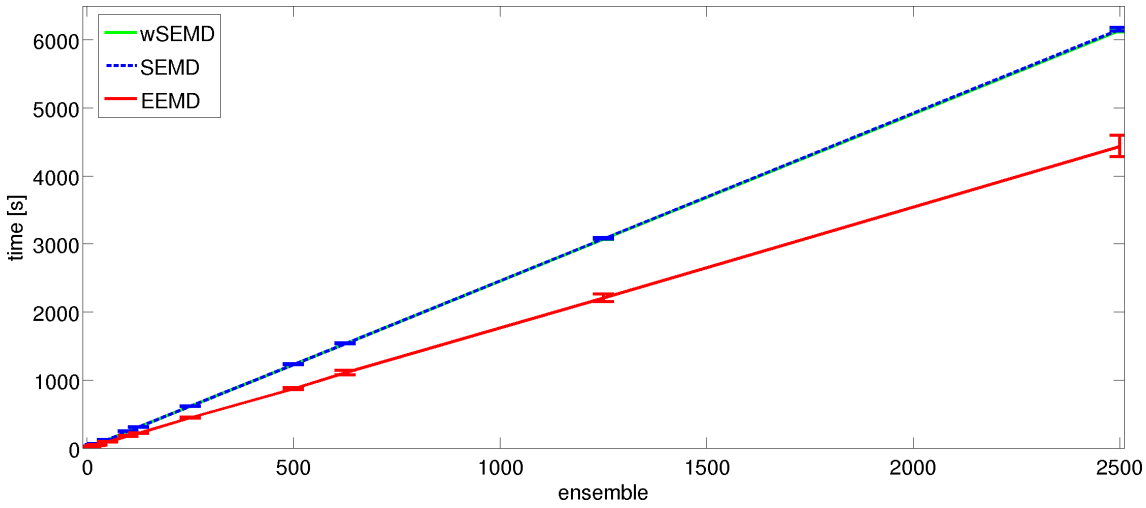

Figure 5.6 The average duration of the decompositions with SEMD, wSEMD and EEMD with respect to the ensemble size is presented. The error bars mark the standard deviations of the eight single computational loads.

As expected the computational loads of all decomposition techniques increase linearly with increasing ensemble size. SEMD and wSEMD perform nearly equally fast, a difference between the durations of the calculations is hardly recognizable. However, EEMD calculates the decompositions slightly faster, at least for this particular sample size of the time series. An analysis about the computational load in relation to the length of the data will follow in the next section. Besides, the by far better reconstruction quality of SEMD and wSEMD renders the slightly increased computational load acceptable.

To be able to assess the contrast to EMD as well, all EMD techniques are tested

for the ensemble size $E = 1$, too, although the analysis with that particular value of the parameter is not reasonable and thus not recommended. The computational load for that parameter setting, averaged over 24 computations and a data length of $N = 40\,000$ samples, is presented in figure 5.7. The error bars, again, mark the standard deviations of the single trials. It is obvious that the computational load of wSEMD and SEMD and that of EMD and EEMD are similar. The calculation periods of the two online methods is slightly higher than those of the decompositions based on the whole time series. However, one has to keep in mind, that for real world applications e.g. to biomedical neuromonitoring data with time series of billions of data points and the necessity of real-time analysis, it is hardly possible to apply EMD or EEMD. An online technique is of vital importance in this field which clearly constitutes the advantage of weighted Sliding EMD.

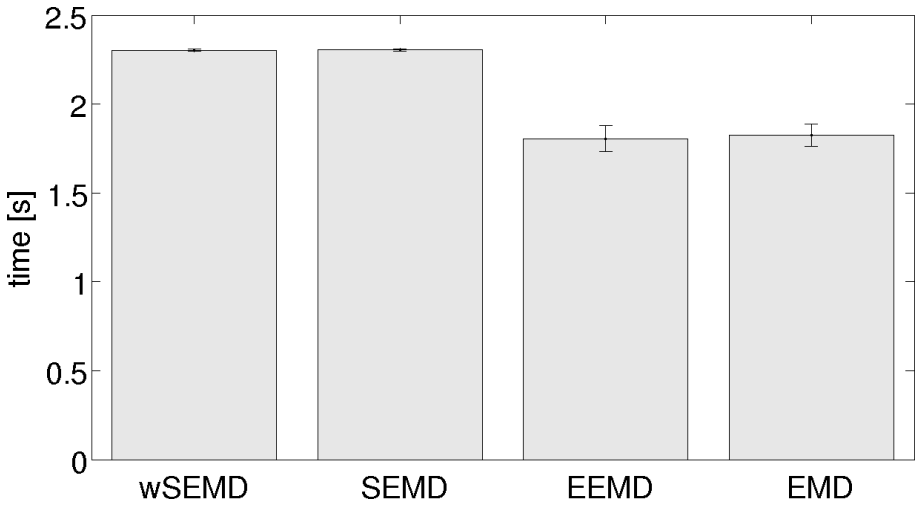

Figure 5.7 The average duration of the decompositions with SEMD, wSEMD, EEMD and EMD using the parameter $E = 1$ is illustrated. The error bars mark the standard deviations of the 24 single computational loads.

5.7.2 Data Length

One problem to be solved in this thesis is the handling of very long biomedical time series with EMD. As the main memory of a computer cannot deal with any number of samples in a data set, an online technique has to be applied to analyze long time series. It is not possible to decompose the neuromonitoring data recorded over days and weeks with EMD (see chapter 7). Furthermore, if the number of IMFs is not kept constant, the number of IMFs will increase with the data length decomposing

real data, as more and more longterm variations have to be taken into account. Additionally, the analysis results for the often instable patients have to be obtained as early as possible, optimally in real-time, for which case an online approach is required.

To have a closer look, a study of computation time with respect to the data length is performed, to be able to estimate the computational cost of the decomposition of long time series with the different EMD methods. Again wSEMD, EMD and EEMD are compared and all tests are implemented with the previously introduced toy data set. SEMD is omitted here, because of its similarity to wSEMD concerning the computational load.

The number of samples of the time series is varied between $N = 25 \cdot 10^3$, $50 \cdot 10^3$, $100 \cdot 10^3$, $500 \cdot 10^3$, $750 \cdot 10^3$, $1 \cdot 10^6$, $2 \cdot 10^6$, $4 \cdot 10^6$, $8 \cdot 10^6$ and $16 \cdot 10^6$ and the ensemble sizes $E = 1$, to be able to compare wSEMD and EEMD to plain EMD, and $E = 50$, which is suitable for practical applications, are used. All computations are executed eight times and are averaged afterwards.

Figures 5.8 (ensemble size $E = 1$) and 5.9 (ensemble size $E = 50$) display the computational load with respect to the length of the time series. The error bars label the standard deviations of the computational times. In both cases, $E = 1$ and $E = 50$, for up to $N = 4 \cdot 10^6$ data points the computational loads of EMD, EEMD and wSEMD increase linearly and equivalently. Beginning with $N = 4 \cdot 10^6$ for EEMD and $N = 8 \cdot 10^6$ for EMD the situation changes and the calculation time for EMD and EEMD increases more than linearly in contrast to wSEMD. As expected, also for those high sample sizes, the increase of computational load of wSEMD still remains linear.

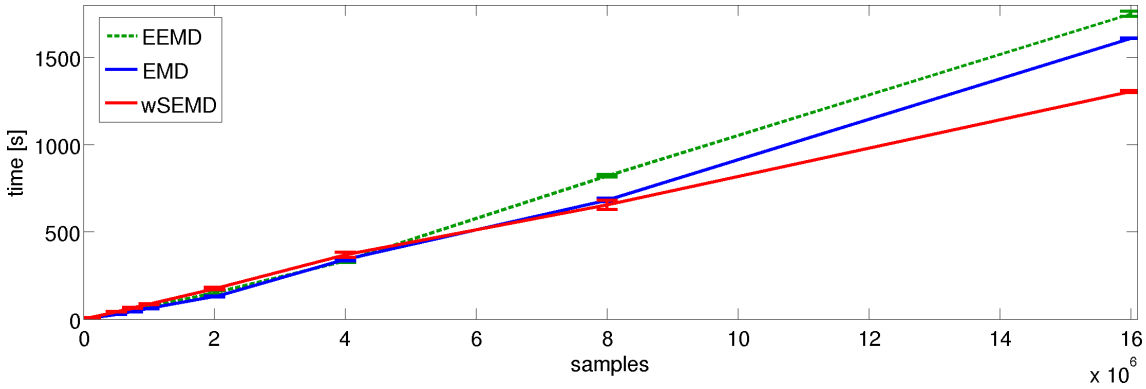

Figure 5.8 An analysis of the computational load of the wSEMD, EMD and EEMD decomposition with ensemble size $E = 1$ is presented with respect to the data length. The error bars mark the standard deviations of the eight single computational loads.

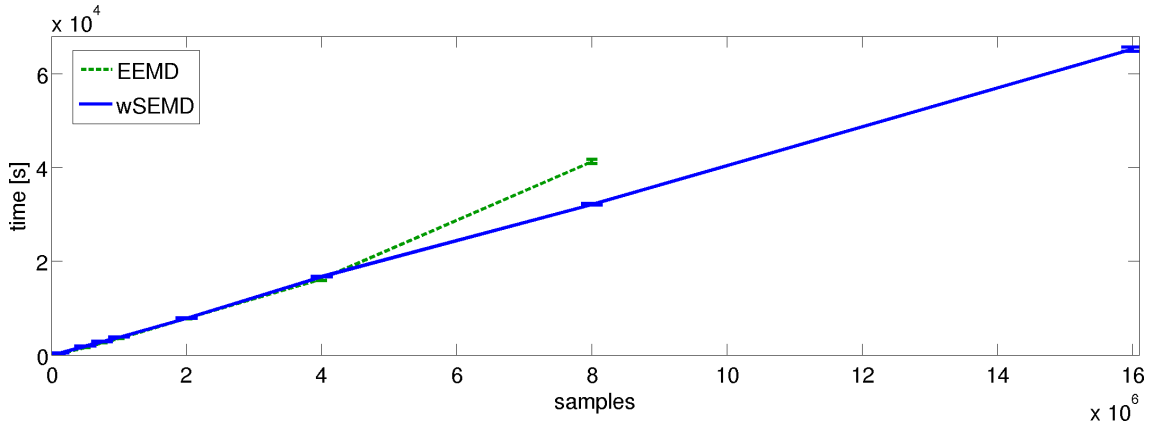

Figure 5.9 An investigation of the computational load of the wSEMD and EEMD decomposition with ensemble size $E = 50$ is depicted with respect to the data length. The error bars mark the standard deviations of the eight single computational loads.

The working memory of the computer (in this case 8 GB) gives a practical limit to the decomposition of long time series. In this test the computations were stopped at a sample size of $8 \cdot 10^6$, respectively, $16 \cdot 10^6$. Nevertheless, some analyses were done using a sample size of $16 \cdot 10^6$ and also the EMD and the EEMD decompositions for ensemble number 1 were run eight times.
The decomposition with EEMD using an ensemble of 50 was not possible to operate at all with the given computer setting. The SEMD and wSEMD decompositions worked perfectly fine, also for $E = 50$ without any problem. Therefore, one can say, that the limits of the *non-online* versions of the algorithm are reached with the used type of machine for that amount of data points.
$16 \cdot 10^6$ samples correspond to approximately 4.4 h of neuromonitoring data (taking the sampling rate of 1 kHz into account) which will be analyzed in chapter 7. As those time series are recorded over days and weeks only (w)SEMD can be applied to those.

Additionally, when compared to EMD, with SEMD and wSEMD it is easily possible to apply parallel computing for every single window, which renders the decomposition much faster and constitutes another advantage of the method.

Chapter 6

Application of wSEMD to Homeostatic Brain Status Data

In the following, brain status data, namely Arterial Blood Pressure (ABP), Intracranial Pressure (ICP) and Tissue Partial Oxygen pressure (TPO) recorded with a sampling rate of 0.2 Hz at the University Hospital Regensburg, will be analyzed. With the aid of a mathematical model [8, 9] it can be shown that correlations of the homeostatic, low-frequency part of ABP, ICP and TPO will occur, if particular cerebral regulatory systems start to fail. Especially a negative correlation between ABP and ICP develops in case of a diminished cerebral compliance, caused by a severe brain swelling, in combination with an intact autoregulation. Such an expanding lesion may severely disturb the cerebral perfusion and therefore has to be detected as early as possible. Up to now this can only be done reliably by repetitive CT-scans, a very stressful procedure for the patient.

Therefore, we used the property of wSEMD, described thoroughly in section 4.2 and [59, 63, 64], that its residuum consists of the low-frequency modes, to extract the latter. In a second step, we will locate temporal interdependencies between the filtered ABP, ICP and TPO data by means of correlation. An interdependency will be constituted only, if all three combinations of the time series (ABP-ICP, ABP-TPO and ICP-TPO) are significantly correlated. In this thesis correlation always denotes the Pearson correlation [65]. For the algorithm the built-in Matlab function *corr* with its default parameters is used.

As the time series have to be filtered by wSEMD first, some investigations concerning the adequate window size are done and the numerical accuracy of wSEMD applied to the homeostatic brain status data is researched. Furthermore, a significance test is employed, in order to receive an appropriate limit for the correlation

coefficient with respect to the various used parameters. In the end, the detected correlations are compared to previous work by Faltermeier *et al.* [10]. This recently proposed method based on Fast Fourier Transform dependably detects such correlations, but has a crucial drawback, as it needs more than 2.8 hours of observation time for the detection. Therefore, the highest possible temporal resolution using the new approach is determined. Another advantage of the correlation based evaluation method is, that it automatically distinguishes between a positive and negative correlation. Finally, an example of an observed interdependency within the neuromonitoring data is presented.

6.1 Data Set

The ABP, ICP and TPO time series are recorded with a sampling rate of 0.2 Hz (see figure 6.1) in the intensive care unit of the Department of Neurosurgery of the University Hospital Regensburg during the treatment of patients with severe brain trauma. With those measurements, globally called neuromonitoring, patients with a critical brain status are monitored. The time series consist of the so-called Mayer waves, and of low-frequency, often nonstationary, nonlinear oscillations attributed to the homeostasis.

A specific set of patients' data is selected for the following analyses, labeled PAT 1, PAT 3, PAT 4, PAT 5, PAT 7 and PAT 8 (PAT 2 and PAT 6 are omitted due to sensor failures). Those data sets exhibit various interesting patients' conditions and different developments of the situation of the patients. In [10] these time series have already been investigated. The data is, therefore, well-known and has been compared to further medical diagnosis of the patients, as for example neuro-imaging.

The time series exhibit failures of the sensors, e.g. when they are cleaned or the patients are relocated. Those intervals of the time series, which often show extreme values, are removed and replaced by linear splines preliminary. As the EMD decomposition has problems dealing with linear segments of the data, which do not feature any extrema, noise is added to the time series to avoid those difficulties. As only the residua are of interest for this specific application, additional high-frequency IMFs created by the noise are insignificant.

In the following $n = 1, 2, \ldots, N$ denotes the samples of the data, which yields, with a time interval of $\Delta t_n = 5$ s between the samples, the temporal scale $t_n = n \cdot \Delta t_n$.

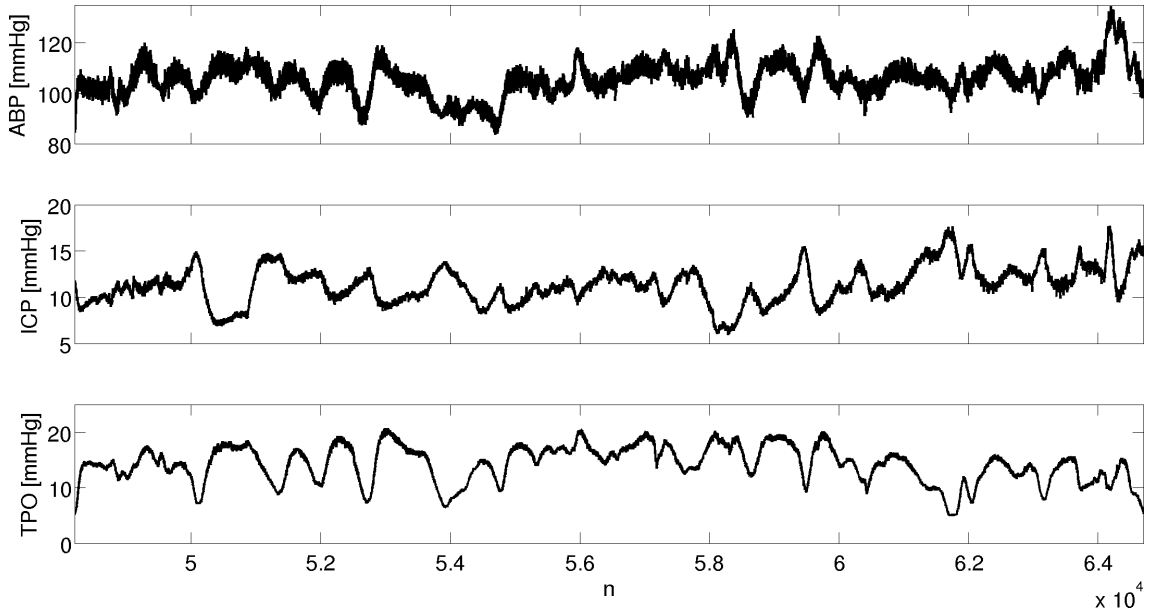

Figure 6.1 A detail of an arterial blood pressure (top), intracranial pressure (middle) and tissue partial oxygen pressure (bottom) time series (PAT 3). It was recorded in the intensive care unit of the Department of Neurosurgery of the University Hospital Regensburg measured in the pressure unit [mmHg]. The abscissa depicts the sample points n with an interval of $\Delta t = 5$ s between the samples, so that the temporal scale corresponds to $t_n = \Delta t \cdot n$.

6.2 Multi-Taper Method

In order to detect interdependencies within the neuromonitoring time series up to now the windowed multi-taper method has been used, which is based on the coherence of the data in the frequency domain (for a more detailed description see [66]).

The method works with a fixed segment size, which was chosen to 2048 sample points in this case. Starting with the beginning of the time series, isochronic segments are cut out of the data, e.g. the ABP and ICP. Then they are normalized by subtracting their mean and dividing by their standard deviation. Following that the power spectrum of each normalized window is computed together with the coherence between them. The multi-taper algorithm applies a significance test to the frequency distributions comparing it to white noise with a significance level of 99 %. From medical literature [66] it is known that the frequency range $\nu < 0.002$ Hz contains the relevant information for the correlational analyses. Therefore, within that range the number of emerging frequencies, that are significant in both spectra and the coherence calculation, are counted. The level of correlation is defined as follows:

the number of significant frequencies within the coherence divided by the number of all significant frequencies occurring in the segments. This approach is applied repeatedly in segments shifted by a certain step size (in this case a step size of 1 is applied) along the time axis, until the end of the time series is reached. A significance test, similar to the one described in section 6.5, will determine, if the level of interdependency between two isochronic segments of the time series is significant.
To obtain information about the phase difference between two correlated signal intervals, the Hilbert phases of the low-pass filtered and normalized time series can be calculated, additionally, with respect to a significance test.

6.3 Completeness and Numerical Accuracy

First of all, the numerical accuracy of the decomposition will be checked in order to verify, if the decomposition produces reasonable results. Thus, the sum of all IMFs and the residuum is compared to the original data via an estimate of the mean squared error (MSE). Exemplarily PAT 3 is used. The decomposition is applied using the step sizes $K = 1, 2, 5$ and 10 and the window sizes $M = 20, 30, \ldots, 100$. For all possible combinations of step and window size, very similar errors of a magnitude of 10^{-27} are obtained (see figure 6.2). This is to be compared with the MSE of the decomposition with plain EMD, which amounts to 10^{-27} as well. These numbers are far below the precision of the measurements ($\pm 10\,\%$). They originate from numerical errors, so that the decomposition can be regarded accurate aside from those numerical inaccuracies. The basic requirement for the decomposition, thus, is fulfilled by wSEMD.

6.4 Selecting the Window Size

As known from the medical literature [66], one important frequency sub-band ν of brain status data, namely ABP, ICP and TPO, lies roughly in the interval between 0 Hz $\leq \nu \leq$ 0.002 Hz. Hence, the data has to be decomposed accordingly by choosing an appropriate window size parameter, so that only the required modes remain in the residuum after the decomposition. Since in section 5.5 and in [59] a thorough analysis regarding the impact of the window size on the frequencies contained in the resulting global residuum have been discussed already, it is clear that the desired window size has to correspond to $M = 50$ roughly, taking the sampling rate of 0.2 Hz into account. Therefore, wSEMD decompositions with window sizes

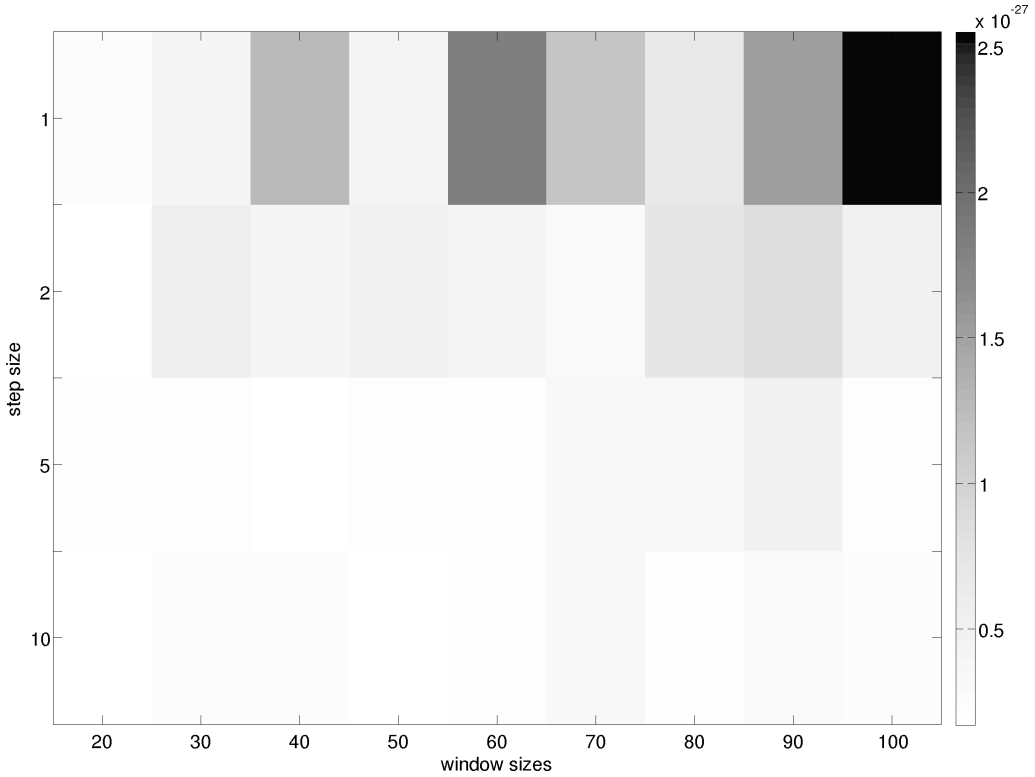

Figure 6.2 Mean squared error between the original time series and the sum of all IMFs and the residuum of wSEMD for step size $K = 1, 2, 5, 10$ and different window sizes $M = 20, \ldots, 100$.

$M = 10, 20, \ldots, 100$ are examined in order to identify the optimal size parameter yielding the desired results.

6.4.1 Mean Reconstruction Error between Residuum and Original Data

As the first criterion for the choice of the wSEMD window, it is determined which residuum meets the center of the original data best, by calculating the mean error (ME) between the original time series $x(t_n)$ and the residua $r_M(t_n)$ of all wSEMD decompositions with window sizes $M = 20, \ldots, 100$ of PAT 3:

$$ME = \frac{1}{N} \sum_{n=1}^{N} \big(x(t_n) - r_M(t_n) \big) \tag{6.1}$$

with N denoting the sample size. Since most estimates are obtained with step size $K = 1$, this parameter is used from now on for the decomposition, if not

stated otherwise. The absolute values of the mean error are depicted in figure 6.3. The mean error hereby means the sample-wise difference between both time series normalized by the sample size of the complete data set. The average ME for window sizes $M = 20, \ldots, 100$ amounts to 0.055. For $M = 40, 50, 60$ the ME is smallest, therefore one can say, that those residua cover the oscillations of the original data best. However, their deviations from the mean ME value are small and thus further analyses will be performed in the following.

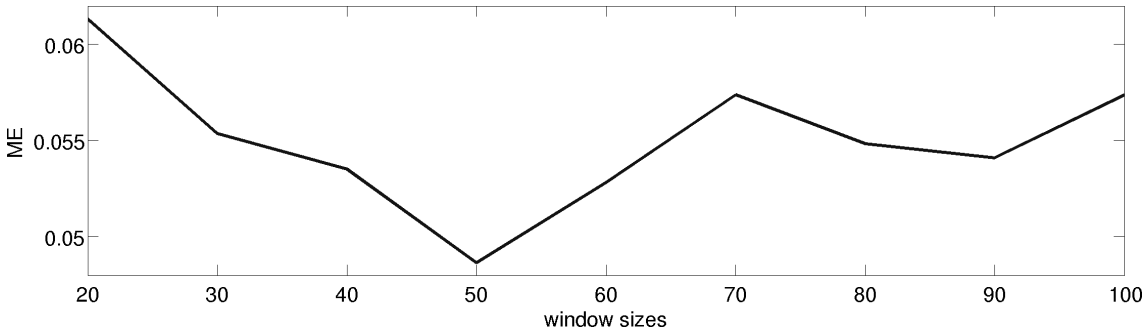

Figure 6.3 Mean error between the original time series and the residua of wSEMD for step size $K = 1$ and different window sizes $M = 20, \ldots, 100$.

6.4.2 Toy Data Experiment

An analysis with toy data is additionally performed to simulate the problem. Therefore, 2048 different sine functions are generated using frequencies in the range of 0.00005 Hz $\leq \nu \leq$ 0.1024 Hz ($\Delta\nu$ = 0.00005 Hz), with 0.1 Hz being the highest frequency that can be represented by data with a sampling rate of 0.2 Hz. All sine waves have randomly distributed phases $(0, \ldots, 2\pi)$ and amplitudes with exponentially decreasing values beginning with the lower frequencies, similar to the neuromonitoring data. They are summed up and decomposed with wSEMD using different window sizes $M = 10, \ldots, 100$. Afterwards, the filtered data are analyzed with the same methods as used in [66] to detect the sub-bands, which contain information. In short, windowed multi-taper spectral analysis (MTM) in combination with a significance test is used to determine the percentage how often a specific frequency is detected as significant within a very long time series. A more detailed description of MTM is found in section 6.2.

Figure 6.4 shows these statistics for the selected window sizes. For clarity only window sizes $M = 10, \ldots, 70$ are depicted. It can be seen that all window sizes beginning with $M = 10$ up to $M = 50$ contain a large amount of frequencies

higher than the desired 0.002 Hz. For window sizes $M = 60, \ldots, 80$ the distribution decreases rapidly to zero shortly after the limit of 0.002 Hz and for $M = 90, 100$ the frequencies lower than 0.002 Hz are already compromised. Because of the frequency content in the residuum resulting from the window sizes, the latter seems optimal in the range $M = 60, \ldots, 80$.

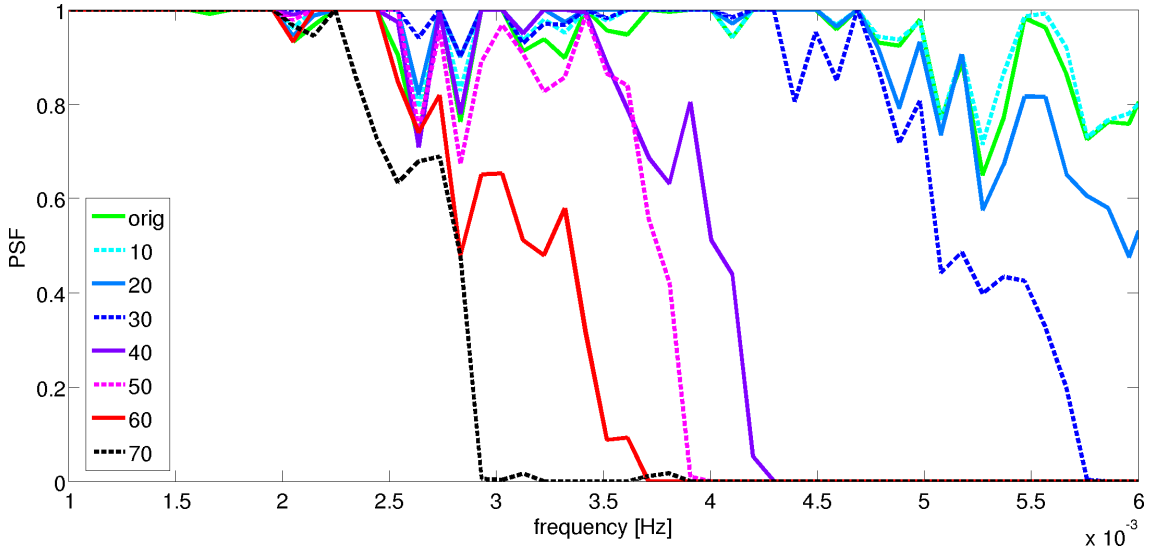

Figure 6.4 The residua of wSEMD with different window sizes $M = 10, \ldots, 70$ of the toy data set and the original data analyzed by windowed multi-taper spectral analysis in combination with a significance test. The percentage of being significant for every single frequency (PSF) is shown with respect to the frequency in Hz.

6.4.3 Medical Data

For further investigation to determine, which window size to use, the above mentioned spectral tool multi-taper method (MTM) (see section 6.2 for details) is used to analyze the different wSEMD residua of the ABP of PAT 3 (see figure 6.5) including the distribution gained from the unfiltered data. For clarity only window sizes $M = 20, \ldots, 90$ are illustrated.

For $M = 70, 80, 90, 100$ – in contrast to the smaller window sizes – too much power is removed from the distribution by wSEMD in the frequency range of $1 \cdot 10^{-3}$ Hz $\leq \nu \leq 2 \cdot 10^{-3}$ Hz. However, the residua of window sizes $M = 20, \ldots, 60$ still contain a sufficiently high amount of power. Therefore, it is clear that the window sizes $M = 20, \ldots, 60$ are to be preferred for the decomposition with wSEMD. Additionally, it can be seen that the strength of the low frequencies is slightly in-

creased by an appropriate wSEMD filtering, most likely due to an effective noise reduction.

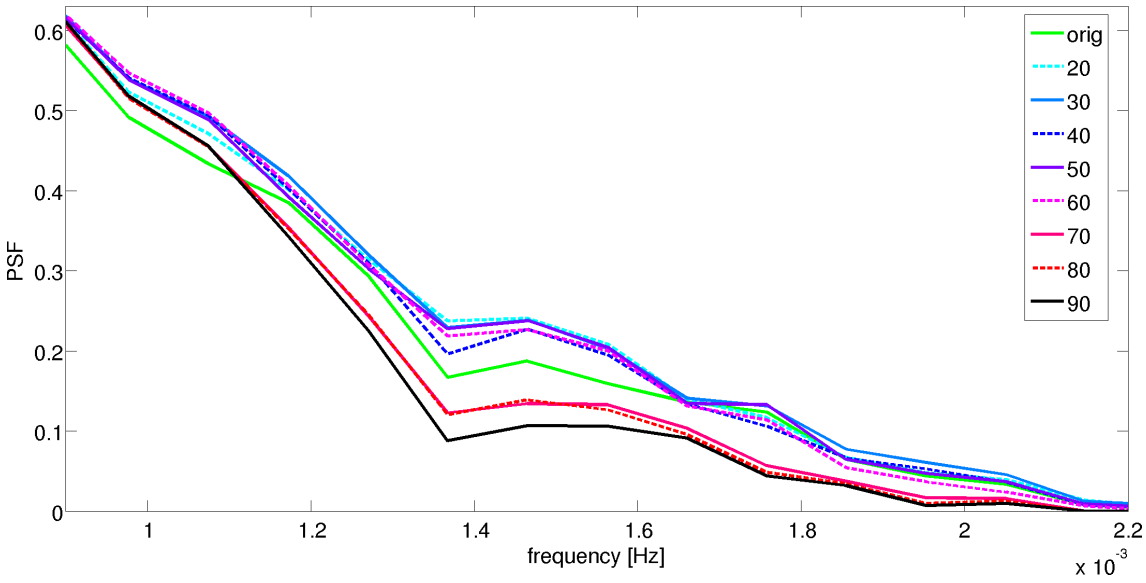

Figure 6.5 The residua of the wSEMD decomposition with different window sizes of the ABP time series analyzed by a windowed multi-taper spectral analysis together with a significance test. The ordinate shows the percentage of significant frequencies (PSF) and the abscissa the frequency in Hz.

Taking all examinations into account the spectra of the residua obtained by wSEMD with window sizes $M = 10, \ldots, 50$ contain too many high frequencies and in those of the residua of $M = 70, \ldots, 100$ too much power in the desired frequency range is removed. The residua of windows $M = 40, 50, 60$ meet the center of the original data best. Therefore, in the following analyses of the correlations the residuum with window size $M = 60$ will be used.

6.5 Significance Test for Correlation Coefficients

To estimate the average random correlation of non-isochronic segments of the wSEMD filtered ABP, ICP and TPO time series, a statistical test is done with respect to the segment size and the significance level.

The significance test is based on the mathematical model [8, 9] which predicts, that the interdependencies within the neuromonitoring data appear without time delay, thus isochronously in case of a failure of particular cerebral regulatory systems. Due to that prediction, correlations will not, or rather only randomly, appear between

two segments of the different time series, if their starting points are shifted relative to each other. The time shift between the segments will have to be selected adequately, taking into account, that the signals themselves could exhibit autocorrelation effects. The minimal shift between the segments has to be larger than the autocorrelation effects.

Mean Windowed Autocorrelation

The extent of the autocorrelation effects within the signals will be calculated by means of the mean windowed autocorrelation in the following way: An ABP signal consisting of the residua of all patients' time series, decomposed with wSEMD ($M = 60$, $K = 1$) is used as input data for the test. The analysis is conducted comparing two segments of the time series, respectively. Randomly a starting point of a first segment is chosen within the time series. The starting point of the second window is selected to be the same as the first starting point plus a delay d. Then the mean windowed autocorrelation C_A between both windows is examined.
In general, the correlation in this thesis, denoted with C, means the Pearson correlation and is calculated according to [65]:

$$C(x, y) = \frac{cov(x, y)}{\sigma(x)\sigma(y)} \tag{6.2}$$

whereby x and y denote the two data sets, which are supposed to be compared, $cov(x, y)$ means the covariance of x and y and $\sigma(x)$ the standard deviation of x.
The mean windowed autocorrelation is calculated, averaging over Z trials with Z different random starting points of the windows:

$$C_A(d) = \frac{1}{Z} \sum_{z=1}^{Z} C(l_z, l_z + d) \tag{6.3}$$

whereas l_z and $l_z + d$ denote the two windows to be compared. In this case the parameter is set to $Z = 200\,000$. The analysis is conducted with respect to different delay parameters d. That way an autocorrelation curve with respect to the delay is obtained. It decreases from $C_A(0) = 1$ to a fluctuation around $C_A(d) \approx 0$, for approximately $d \geq 1000$ choosing the window size $L = 2048$. The same results were obtained with the ICP and TPO time series.
Also the impact of the window size is analyzed. It influences the results of the mean windowed autocorrelation only marginally. To be sure the minimal delay for the significance test will be set to $d = 5000$.

Mean Windowed Significance Test

For the mean windowed significance test $Z = 200\,000$ non-overlapping, i.e. non-isochronic segments with an interval of at least $d = 5000$ samples between them – due to the autocorrelation – are picked out of all three time series ABP, ICP and TPO, respectively. Their starting points are chosen randomly in all of the Z trials. Then the correlation coefficients C between all combinations of the three segments are calculated. For different correlation limits ($C_{\text{lim}} = 0.01, \ldots, 1$) the percentage of coefficients showing a higher correlation than that limit is determined. Only if all three combinations of neuromonitoring data windows (ABP-ICP, ABP-TPO and ICP-TPO) exhibit a larger coefficient C than the correlation limit, this case will be counted as correlated. However, since non-isochronic segments are expected not to be correlated, an error rate is established counting the wrong hits. The error rate $F(C_{\text{lim}})$ is assessed for various correlation limits C_{lim}:

$$F(C_{\text{lim}}) = \frac{1}{Z} \sum_{z=1}^{Z} f_{C_{\text{lim}}}(l_z, l_{z'}) \tag{6.4}$$

with

$$f_{C_{\text{lim}}}(l_z, l_{z'}) = \begin{cases} 1 & \text{if} \quad C(l_z, l_{z'}) > C_{\text{lim}} \\ 0 & \text{otherwise} \end{cases} \tag{6.5}$$

whereby l_z and $l_{z'}$ indicate the two windows to be compared. This test can be conducted with different segment sizes L.
Furthermore, a significance level is set. It represents, that for each correlation limit only a certain percentage of the segments is allowed to exceed this limit. This means, that only a specific number of wrong hits are tolerated. Thus, the minimal acceptable correlation limit for the chosen significance level can be determined.
In the following the significance test for the correlation coefficients is conducted, first with varying segment sizes and afterwards with respect to various significance levels.

6.5.1 Variation of the Segment Size

First of all the residua of the wSEMD decomposition with window size $M = 60$ and step size $K = 1$ of the ABP, ICP and TPO time series of the six patients' data (PAT 1, 3, 4, 5, 7, 8) are calculated. A test data set is generated adding all patients' residua of the ABP, ICP and TPO data, respectively, subsequently combined to one time series. The significance test is done with segment sizes of $L = 100, \ldots, 2048$ and

in this case a significance level of 10 % is applied, meaning that only 10 % wrong hits are accepted. Taking this significance level into account, a certain correlation limit is computed for each segment size. Correlation coefficients of isochronic segments of the data higher than that correlation limit are estimated to exhibit a significant correlation.
Figure 6.6 shows the correlation limits of the whole data set consisting of the six patients' time series put subsequently into one time series for varying segment sizes. The correlation limit decreases for increasing segment sizes, meaning that considering larger data intervals less wrong hits are found. For a segment size of e.g. $L = 720$, which matches 1 hour of data, the correlation limit amounts to 0.5 for the whole data set (with a significance level of 10 %). That means, that the correlation coefficient has to be higher than 0.5 to account for a significant correlation between ABP, ICP and TPO, which seems reasonable.

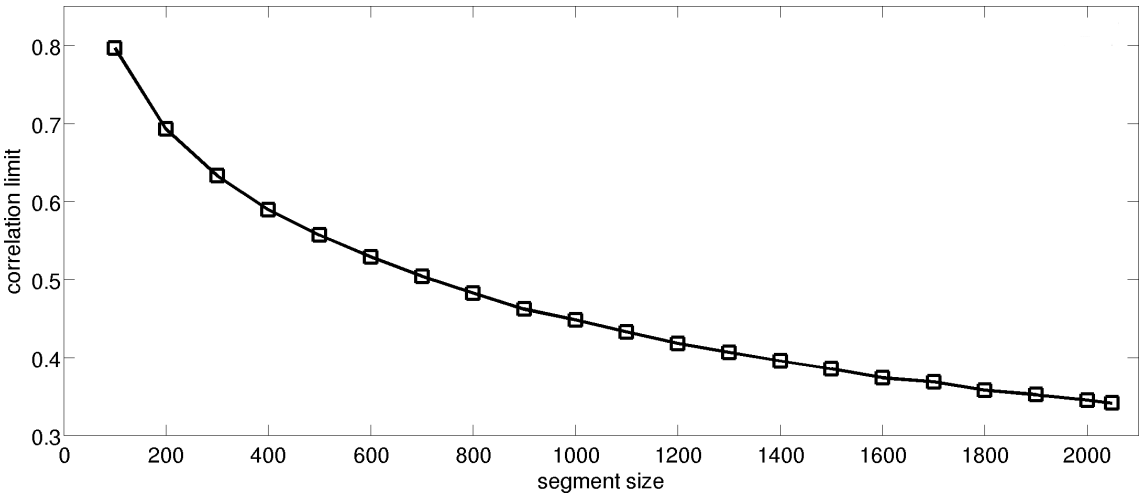

Figure 6.6 Correlation limits for different segment sizes with a fixed significance level of 10 % for the whole data set consisting of a combination of all patients' data sets.

In the following the influence of the significance limit on the correlation limit with respect to a fixed segment size will be examined.

6.5.2 Variation of the Significance Limit

For further investigations, again, the data set with all patients' brain status data will be used, consisting of the residua of the ABP, ICP and TPO time series. They were decomposed with wSEMD utilizing a window size of $M = 60$ and a step size of $K = 1$. The significance limit will be varied and the segment size will be kept

constant to $L = 2048$. Such an interval of the time series corresponds to roughly 2.8 h of the data, taking the sampling rate of 0.2 Hz into account. The significance level is varied from 0.005 to 0.1, respectively, from 0.5 % to 10 %.
Figure 6.7 shows the correlation limit for increasing significance level. The correlation limit ranges from around 0.35 to 0.65. It increases for decreasing significance levels, as expected.

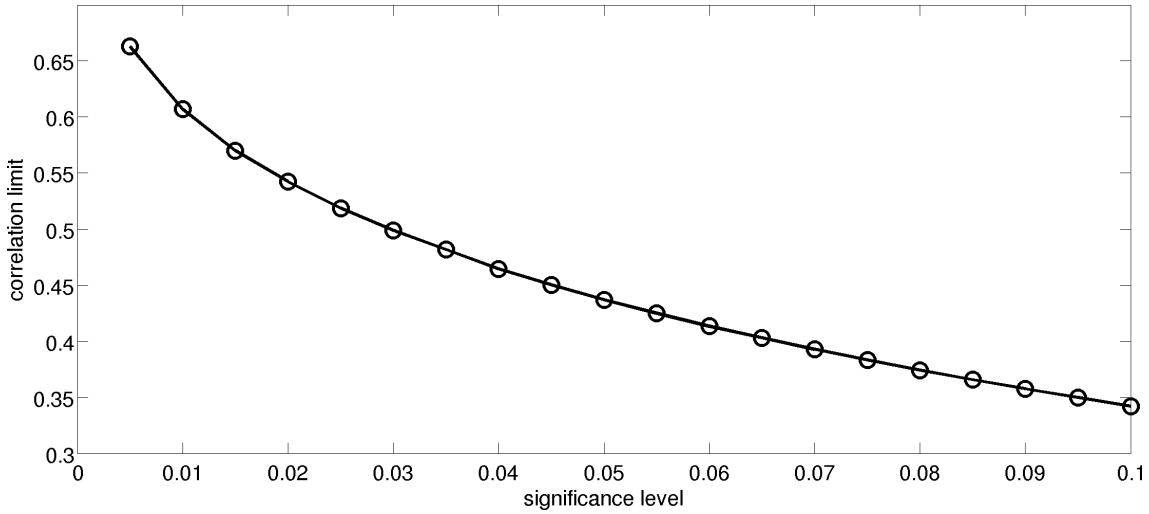

Figure 6.7 Correlation limits for various significance levels and for a fixed segment size of $L = 2048$ which corresponds to ca. 2.8 h of the data.

A significance level of 5 % seems to be a reasonable choice and constitutes an often used standard value in statistics and is, therefore, applied in the following analyses. The correlation limits are calculated accordingly for all segment sizes, taking the 5 % significance level into account.

6.6 Analyzing Neuromonitoring Time Series

In this section the correlation analyses between the neuromonitoring time series are applied. The analyses are conducted in the following way: A segment of a certain segment size L is taken from the ABP time series and the same, isochronic segment is equally cut out of the ICP and TPO data. The correlation between ABP-ICP, ABP-TPO and ICP-TPO is calculated and the segments will be regarded correlated if all three correlation coefficients exceed the previously calculated correlation limit. Afterwards, the next segments are picked out shifted by 1 data point, i.e. the overlap to the last segment amounts to $L - 1$ samples. Again the correlation between the

three time series is calculated and checked for significance. This procedure is applied until the end of the data is reached, yielding one sample per segment denoting correlation between ABP, ICP and TPO or independence of the time series.
Following that, a comparison of the correlational analysis method to the previous work with MTM (see section 6.2 for details) is drawn, using the same segment size, namely $L = 2048$, for the analyses. Additionally, the consensus between the investigations in the frequency and time domain is examined. Furthermore, testing the stability of the results with decreasing the segment size, the optimal temporal resolution is detected. The minimal segment size will be determined for a stable and reliable localization of correlations as close to real-time analysis as possible. Finally results within the neuromonitoring data sets exhibiting interdependencies, respectively, no interdependencies are presented.

6.6.1 Comparison to MTM Analyses

Correlation analyses have already been executed with this data set using the windowed multi-taper spectral analysis method (MTM) [10] (for a short description of the method see section 6.2). The investigations have been conducted in the frequency domain. In order to have a sufficient frequency resolution to examine the time series, an amount of at least 2048 samples is necessary. The temporal resolution needs improvement, which thus cannot be implemented in the frequency domain. Therefore, the correlation analyses are implemented with residua in the time domain in this thesis. First of all a comparison between both methods – the correlation evaluation and the MTM – is performed. To be able to do the comparison between MTM in the frequency and the correlation in the time domain precisely, for the correlation analyses also a segment size of $L = 2048$ is utilized at first.
In figure 6.8 the comparison between both analyses are shown exemplarily. PAT 3 is used as an example to show the interdependent segments found with MTM and with the correlation with respect to time. Every marker denotes a time segment of 2048 samples in which ABP, ICP and TPO are significantly correlated. The significance level is set to 5 %.
The correlation method detects a little more interdependent signals especially at the beginning of the time series. However, both methods are very well in accord. That both methods locate the interdependencies between the ABP, ICP and TPO time series slightly shifted is expected, since the MTM, respectively, the Fourier transform needs a full period of every frequency within the signal to detect it. It is therefore possible, that the correlation method discovers an interdependency, while

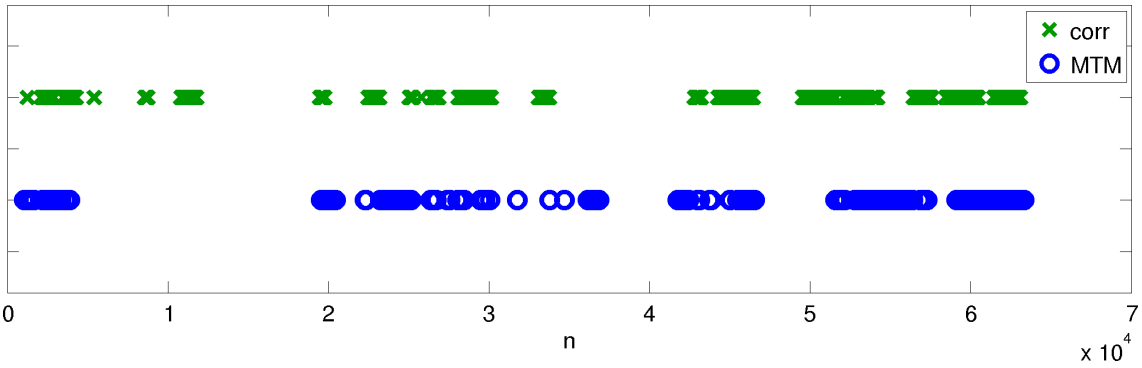

Figure 6.8 Correlated segments of PAT 3 found by MTM and correlation with segment size $L = 2048$. The abscissa denotes samples n of the time series with a sampling interval of $\Delta t = 5$ s. The temporal scale corresponds to $t_n = \Delta t \cdot n$.

MTM still needs further samples to complete a full period and discover the frequency exhibiting interdependencies between the time series. Moreover, MTM is expected to estimate the interdependencies quite conservatively due to its significance test, which is applied first.

On the other hand, for the correlation method as well as for the MTM, it is likely to happen, that interdependencies are located slightly delayed in time. Since it can take some time until the interdependent part of the time series takes up the majority of the considered segment, the other part of the time series still dominates the resulting correlation measurement for a specific amount of time. Evaluating the results, this has to be taken into account. This is true for all windowing methods. Nevertheless, this situation can be moderated by applying smaller segment sizes, which will be conducted in section 6.6.2.

Figure 6.9 quantitatively illustrates the consensus, respectively, the dissent, of the two different research methods, MTM and correlation, for all analyzed patients. For all data sets the percentage of cases, in which both methods agree, is counted. If they do not coincide, the plot shows, which one sees an interdependency and which one does not. The top line shows the percentage of segments, for which in general consensus between MTM and the correlation method is measured. The other two graphs denote the cases, in which MTM sees a similarity between both time series and the correlation does not (MTM 1, corr 0) and the other way around (MTM 0, corr 1). All three graphs add up to 1 for every patient.

As observed in the example of PAT 3 the MTM estimation of correlated segments is a little more conservative in contrast to the correlation. Especially interesting is, that the correlation method recognizes almost all cases, in which the MTM registers interdependencies as well. Most of the dissents originate from additionally located

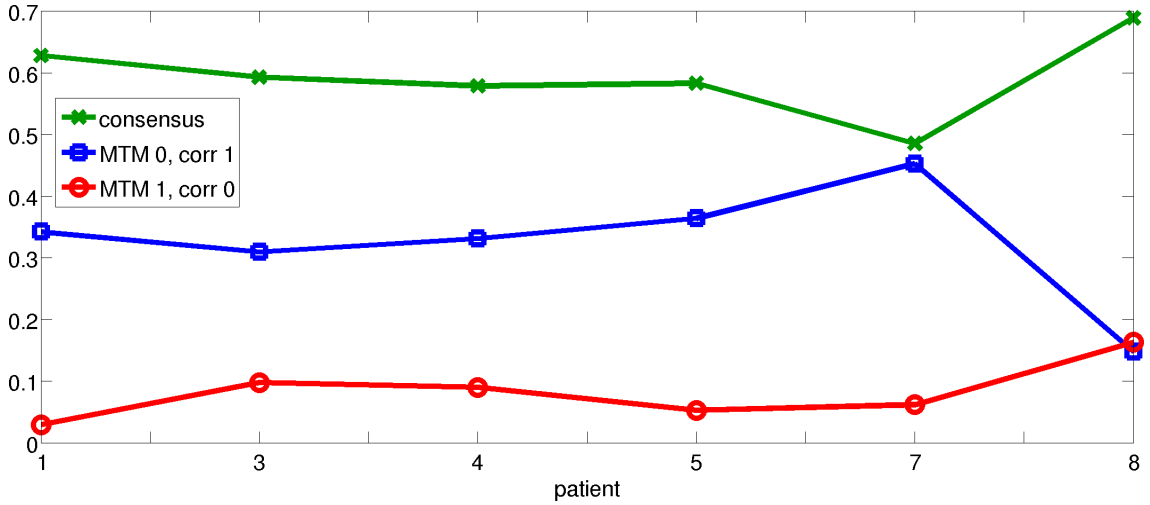

Figure 6.9 Consensus between the MTM and correlation, which is additionally differentiated by the cases with MTM showing interdependencies in contrast to the correlation (MTM 1, corr 0) and vice versa (MTM 0, corr 1).

interdependencies by the correlation method, which will be regarded in detail later on.

However, this plot has to be considered carefully. One has to keep in mind, that the time series of located correlations resulting from both methods are compared pointwise. Should the detected interdependency be shifted by only one sample, this situation will be counted as dissent. Furthermore, the graph depends on the employed significance level of the correlation method and the MTM, which is challenging to chose equivalently for both approaches.

As a first example, the significantly correlated period at the beginning of the data set PAT 3 (see figure 6.8 at around $n = 11\,000$) is considered, since in this interval of the time series the correlation and the MTM disagree. As the absolute pressure values of the brain status data differ vastly, an optical evaluation is not easy with the raw data. A normalization of the illustrated interval of the ABP, ICP and TPO data is implemented first. The normalization is performed thus:

$$f_{\text{norm}}(t_n) = \frac{f(t_n) - \overline{f}(t_n)}{\sigma} \tag{6.6}$$

with $f_{\text{norm}}(t_n)$ denoting the normalized time series, $f(t_n)$ the raw data, $\overline{f}(t_n)$ its mean value and σ its standard deviation.

Figure 6.10 presents the detail, namely samples $n = 10\,000, \ldots, 12\,000$, of the residua of the ABP, ICP and TPO of PAT 3 decomposed with wSEMD using the window size $M = 60$ and the step size $K = 1$. This segment is found correlated, which, by optical

inspection, can be confirmed. The significant positive correlation between ABP-TPO, especially, and the high negative correlation between ABP-ICP, respectively, TPO-ICP is apparent. This particular interdependent signal interval was not located by MTM.

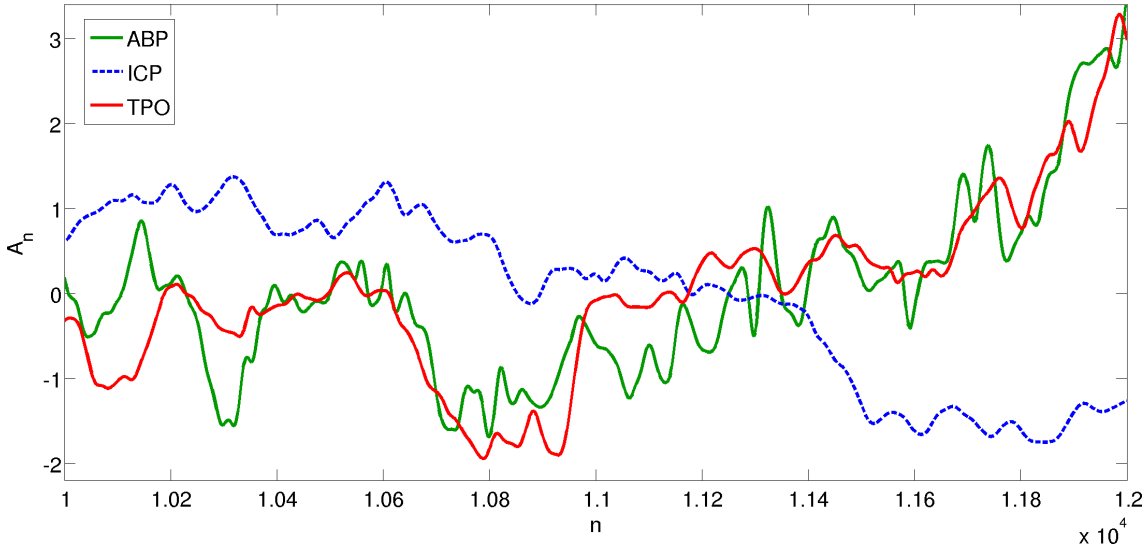

Figure 6.10 A detail of the normalized ABP, ICP and TPO time series is presented featuring interdependencies, which are detected by the correlation, but not by MTM. The ordinate depicts the normed amplitude A_n and the abscissa the samples $n = 10\,000, \ldots, 12\,000$ of the data.

Therefore, it can be concluded, that the correlation method detects slightly more interdependencies than MTM, however this can only be attributed to the conservative estimation of the multi-taper method. Another advantage of using the correlation is, that a positive and negative correlation are automatically distinguished. Additionally computing the Hilbert phase difference, which is necessary after MTM, is not required any more. The approach to locate the interdependencies in the time domain by means of Pearson correlation can be considered reliable and thorough.

6.6.2 Analysis of the Segment Size

For the practical application of the presented method in an intensive care unit, it would be optimal to be able to apply it as a real-time technique. Therefore, it would be desirable to receive the results with a temporal resolution, which is as high as possible. Further, a smaller segment size alleviates the effect to find correlations slightly time delayed due to the windowed approach. To find the corresponding minimal segment size the influence of that parameter on the results is, thus, examined.

The findings should, of course, be independent of the segment size.
The basis for the following examinations are the residua of ABP, ICP and TPO obtained by wSEMD with window size $M = 60$ and step size $K = 1$ again. The analyses are shown for PAT 3 exemplarily. The findings behave similarly for all data sets though. Figure 6.11 depicts markers when a correlation between segments of all three neuromonitoring time series ABP, ICP and TPO of PAT 3 occurs. The horizontal lines of markers are shown with respect to time and every line stands for the use of a different segment size L for the analyses. A marker respectively correlation will only be illustrated, if the correlation limit is exceeded in the specific time interval. Like in the previous analyses the initial significance level again amounts to 5 %.

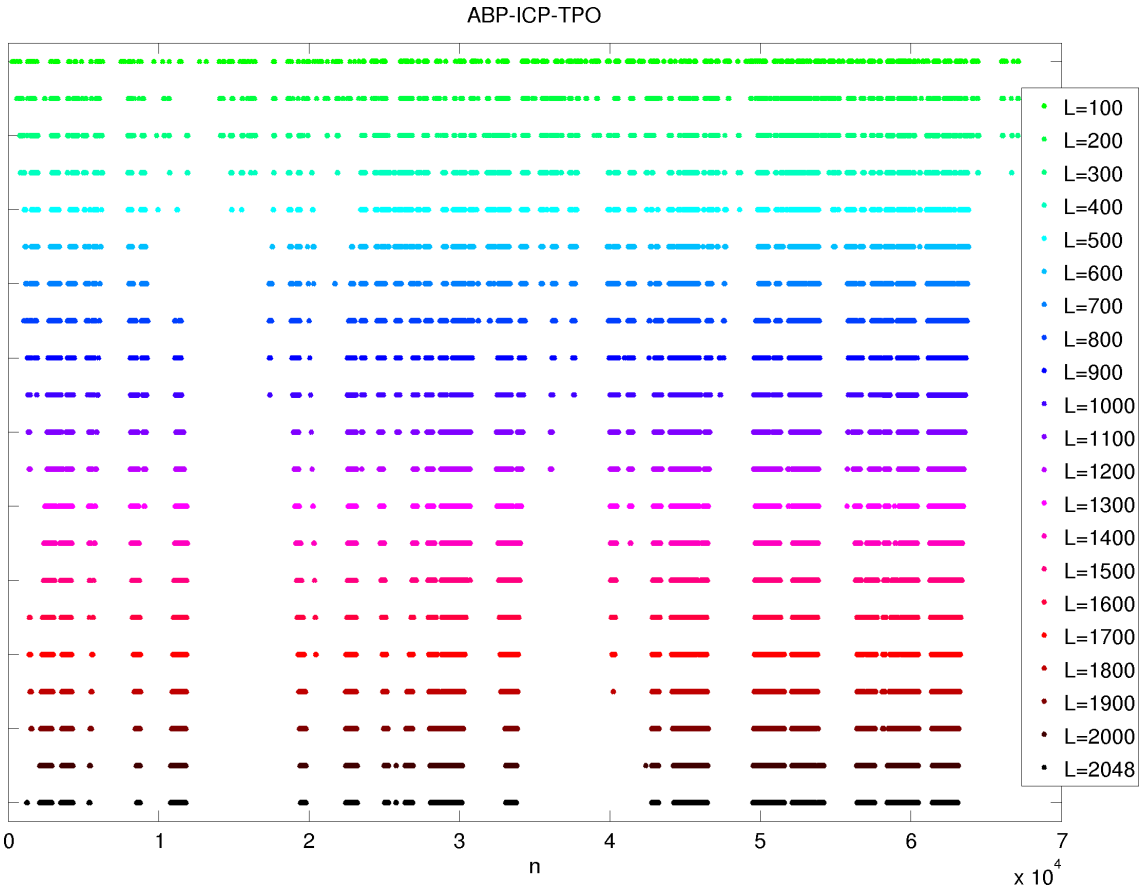

Figure 6.11 Denoted with markers are segments with significant correlation between the ABP, ICP and TPO time series of PAT 3. The analyses are conducted depending on the segment size L. The abscissa shows the samples of the time series n with a sampling interval of $\Delta t = 5$ s. The temporal scale corresponds to $t_n = \Delta t \cdot n$.

The localized correlations stay very stable for most of the tested segment sizes. However, three different sectors can be spotted. One in the range of approxi-

mately $1500 \leq L \leq 2048$, the next roughly in $700 \leq L \leq 1400$ and finally circa $100 \leq L \leq 600$. In the middle range the correlated segments seem to subdivide slightly. Beginning with ca. $L = 600$ (and lower) the found interdependencies start to transform strongly. A higher number of correlation markers appear which are spread over the time series more and more and are no longer clustered for decreasing segment sizes. Thus, a segment size of $L = 720$, which corresponds to 1 h of data, taking the sampling rate of 0.2 Hz into account, seems to be a reasonable choice for the parameter. The located interdependencies remain mostly identical to those found for higher segment sizes and equally $L = 720$ seems the best achievable resolution. Hence, in the following the segment size parameter $L = 720$ will be applied.

6.6.3 Correlations in Neuromonitoring Data

After an appropriate significance level (5 %) and segment size ($L = 720$, respectively, 1 h of data) have been chosen, the correlation analyses can finally be conducted with a very good temporal resolution. Examples of periods containing interdependencies and no significant correlation in the neuromonitoring data will be presented in the following. The illustrated intervals of the ABP, ICP and TPO time series are normalized before they are depicted as is shown in section 6.6.1 (see equation (6.6)).

No Significant Correlation

First of all an example interval of the brain status data exhibiting no significant correlation is presented in contrast and as a possibility to compare to figure 6.10 and the subsequent figure 6.13 in this section, which show a high correlation. The illustrated data interval features the gap in the correlation time series of figure 6.11 between sample 10 000 and 20 000. Presented in figure 6.12 are the residua filtered with wSEMD ($M = 60$, $K = 1$) of the ABP, ICP and TPO normalized in the particular data segment. The missing sample points at around $n = 16\,800$ of the ICP data mark a sensor failure. Also by optical inspection significant interdependencies of all three data sets are not detectable.

Significant Correlation

Many segments of the data sets with significantly high correlation are detected showing the interdependencies between the ABP, ICP and TPO time series. We selected one particular part – visualized in figure 6.13 – located at the end of the

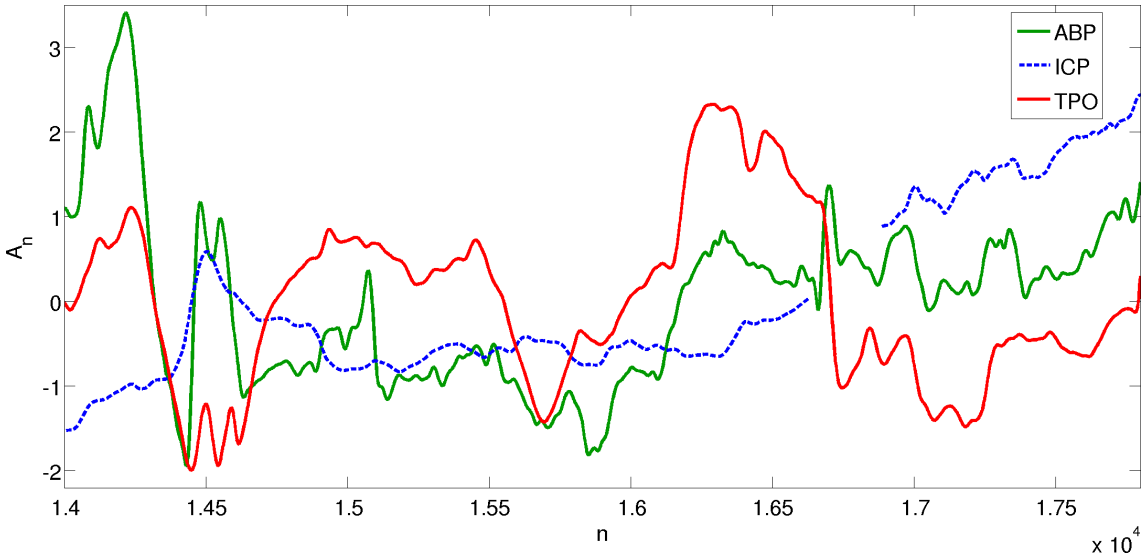

Figure 6.12 A detail of the normalized ABP, ICP and TPO time series is presented featuring no significant interdependencies detectable via the correlation method. The ordinate depicts the normed amplitude A_n and the abscissa the samples $n = 14\,000, \ldots, 17\,800$ of the data. At around $n = 16\,800$ the missing data points of the ICP time series exhibit a sensor failure.

PAT 3 time series (c.f. figure 6.8), that has already been thoroughly discussed in [8, 10]: On the one hand, it has been evaluated with the help of the mathematical model. On the other hand, this particular segment has also been detected as an interval containing a large amount of interdependencies using the multi-taper method. The correlation exhibits high values over a very long time span in this interval, the median correlation of the presented data segment amounts to:

- -0.76 for ABP-ICP
- 0.81 for ABP-TPO
- -0.83 for ICP-TPO

Figure 6.13 again shows the residua decomposed with wSEMD using a window size of $M = 60$ and $K = 1$ of all three time series, the arterial blood pressure, the intracranial pressure and the tissue partial oxygen pressure. The high, negative correlation between ABP-ICP and ICP-TPO and the high positive correlation between ABP-TPO is already eminent only performing a visual examination of the plotted residua.

The Pearson correlation in combination with wSEMD is, thus, able to dependably detect interdependencies in neuromonitoring time series with a time resolution of

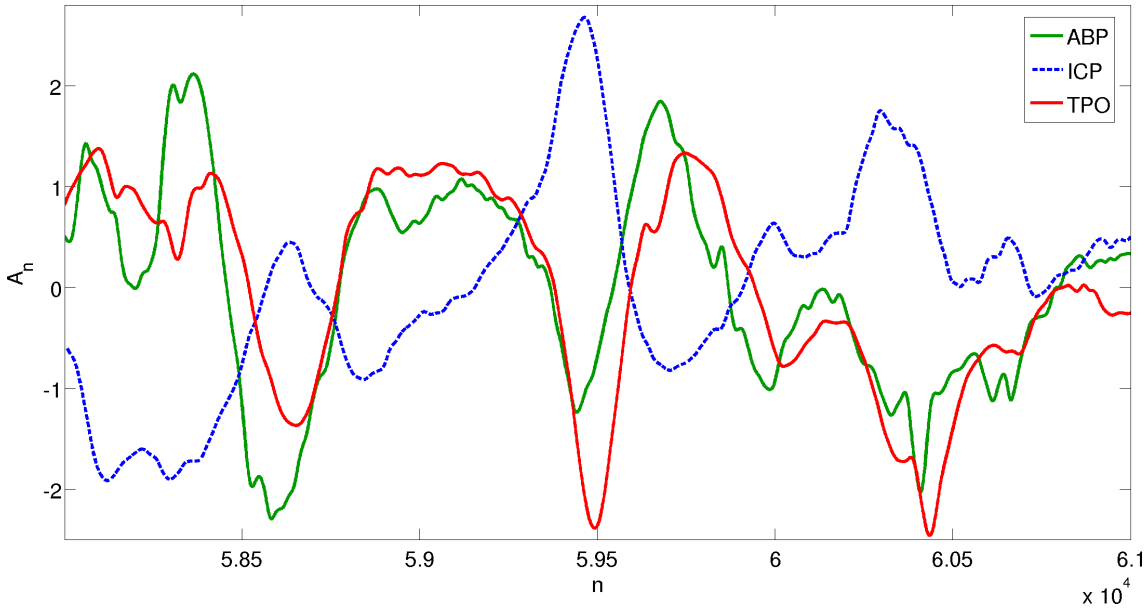

Figure 6.13 A detail of the normalized ABP, ICP and TPO time series of PAT 3 exhibiting a high correlation is illustrated. The ordinate depicts the normed amplitude A_n and the abscissa the samples $n = 58\,000, \ldots, 61\,000$ of the data.

only 1 h. Additionally, more interdependent segments within the brain status data are located than with the MTM approach, since the estimation of the latter is quite conservative. Furthermore, the type of correlation, positive or negative, is automatically determined without the need of an additional analysis of the phase difference. We demonstrated that the presented method reduces the amount of observation time, needed to reliably detect the interdependencies within neuromonitoring data, drastically.

Chapter 7

Application of wSEMD to Pulsatile Brain Status Data

Due to (weighted) Sliding Empirical Mode Decomposition it is possible to apply the EMD technique to very long biomedical time series with high sampling rate. Even real-time analyses can be operated with the new wSEMD method. An example for biomedical time series with a very high sampling rate are neuromonitoring data recorded in the intensive care unit of the Department of Neurosurgery of the University Hospital Regensburg. With a sampling rate of 1 kHz and a duration of the measurements of days and weeks those amounts of data points are hard to handle.

In order to learn more about the brain during a traumatic brain injury, it would be especially interesting to detect differences between the behavior of the ABP – as the input signal – and the ICP. Deviations between the ABP and the ICP might indicate a change of the state of the brain, which might be caused by a modification of the condition of the patient. In contrast to the slow variations, examined in chapter 6, now the focus will lie on fast oscillating, nonlinear components of the signal, namely the signals of the heartbeat and breathing mode.

Empirical Mode Decomposition is an appropriate technique to deal with the nonlinear and nonstationary neuromonitoring data, which not many data analysis methods can claim. Therefore, the combination of brain status data and weighted Sliding Empirical Mode Decomposition appears to offer promising results.

After a presentation of the used data sets in particular, the preprocessing with singular spectrum analysis will be introduced. The behavior of wSEMD facing real time series will be demonstrated analyzing the numerical accuracy, the compliance of the IMF criteria and the influence of the ensemble size on the decomposition.

Finally, wSEMD will be applied to the brain status data and the separation of

heartbeat and breathing mode with wSEMD will be presented. Additionally, the amplitude of the heartbeat mode will be examined on a very small time scale, whereby every period is considered. Subsequently, the mean amplitude averaged over 300 s will be discussed.

7.1 Data Set

The data was recorded in the intensive care unit of the Department of Neurosurgery of the University Hospital Regensburg during the treatment of patients with severe brain trauma. The data sets contain arterial blood pressure (ABP) and intracranial pressure (ICP) time series (see chapter 2). The sampling rate of the ABP and ICP data yields 1 kHz in order to be able to thoroughly scan the single heartbeats. The tissue partial oxygen pressure (TPO) can be recorded with an equally high sampling rate, however its $T90$ time amounts to 32 s. The $T90$ time means that, after a constant oxygen concentration, increasing it by 90 % the sensor needs 32 s to measure the new concentration correctly. Thus, it is not reasonable to consider TPO data with a sampling rate of more than 1 Hz. The TPO is, therefore, only employed for the analyses in chapter 6.
The analyses of the wSEMD algorithm are exemplified with the arterial blood pressure and later on also with the intracranial pressure of the data set PAT 14, a segment of which is depicted in figure 7.1. The high amplitude spikes are caused by the heartbeat and the slight longterm oscillations are generated by the mechanical ventilation of the patient.
The data exhibit failures of the sensors from time to time due to external manipulations by the medical staff. Those segments of the time series are replaced by negative values in advance and are generally omitted for the investigations.
In the following $n = 1, 2, \ldots, N$ denotes the samples of the data, which yields the temporal scale $t_n = n \cdot \Delta t_n$, with a time interval of $\Delta t_n = 0.001$ s between samples. Note that the amplitudes are reduced and have to be multiplied by a factor 100 to obtain the true values in [mmHg].

7.2 Singular Spectrum Analysis Preprocessing

Singular Spectrum Analysis (SSA) is a signal processing method mostly used for denoising or artifact reduction. In order to remove noise from the neuromonitoring data, SSA preprocessing is applied first to every single window of the time series.

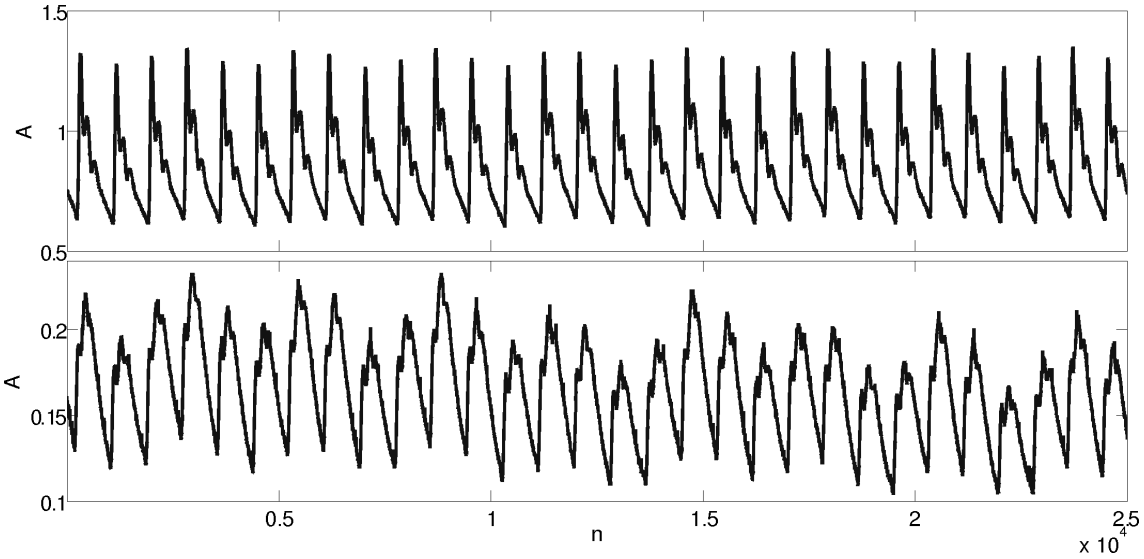

Figure 7.1 An ABP (top) and ICP (bottom) segment of the data set PAT 14 is shown. The ordinate illustrates the amplitude A and the abscissa the samples n of the data with an interval of $\Delta t_n = 0.001$ s between the samples.

After the reconstruction of the data with a smaller amount of eigenvectors, the time series are very smooth, yet the wave forms remain unchanged. The second advantage of the SSA preprocessing consists of the fact that the relevant, respectively, meaningful modes appear first after the decomposition with wSEMD, namely in IMF $1-5$ as will be described in section 7.6. Due to its high frequency, IMFs containing noise would appear at the beginning otherwise.

In the following – after a short review of the principle of SSA – the parameters of SSA, the size of the embedding matrix, the influence of the sample size and the number of eigenvectors to reconstruct the new time series will be investigated upon. Additionally, the SSA application to brain status data will be discussed. A part of the arterial blood pressure time series of the PAT 14 data set will demonstrate the properties of SSA regarding the choice of parameters.

7.2.1 The Principle of SSA

The great advantage of SSA is that it enables an analysis similar to Principal Component Analysis (PCA) [67] for univariate data. SSA [68, 69, 70] is a nonparametric spectral estimation technique, which first decomposes, then reconstructs a data set. The principle of SSA is based on embedding a time series in a vector space and conducting a Singular Value Decomposition. In the end the new time series is re-

constructed using subgroups of the decomposed data (algorithm see [71]). SSA will be described in detail in the following.

Embedding

The first step of Singular Spectrum Analysis is creating a matrix $\mathbf{A}$ out of a time series $a(t)$ via embedding with a time delay τ. Different subsets of values of the time series $a(t_l)$, called lagged vectors, form the data matrix or trajectory matrix:

$$\mathbf{A} = \begin{pmatrix} a(t_l) \\ a(t_l + \tau) \\ \vdots \\ a(t_l + n\tau) \end{pmatrix} \tag{7.1}$$

In case of the algorithm used in this thesis, the selected time delay amounts to $\tau = 1$. With the sample size N of the time series, the embedding parameter L with $l = 1, \ldots, L$ and the parameter $K = N - L + 1$ the data matrix adds up to:

$$\mathbf{A} = \begin{pmatrix} a(t_l) \\ a(t_l + 1) \\ a(t_l + 2) \\ \vdots \\ a(t_l + (K - 1)) \end{pmatrix} \tag{7.2}$$

yielding an $K \times L$ matrix. Note that $\mathbf{A}$ is a Hankel matrix with equivalent entries where the matrix indices $i + j = const.$ [72]. The further steps of the algorithm are carried out with this data matrix.

Decomposition

With the embedded matrix a Singular Value Decomposition (SVD) [67] is conducted. SVD describes a matrix $\mathbf{A}$ as a product of three specific matrices

$$\mathbf{A} = \mathbf{USV}^T \tag{7.3}$$

with which the singular values can be determined. Those characterize the properties of the matrix similar to eigenvalues. SVD can be applied to any – also non-quadratic – matrices. Singular Value Decomposition and the eigendecomposition are closely related. For a normal (e.g. square, real, symmetric matrices) matrix $\mathbf{A}$ the SVD is

equivalent to diagonalization via solving an eigenvalue problem.
In pracitical applications often the $L \times L$ lag-covariance matrix $\mathbf{C}_A$ of the embedded matrix is computed via:

$$\mathbf{C}_A = \mathbf{A}^T \mathbf{A} \tag{7.4}$$

After that $l = 1, \ldots, L$ eigenvectors and eigenvalues are calculated according to [73]:

$$\mathbf{C}_A \mathbf{E}_l = \lambda_l \mathbf{E}_l \tag{7.5}$$

The eigenvalues λ_l of $\mathbf{C}_A$ denote the partial variance in the direction of the eigenvectors $\mathbf{E}_l$. They are usually ordered by their magnitude.
The principal components $\mathbf{A}_l$ are obtained projecting the data onto each eigenvector:

$$\mathbf{A}_l = \mathbf{A}\mathbf{E}_l. \tag{7.6}$$

Reconstruction

Finally, the data set is reconstructed again using a subset of eigenvectors. The entire time series or parts of it, that correspond to trends or oscillations, can be reconstructed using linear combinations of a subset of principal components and eigenvectors, which then provide the reconstructed components. A diagonal averaging (hankelization) over all entries with matrix indices $i + j = const.$ is conducted in order to obtain an univariate time series as final result.

7.2.2 SSA Parameters

The influence of the single SSA parameters on the resulting eigenvalues and on the reconstructed time series are discussed in the following using neuromonitoring data.

Lag Parameter

One of the parameters influencing the eigenvalues resulting from the decomposition is the size of the $K \times L$ embedding matrix with $K = N - L + 1$. The size is composed of the segment size, that means the vector length of the lagged vectors L and the sample size of the complete time series N. In the following the focus will lie on the embedding parameter L and subsequently on the sample size N.
For a constant sample size of $N = 15\,000$ the embedding parameters $L = 25$, 50, 100, 200, 300, 400, 500 are used for the SSA decomposition. Figure 7.2 presents the eigenvalues sorted by their magnitude for different L. The ordinate is plotted

logarithmically as the magnitudes of the eigenvalues vary severely. The first 60 eigenvalues (for $L = 25$ all 25 and for $L = 50$ all 50) are presented in descending order for all embedding parameters. Qualitatively all curves look very similar displaying several bends. Due to the higher amount of eigenvalues for increasing lag parameter L a more finely graduated reconstruction of the data is possible. Whereas, for example, for $L = 25$ the first three eigenvalues cover several orders of magnitude, those of $L = 500$ cover only two.

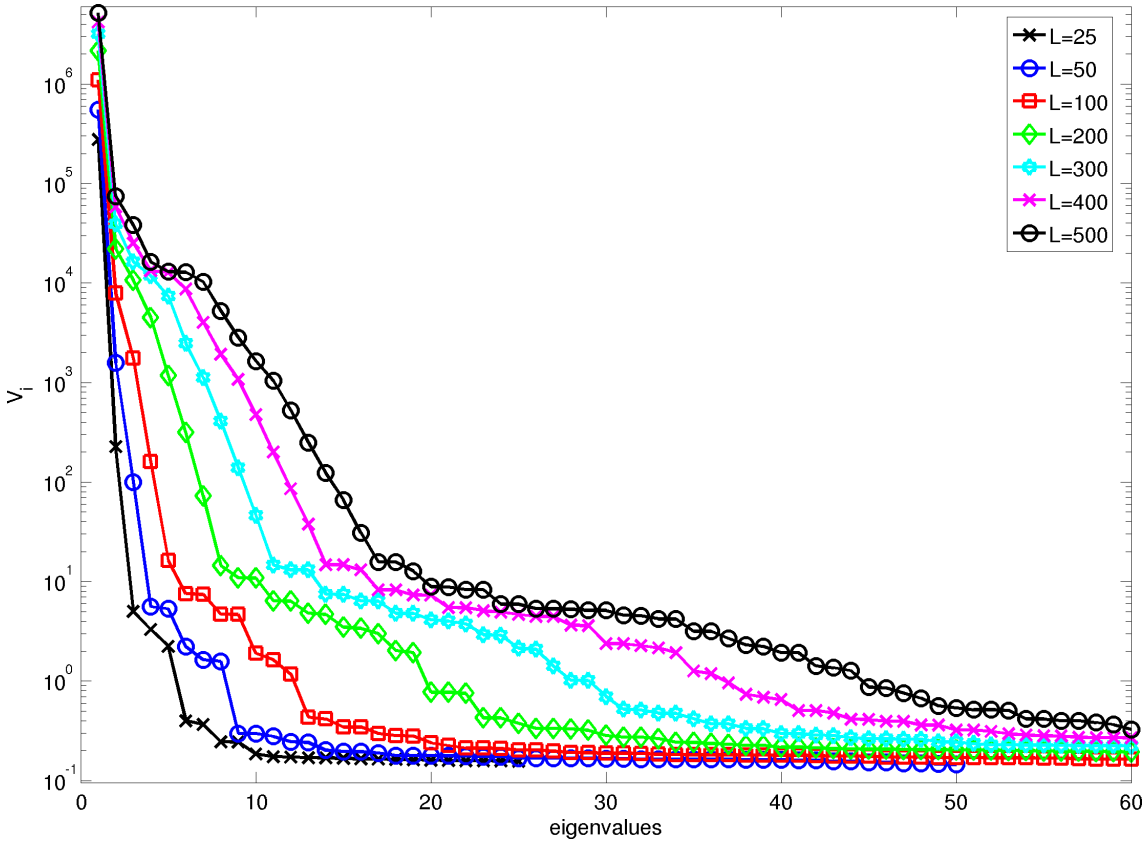

Figure 7.2 The eigenvalues of a part of the ABP of PAT 14 are shown after the SSA decomposition with different embedding parameters L, whereby the sample size is kept constant at $N = 15\,000$. The logarithmic ordinate gives the values V_i and the abscissa the number of the eigenvalues.

Selecting a large lag parameter, however, bears the disadvantage of a high computational load and demand of working memory of the computer. Due to that fact a trade-off between precision and computational requirement has to be found. Exhibiting a good compromise is $L = 50$, which will be used in the following.

Data Length

Another parameter influencing the decomposition results of SSA is the size of the input data N. For constant embedding parameter $L = 50$ the sample size is varied ($N = 500$, 1000, 2500, 5000, 10 000, 25 000, 50 000, 1 000 000, 2 000 000) for the SSA decomposition. Figure 7.3 illustrates the eigenvalues sorted by their magnitude for various N. Again, the ordinate is plotted in a logarithmic scale as the eigenvalues differ extremely. The first 20 of all 50 eigenvalues are illustrated in the diagram ordered by their magnitude with respect to the sample size N of the input data of the SSA decomposition. All curves run almost parallel, whereas the total amount of variance (sum of the eigenvalues) increases for increasing N, which renders the single magnitudes of the eigenvalues higher. Qualitatively the reconstruction of the time series should be similar for a fixed number of eigenvalues independent of the sample size.

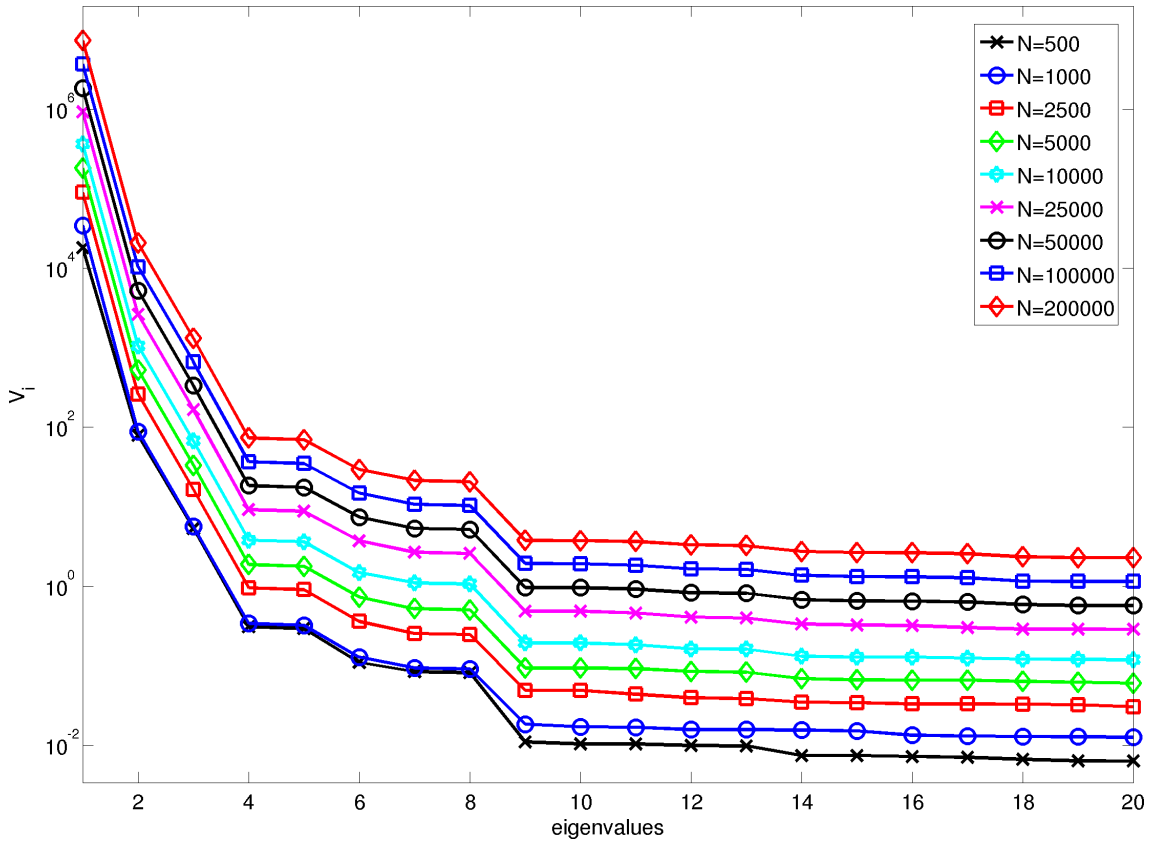

Figure 7.3 The first 20 eigenvalues of a part of the ABP of PAT 14 are shown after the SSA decomposition with different sample sizes N for embedding parameter $L = 50$. The logarithmic ordinate pictures the values V_i and the abscissa the number of the eigenvalues.

As the SSA preprocessing step is applied to all data windows of wSEMD first, the selection of the window size, which corresponds to the input data length N of SSA, is mainly influenced by the desired results of the wSEMD decomposition. Due to the altered frequency content of the IMFs and the residuum depending on the window size (see section 4.2), the focus of the determination of N lies within wSEMD.
A suitable window size for the wSEMD decomposition to cover the breathing and heartbeat mode (see section 7.6) is $N = 15\,000$, which will be used in the following. For the ICP time series of the PAT 14 data set the findings are qualitatively equal to those of the ABP time series.

Number of Eigenvalues

A very important parameter determining the results is the number of eigenvectors (EVs) to reconstruct the data. Their corresponding eigenvalues are arranged according to their contribution to the data. A high magnitude of the eigenvalue means a high variance of the data in that direction.
For the applications in the following the goal is a reconstruction of the low-frequency oscillations of the data omitting the high-frequency noisy modes.
Figure 7.4 presents a detail of the time series ABP of the PAT 14 data set reconstructed after SSA decomposition with a various amount of eigenvectors denoted by the different colors. Additionally, the original time series of this interval of the data is presented. Obviously only the first eigenvector is not sufficient to reconstruct the data, the center of the time series is not met properly. Using the first 2 respectively 3 eigenvectors to reconstruct the data the center is met well, whereas it seems that the third eigenvector is needed to retrace the low-frequency content of the original data entirely. Especially at extremal areas of the time series the reconstruction with 3 EVs (see magenta graph in fig. 7.4) meets the center of the original data best.
Figure 7.5 demonstrates the absolute values of the mean error (ME)

$$ME = \frac{1}{N} \sum_{n=1}^{N} \big(f(t_n) - f'(t_n)\big) \tag{7.7}$$

between $N = 15\,000$ samples of the original ABP time series $f(t_n)$ and the data after SSA reconstruction $f'(t_n)$ with $N = 15\,000$ and $L = 50$ and increasing numbers of eigenvectors. The more EVs are used for the reconstruction the more similar the result becomes to the original data. Additionally, a minimum appears using 4 eigenvectors to reconstruct the time series, however figure 7.4 illustrates that the reconstruction with EVs $1 - 4$ already contains too many fluctuations (of approxi-

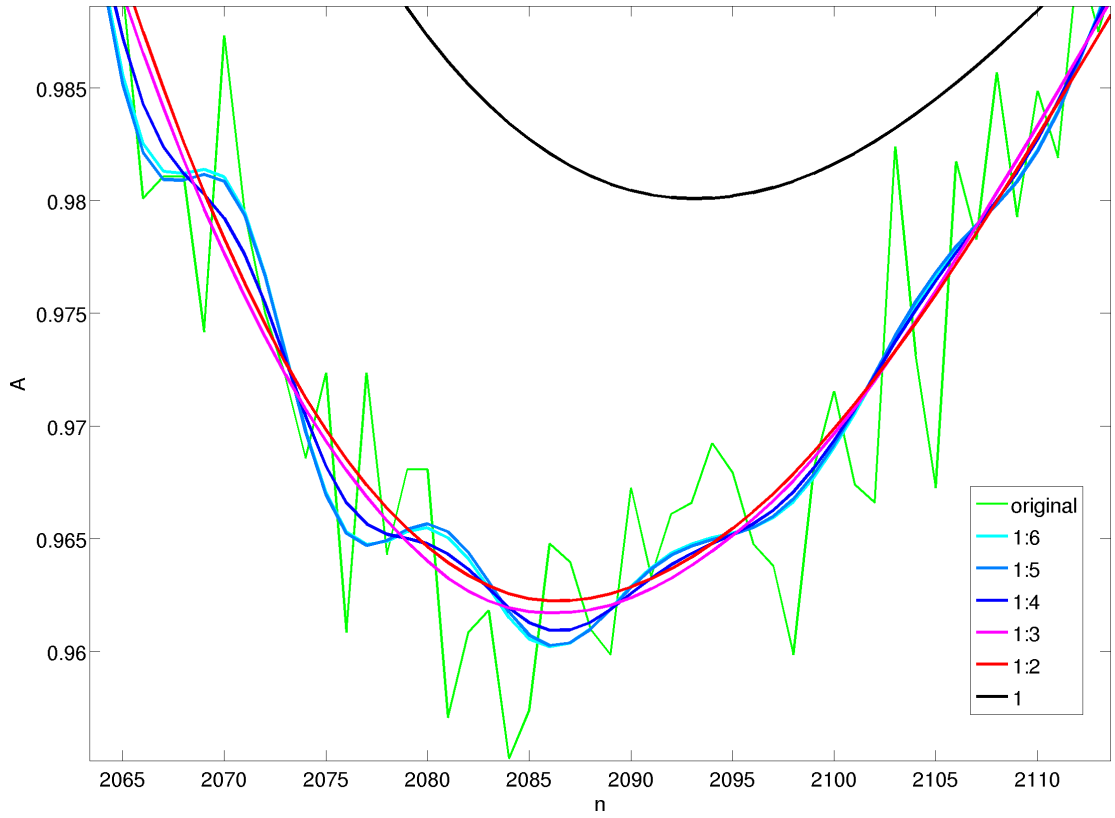

Figure 7.4 A detail of the time series ABP of PAT 14 is depicted after the SSA reconstruction ($N = 15\,000$ and $L = 50$) with different numbers of eigenvectors. Furthermore, the detail of the original data is plotted. The ordinate depicts the amplitude A and the abscissa the samples n of the data.

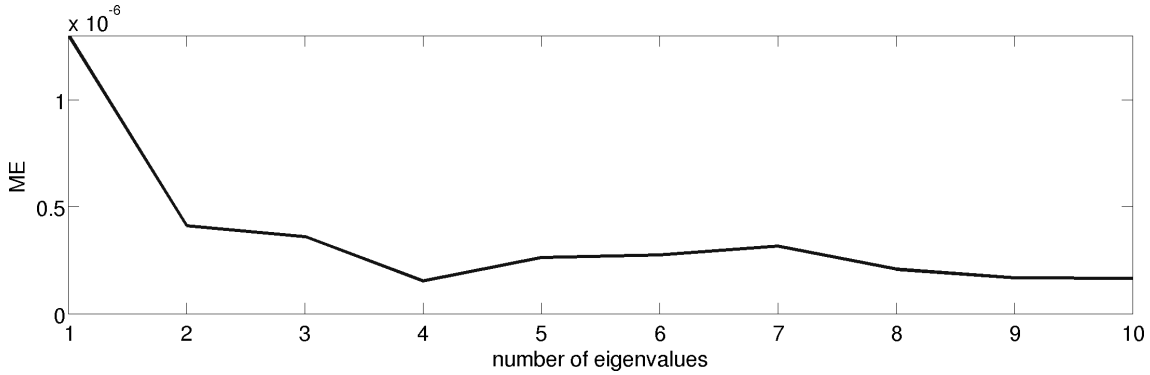

Figure 7.5 Absolute values of the mean error between the original time series ABP of PAT 14 and the new time series after SSA reconstruction ($N = 15\,000$ and $L = 50$) with ascending numbers of eigenvectors is displayed.

mately 90 Hz). Therefore, 3 eigenvectors will be used in the following to reconstruct the data as a good trade-off between reconstruction quality and noise reduction. Also for the ICP time series of the PAT 14 data set the results were qualitatively equal to those of the ABP time series and therefore EVs $1-3$ are used to reconstruct the ICP as well.

7.2.3 SSA Applied to Brain Status Data

Finally SSA is applied to neuromonitoring data. Figures 7.6 and 7.7 present a detail of the ABP and ICP time series of the PAT 14 data set. The upper trace, respectively, shows the original time series, whereas the bottom plots depict the SSA preprocessed data with a lag parameter of $L = 50$ reconstructed with 3 eigenvectors. After the reconstruction the time series look very smooth while the general appearance remains unchanged. SSA removes the noise, however, the wave form is conserved, which constitutes the advantage of that method. The preprocessing step works well for the ABP as well as for the ICP data. Therefore, it will be applied before the wSEMD decomposition of the pulsatile neuromonitoring time series.

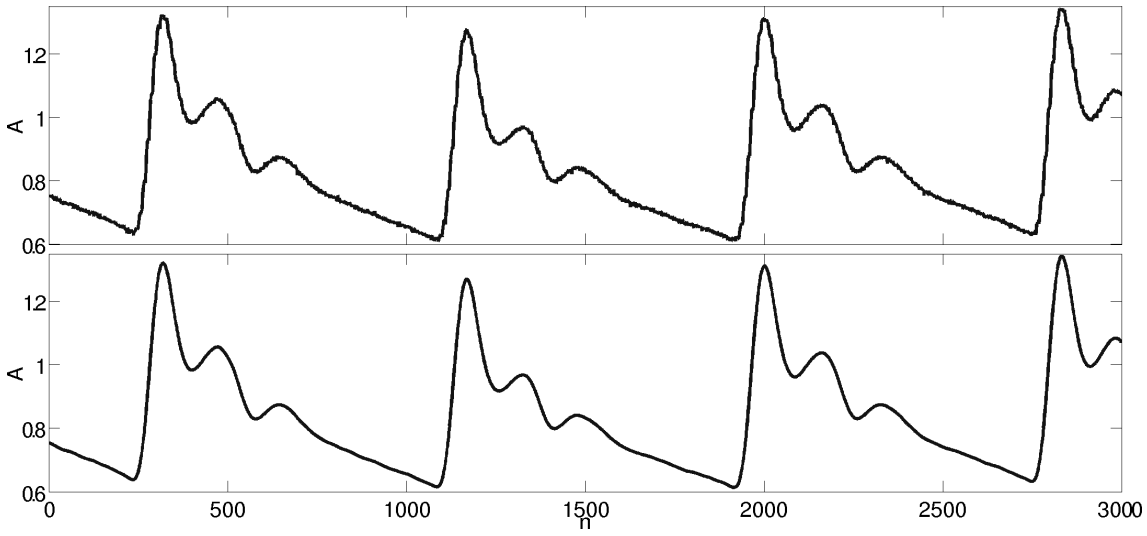

Figure 7.6 The figure depicts a detail of the original arterial blood pressure of PAT 14 (top) and the SSA preprocessed time series with $L = 50$ and a reconstruction from 3 eigenvectors (bottom). The ordinate shows the amplitude A and the abscissa the samples n of the data.

The advantage of the SSA preprocessing consists in the fact, that decomposing the reconstructed time series with wSEMD no noisy IMFs will be obtained. Those are to be avoided, since – depending on the noise – more or less IMFs containing noise can

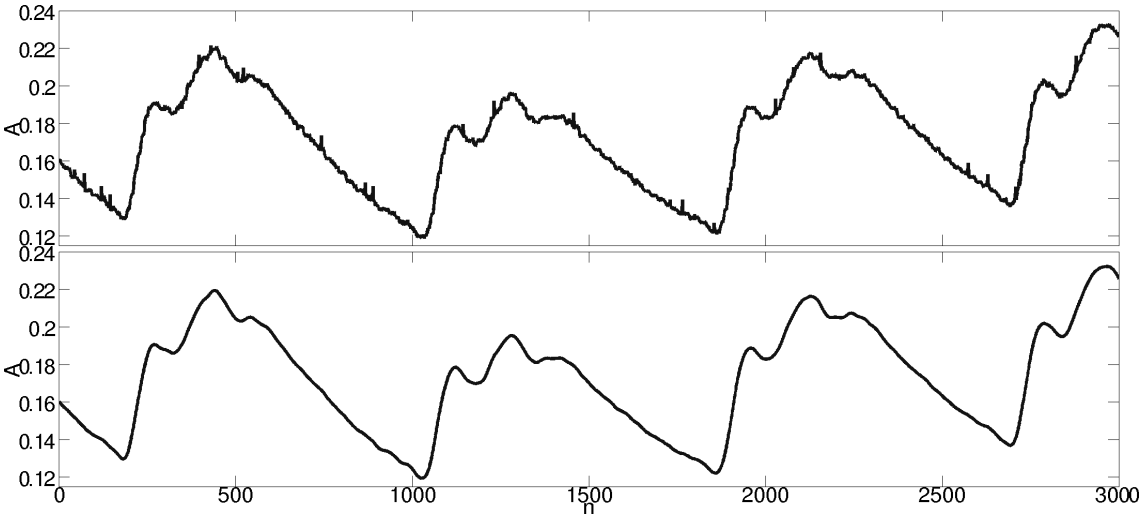

Figure 7.7 The figure depicts a detail of the original intracranial pressure of PAT 14 (top) and the SSA preprocessed time series with $L = 50$ and a reconstruction from 3 eigenvectors (bottom). The ordinate shows the amplitude A and the abscissa the samples n of the data.

be created, which renders the joining together of the windows of wSEMD difficult. On the other hand, with the important IMFs appearing first, namely in IMFs $1 - 5$ (see section 7.6), the ones containing relevant information do not have to be located first within the other IMFs. Therefore, the SSA preprocessing will be applied to the pulsatile neuromonitoring data in this thesis before wSEMD is operated.

7.3 Completeness and Numerical Accuracy

The completeness, respectively, the numerical accuracy of the applied wSEMD algorithm is tested also for the pulsatile neuromonitoring data. In this case a segment of the arterial blood pressure of the data set PAT 14 with 300 000 samples is used. The wSEMD algorithm is applied with window size $M = 15\,000$ and various ensemble sizes E covering all divisors of M. The SSA preprocessing is implemented with $L = 50$ using 3 eigenvectors to reconstruct the data.

However, the SSA preprocessing changes the original data and therefore the completeness has to be analyzed in comparison to the SSA preprocessed time series, not the original data. Thus, SSA is applied to the original data sliding a window of 15 000 samples with step size 1 over the time series and averaging over the estimates for every data point using the same dimension of the embedding matrix and number of eigenvectors to reconstruct the data. That way the input data for the

wSEMD algorithm is recreated and can be used to analyze the numerical accuracy of wSEMD applied to pulsatile brain status data. To do so, the mean squared error (MSE) between the reconstructed input time series and the sum of all IMFs and the residuum is calculated with respect to the ensemble size, which is illustrated in figure 7.8.

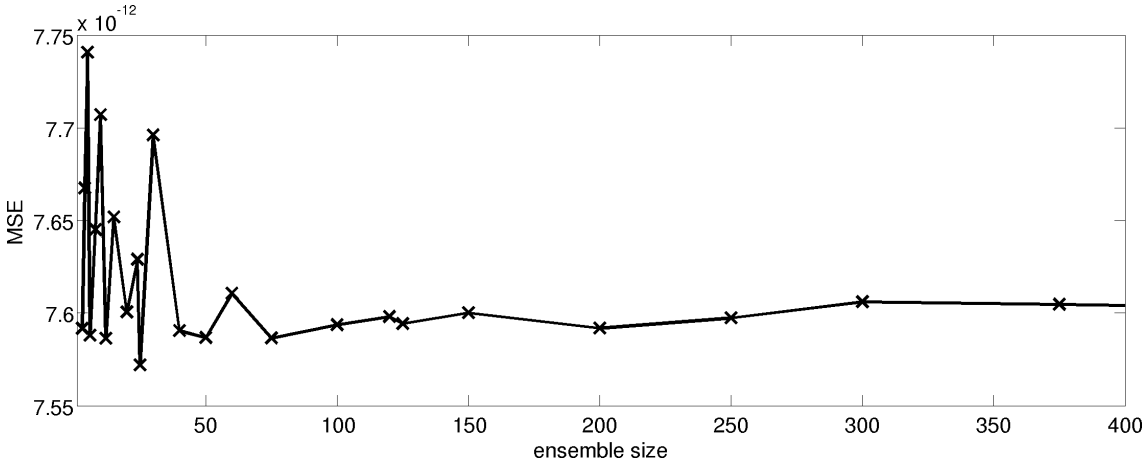

Figure 7.8 MSE comparing the sum of all IMFs plus the residuum and the input data reconstructed from the original data after SSA preprocessing. The mean squared errors are presented with respect to the ensemble size used for the wSEMD decomposition.

As before (see sections 5.2 and 6.3) the difference between the sum of all IMFs and the residuum of the neuromonitoring data with high sampling rate and the original data, reconstructed after the SSA preprocessing, is extremely small. After some fluctuations for large step sizes the MSE levels at a nearly constant and very small value of around 10^{-11}. The errors are by far below the accuracy of the measurements of the brain status data ($\pm 10\,\%$). The decomposition can, hence, be considered precise aside from those numerical inaccuracies and no information loss due to the decomposition can be observed. The basic requirement for the EMD decomposition is therefore fulfilled by the wSEMD decomposition of the neuromonitoring data.

7.4 Examination of the IMF Criteria

The IMF criteria (see section 3.1) can also be evaluated with the biomedical neuromonitoring data with high sampling rate. As an example for such a time series a part ($N = 300\,000$) of the arterial blood pressure of the PAT 14 data set is employed in the following. Again the local average of the upper and lower envelopes of the IMFs and difference between the number of extrema and zero crossings is

checked. The time series are decomposed with window size $M = 15\,000$ and ensemble sizes covering all divisors of M (see previous section). The SSA preprocessing is implemented with $L = 50$ using 3 eigenvectors to reconstruct the time series. Furthermore, all investigations are executed additionally with EMD to be able to compare both techniques. The IMF criteria are two of the few definitions EMD is based on. Their adherence is, thus, of importance.

7.4.1 Mean Value

The local average of the upper $U(t_n)$ and lower $L(t_n)$ envelopes, $m(t_n)$, is used to inspect, if the mean value is close to zero. For an investigation upon the mean value of the IMFs, the mean of the *absolute* values of $m(t_n)$, denoted by S

$$S = \frac{1}{N} \sum_{n=1}^{N} \mid m(t_n) \mid \tag{7.8}$$

is applied, whereas N denotes the number of samples. For comparison the average of the absolute values of $m(t_n)$ is shown for wSEMD and EMD averaged over the first 5 IMFs of both methods. The mean of the absolute values of the difference between upper and lower envelope S is computed depending on the ensemble size. Figure 7.9 illustrates S which is relatively small for both decompositions. After some fluctuations for small ensemble sizes, the parameter S of the wSEMD decomposition remains roughly constant. The IMFs of EMD reach smaller S values than the IMFs of wSEMD, however its mean of the absolute values of $m(t_n)$ is still sufficiently small. Therefore, one can say, that the first IMF criterion is fulfilled by wSEMD applied to neuromonitoring data.

7.4.2 Number of Extrema and Zero Crossings

The absolute value of the difference between the number of extrema and zero crossings (for convenience denoted with P in the following) with respect to the ensemble size is illustrated in figure 7.10 for IMFs $1-5$ of the ABP data of PAT 14 separately. Again results of the wSEMD and EMD decomposition are plotted, to be able to compare the different techniques. After some fluctuations for small ensemble sizes, the difference P of wSEMD remains roughly constant in the progress. For all IMFs the difference between extrema and zero crossings is smaller for the IMFs resulting of the wSEMD decomposition than the ones of EMD, except for the first IMF. For IMF 1 of wSEMD the difference P is relatively high. That stems from a jaggedness

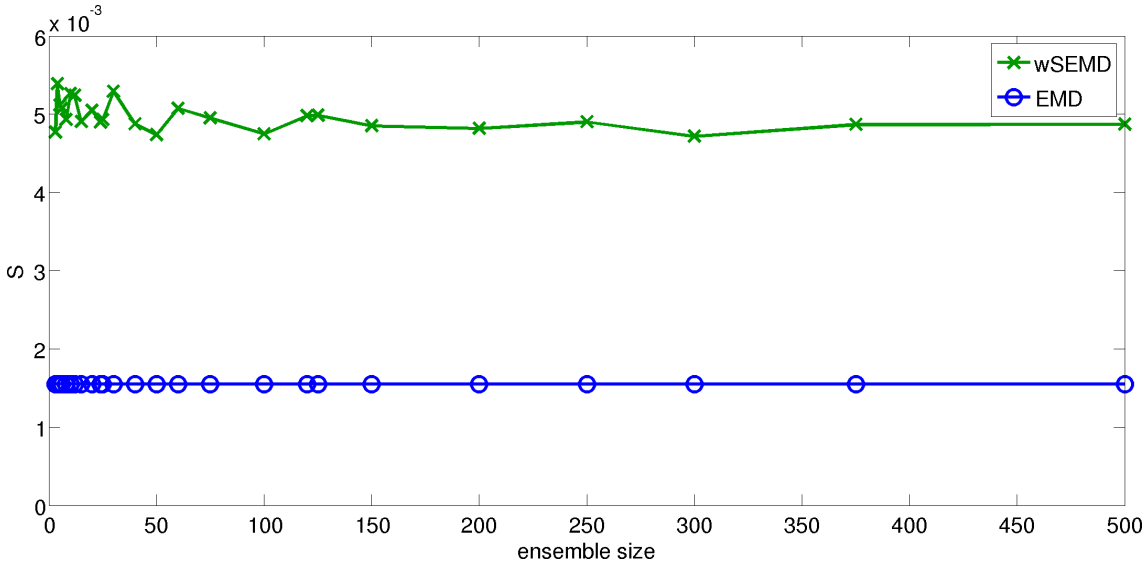

Figure 7.9 The ordinate of the diagram denotes the mean of the absolute values of the local average of the upper and lower envelope of the IMFs of the PAT 14 ABP data, indicated by S. It is depicted with respect to the ensemble size for the wSEMD ($M = 15\,000$) and EMD decomposition averaged over the first 5 IMFs.

of the signal in some areas, which produces additional extrema, regardless of the distance between them.

This jitter appears especially in intervals with a relatively flat signal, however it exhibits very small fluctuations. The interval between the amplitudes of most of these extrema underrun the measurement precision of the data by far, yet they are counted by the algorithm. To examine the extrema closely, first, the mean amplitude of the ABP signal is calculated. On that account, the highest maximum and lowest minimum of every heartbeat period of the time series is determined. In a time period of 300 s, about $N_{\max} = 300$ of those maxima ($n_{\max}$) and $N_{\min} = 300$ of those minima ($n_{\min}$) of the time series are located. The mean amplitude is calculated averaging over the y-values of the maxima $A(n_{\max})$ and minima $A(n_{\min})$ separately and summing up their absolute values. The result is divided by the factor 2:

$$A = \frac{1}{2}\left(\left|\frac{1}{N_{\max}}\sum_{n=1}^{N_{\max}} A(n_{\max})\right| + \left|\frac{1}{N_{\min}}\sum_{n=1}^{N_{\min}} A(n_{\min})\right|\right) \tag{7.9}$$

Also the amplitude differences between all extrema, not just the two extrema of every heartbeat period, are calculated. They are indicated by D_i and are defined as the absolute differences between the amplitude of a minimum and of its subsequent maximum and vice versa. As an example IMF 1 of the ABP signal decomposed

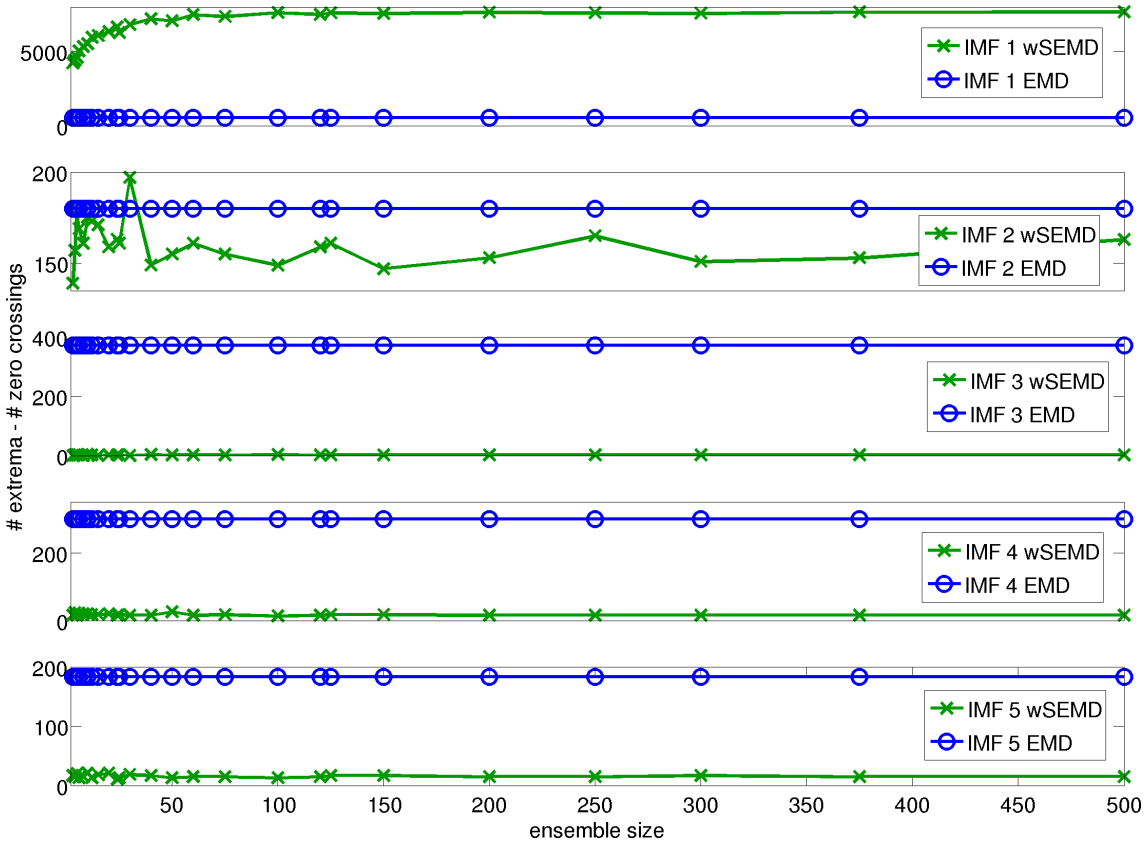

Figure 7.10 The illustration shows the absolute difference between extrema and zero crossings of IMFs $1-5$ of the PAT 14 ABP time series. EMD and wSEMD ($M = 15\,000$) decompositions are compared with respect to the ensemble size.

with ensemble size $E = 50$ is considered. Its mean amplitude yields $A = 0.34$. Its total number of extrema is 11 676 and the number of zero crossings amounts to 4 607, in this case. Therefore, 7 069 "wrong" extrema are located, which constitutes 60 % of the found maxima and minima. The amplitude differences D_i between the extrema of IMF 1 yield, that 79 % of D_i are smaller than $0.01 \cdot A$ and 70 % of D_i are even smaller than $0.001 \cdot A$. Thus, the amplitude differences between those wrong additional extrema are marginal.

See figure 7.11 depicting a detailed view of IMF 1 of the ABP time series (decomposed with EMD and wSEMD with $E = 50$) for an example of the jitter: The counted maxima and minima are marked with crosses and circles, respectively. The amplitude differences are hardly recognizable for the wSEMD time series. Therefore, the large difference between extrema and zero crossings is to be contemplated critically. Those additional extrema cannot be regarded as typical riding waves. In contrast, the same interval resulting from EMD features a noisy signal oscillating

with about 350 Hz, instead of a constant signal, producing more zero crossings, which formally leads to a better ratio of extrema and zero crossings for EMD.

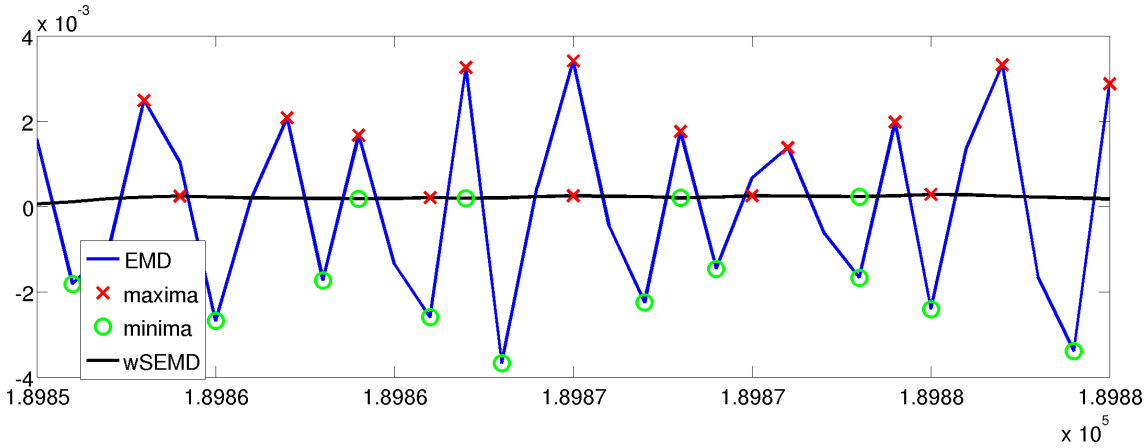

Figure 7.11 Illustrated is a detail of IMF 1 of the ABP time series decomposed with EMD and wSEMD ($E = 50$). The markers indicate the maxima and minima to be counted. The ordinate gives the amplitude A of the time series and the abscissa depicts the samples n.

Both algorithms formally do not adhere to the IMF criterion, the difference between extrema and zero crossings is larger than 1. The reason for this is that the stopping criterion of the used algorithm (for EMD and wSEMD) does not directly check the compliance of the second IMF criterion, but applies a constant number of sifting steps, namely 10. The advantage is, that equivalent oscillatory modes are found in identical IMFs so that averaging is possible.
All in all one can conclude that the first IMF criterion is fulfilled for brain status data. The second IMF criterion, however, is formally neither achieved by wSEMD, nor by EMD. But the difference between extrema and zero crossings is mostly small. Thus, the application of wSEMD to biomedical data can be conducted.

7.5 Influence of the Ensemble Size

In contrast to toy data, it is not possible for real data to compare the IMFs to the original components in order to assess the reconstruction quality. Thus, the IMFs resulting from the decomposition with ensemble size $E = i$ are compared to the IMFs obtained by the ensemble size $E = j$, whereas $E = i$ and $E = j$ are "neighboring" ensemble sizes. That means, we compare successive ensemble sizes, respectively, divisors of the window size M. The idea behind this test is to identify ensemble sizes that are big enough, so that the resulting IMFs are robust against

further increase. As method for the comparison the mean squared error (MSE) is used again.
A part ($N = 300\,000$) of the ABP data of PAT 14 is decomposed with wSEMD using a fixed window size of $M = 15\,000$ and all divisors of M served as ensemble size parameters. In figure 7.12 the MSEs between decompositions with subsequent ensemble sizes $E = i$ and $E = j$ are shown averaged over the first 5 IMFs. The MSEs between the IMFs change the most for small subsequent ensemble sizes. With increasing ensemble sizes the MSEs decrease and become very small and roughly constant. Beginning with an ensemble of about $E = 50$ the IMFs of the decomposition with wSEMD are therefore very similar, so that for practical applications an ensemble size of $E = 50$ seems to constitute a good trade-off between decomposition quality and computational load.

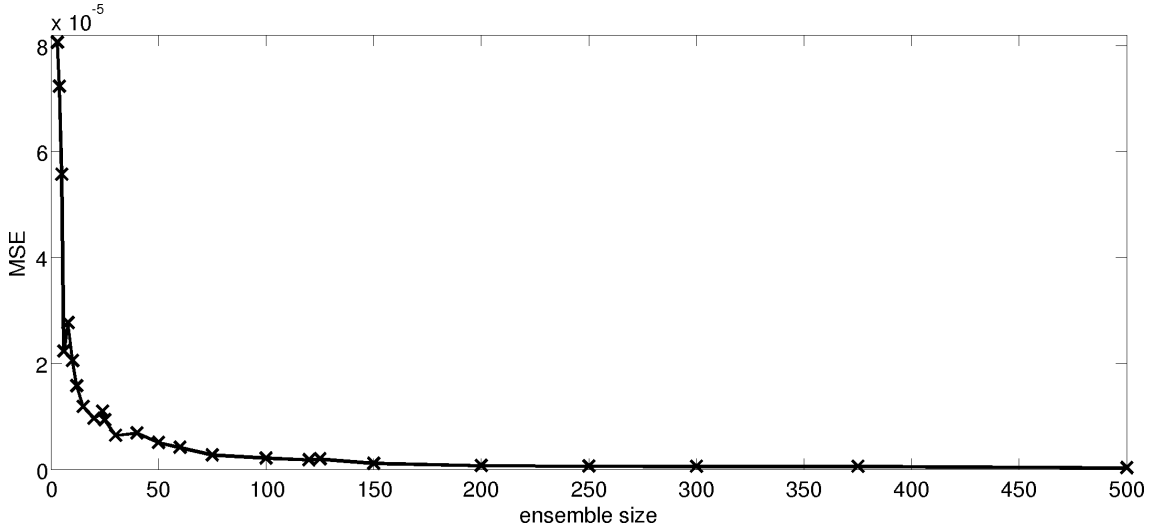

Figure 7.12 MSEs between IMFs of the wSEMD decomposition with $E = i$ and their subsequent ensemble sizes $E = j$ averaged over IMF $1 - 5$ are shown. The ensemble sizes of the x-axis hereby mean those, which are compared to their successor, e.g. $E = 50$ is compared to $E = 60$. As exemplary neuromonitoring time series the ABP of PAT 14 is used.

Additionally, all ensemble sizes $E = j$ are compared to the IMFs of the decomposition with step size $K = 1$, meaning $E = 15\,000$, which is supposedly the most precise decomposition result of wSEMD, as this parameter yields most suggestions for one data point. As before the window size $M = 15\,000$ is employed and the different divisors of M are utilized as ensemble sizes. Figure 7.13 shows the MSEs between the IMFs $1, 2, \ldots, 5$ decomposed with wSEMD using $E = 15\,000$ and utilizing ensemble sizes $E = j$.

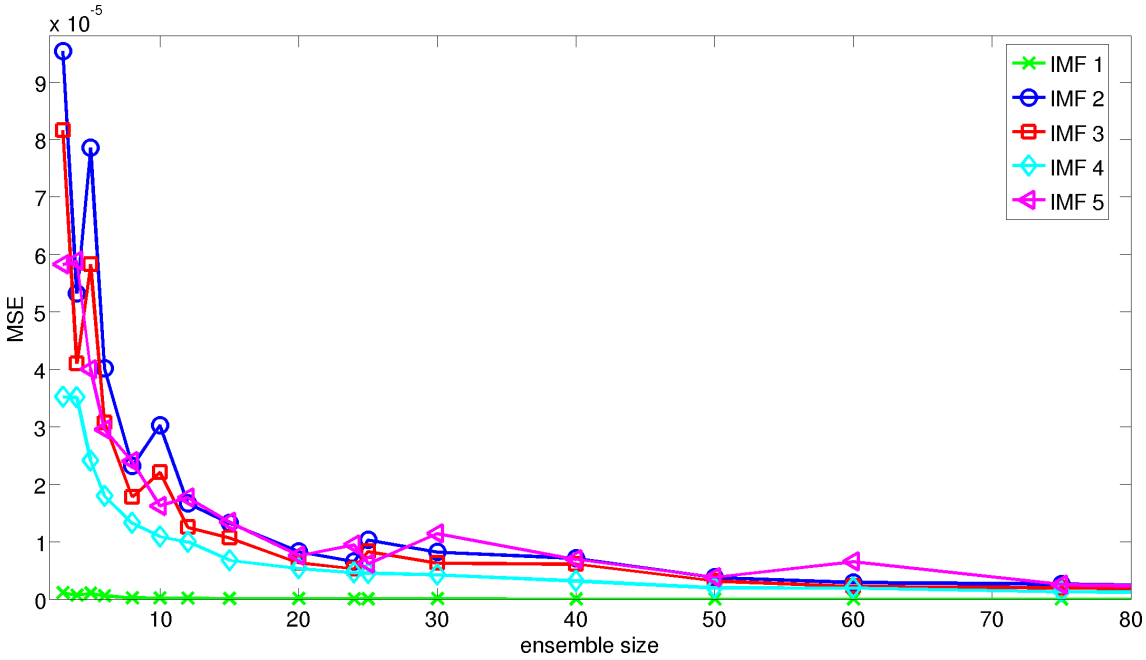

Figure 7.13 MSEs between IMFs $1, 2, \ldots, 5$ of the wSEMD decomposition with $E = 15\,000$ and all other ensemble sizes $E = j$ are depicted. As exemplary brain status time series the ABP of PAT 14 is utilized.

Again, after some fluctuations of the MSEs for small ensemble sizes, the decomposition results do not differ much for increasing E and become almost constant. It is obvious that IMF 1 with the highest frequency demonstrates the smallest MSEs and thus the highest resemblance of all IMFs for various parameters E, while the appearance of the following IMFs varies stronger with changing ensemble size.

The reason for this is presumably, that imprecision or errors emerge at the high-frequency IMFs and those defects propagate to signal components extracted later. Furthermore, the low-frequency IMFs feature the least amount of extrema and thus knots for the spline interpolation. Their reconstruction is, hence, most prone to inaccuracy.

Concluding it is to say that the decomposition with wSEMD using small ensemble sizes is susceptible to defects or inaccuracies, however beginning with approximately $E = 50$ the decomposition results become very stable and the differences between the decompositions executed with different parameters become very small. Hence, the latter ensemble size marks a good trade-off between decomposition quality and computational load and can be used for practical applications, for which computation time is an important factor.

7.6 Separating Heartbeat and Breathing Mode

Two especially interesting oscillatory components exist within the neuromonitoring data, namely the heartbeat and the breathing mode. The heartbeat mode possesses a frequency of roughly 1 Hz and the breathing produces a frequency of roughly 0.25 Hz, whereas its period is relatively constant, as the patients are ventilated mechanically. Separating the heartbeat and breathing mode of the neuromonitoring signals, the arterial blood pressure (ABP) and intracranial pressure (ICP), would be very helpful for facilitating analyses to truly understand the data.

Comparing the behavior of heartbeat and breathing mode in the ABP and ICP components and especially locating differences between both measurements, interesting insights in the status of the patients can be gained. The advantage would additionally be, that changes of the condition of the patient can be registered with a high temporal resolution, almost in real-time, since the periods of the observed oscillations are very short and variations occur on a small time scale.

The separation will be executed with wSEMD in the following for the arterial blood pressure and the intracranial pressure. With the help of the SSA preprocessing step the noise components have already been removed. Thus, the relevant modes are to be found in the first IMFs containing the highest frequencies.

7.6.1 Arterial Blood Pressure

Figure 7.14 depicts the first 5 IMFs of the decomposition of an ABP segment (50 s) of the PAT 14 data set. The decomposition is performed with wSEMD using a window size of $M = 15\,000$ and a step size of $K = 1$, whereas the SSA preprocessing step is operated with $L = 50$ and 3 eigenvectors are used to reconstruct the data. Figure 7.15 shows the fast Fourier transforms (FFTs) of IMFs $1 - 5$. The first three IMFs feature a higher frequency than IMF 4 and 5. The FFTs illustrate clearly that IMFs $1 - 3$ feature a frequency of around 1 Hz and its harmonics and therefore belong to the heartbeat and IMFs $4 - 5$ exhibit oscillations with a period of about 4 s and show thus the breathing component. As could already be suspected examining figure 7.1 the heartbeat mode is not an IMF and does not obey the IMF criteria, that the number of extrema and zero crossings has to be equal, respectively, has to differ at most by one and that the local average of the upper and lower envelopes of an IMF has to be zero. Therefore, it is not surprising to find the heartbeat oscillations split up into three different IMFs and equally the breathing mode divided into two components.

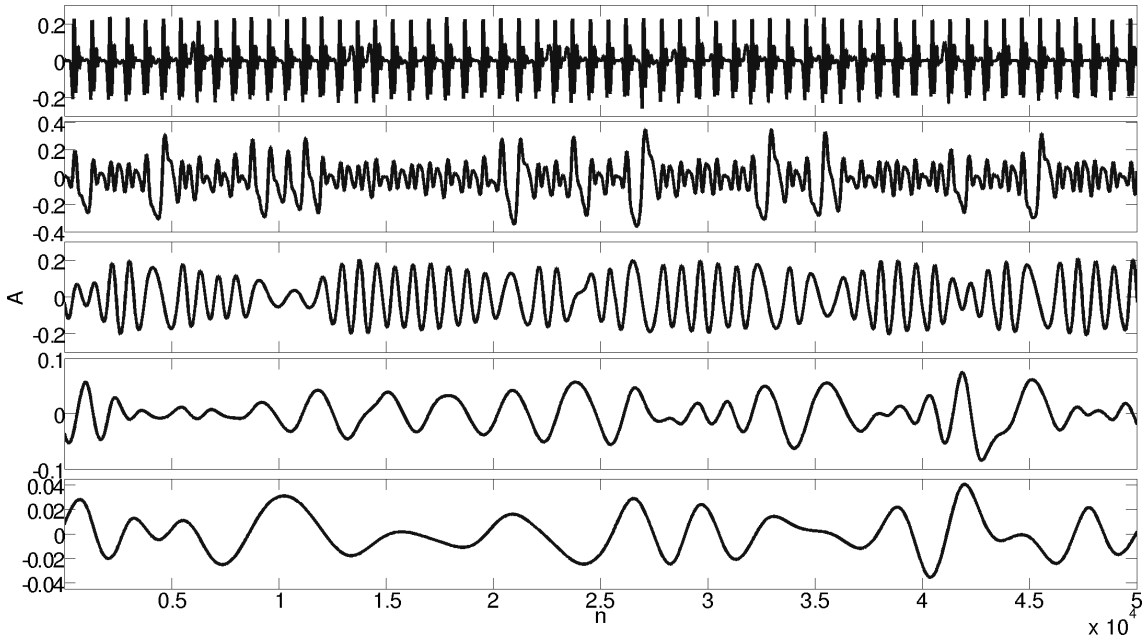

Figure 7.14 IMFs 1-5 of wSEMD ($K = 1, M = 15\,000$, preprocessed with SSA $L = 50$, 3 EVs) of an ABP segment of PAT 14 are shown containing the heartbeat and breathing modes. The ordinate shows the amplitude A and the abscissa the samples n of the data.

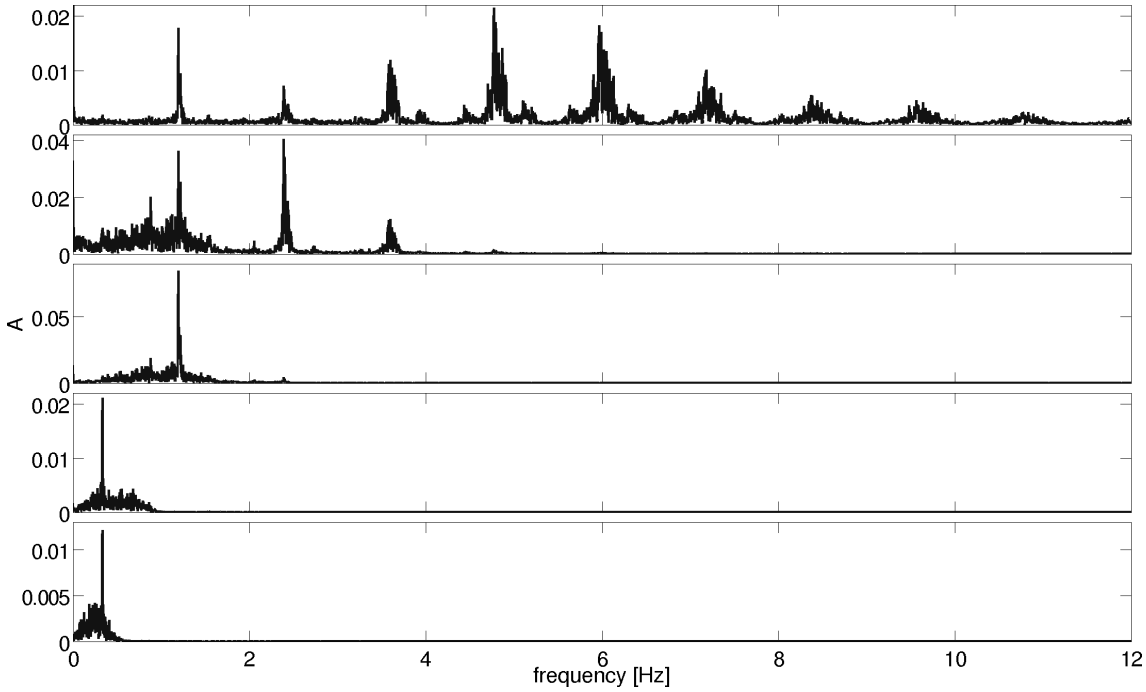

Figure 7.15 The FFTs of IMFs 1-5 of an ABP segment of PAT 14 are shown, featuring the heartbeat and breathing modes. The ordinate holds the amplitude A and the abscissa the frequency of the time series measured in Hz.

Figure 7.16 illustrates the sum of IMFs $1-3$, respectively, the heartbeat (top) and IMFs $4-5$, respectively, the breathing mode (bottom) and figure 7.17 additionally depicts the FFTs of both signals. In those figures one can observe clearly the very good frequency separation between the two oscillations. According to the FFTs the heartbeat mode exhibits a frequency of around 1.2 Hz and consists of this main frequency contribution together with its harmonics. The breathing component features a clear and steep peak at around 0.3 Hz. In the combined signals no mode mixing is observable in the FFTs and in the time series only one period of the heartbeat with slightly reduced amplitude is observable at the end.

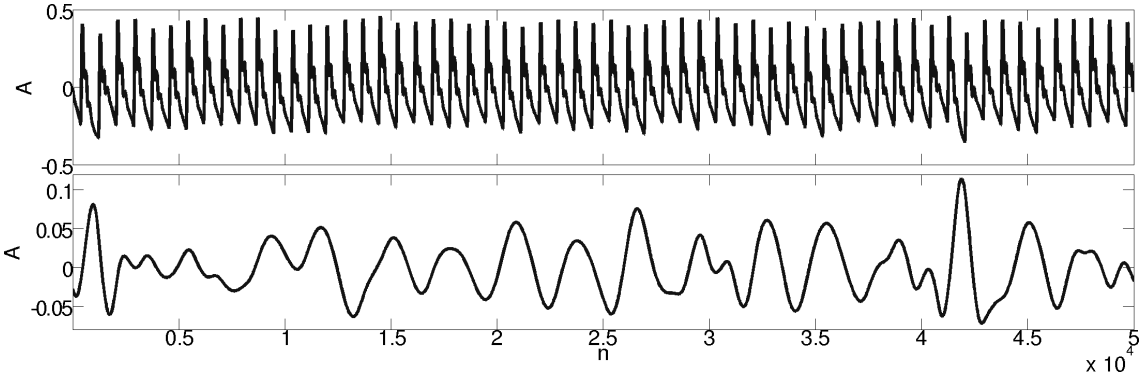

Figure 7.16 The heartbeat composed of IMFs 1-3 (top) and the breathing mode constructed by IMFs 4-5 (bottom) of the ABP time series of PAT 14 is illustrated. The ordinate illustrates the amplitude A and the abscissa the samples n of the data.

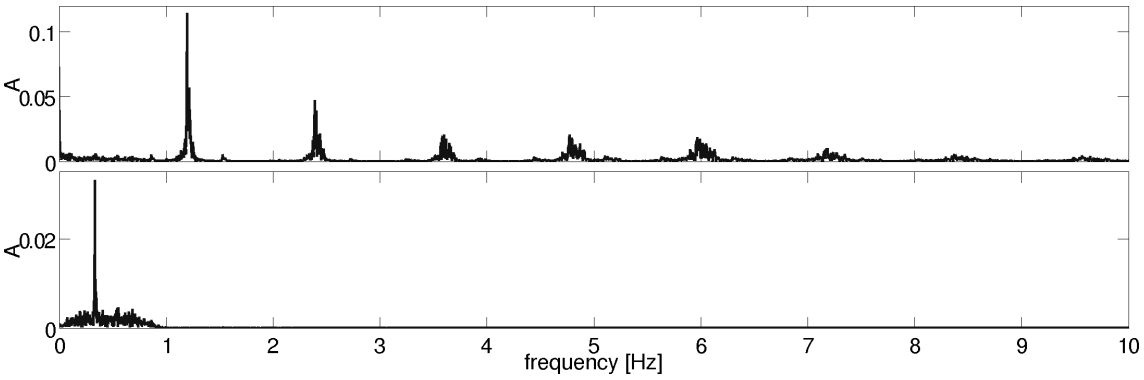

Figure 7.17 The FFT of the heartbeat composed of IMFs 1-3 (top) and the breathing mode constructed by IMFs 4-5 (bottom) of the ABP data of PAT 14 is depicted. The ordinate holds the amplitude A and the abscissa the frequency of the time series in Hz.

The data in the time domain, as well as the data in the frequency domain, generally appear very regular and smooth. By optical inspection wSEMD seems to success-

fully separate heartbeat and breathing mode. A more thorough and systematic investigation will be performed in section 7.6.3.

7.6.2 Intracranial Pressure

A similar analysis is now accomplished for the intracranial pressure, in order to observe its response to the decomposition with wSEMD. The parameters of wSEMD applied in this case are $M = 15\,000$ and a step size of $K = 1$ and the SSA preprocessing step is performed with $L = 50$ and 3 eigenvectors are used to reconstruct the time series. Figure 7.18 illustrates IMFs $1 - 5$ of the decomposition of an ICP segment of 50 s of the PAT 14 data set, which is isochronic to the previously presented interval of the ABP time series. Figure 7.19 shows the individual FFTs of the first 5 IMFs.

The first 3 IMFs feature a higher frequency than IMF $4-5$. The FFTs depict clearly that IMFs $1 - 3$ possess a frequency of around 1 Hz and its harmonics and therefore belong to the heartbeat and IMFs $4 - 5$ show the breathing component, since they feature oscillations with a period of ca. $3 - 4$ s. As already demonstrated with the ABP data, the heartbeat mode is not an IMF and thus does not obey the IMF criteria. Hence, it is expected to find the heartbeat oscillations divided into three different IMFs and equivalently the breathing mode split up into two components.

Figures 7.20 and 7.21 show the sum of the first 3 IMFs (the heartbeat mode, top) and IMFs $4 - 5$ (the respiration mode, bottom) and in addition the FFTs of both time series. In those illustrations one can observe the good separation of the frequency of the two modes. According to the FFTs, the heartbeat mode exhibits a frequency of around 1.2 Hz and, again, consists of this main frequency contribution together with its harmonics. The breathing component possesses a distinct and steep peak at around 0.3 Hz. Mode mixing is not observable in the FFT of the combined signals, however at two points in time of the heartbeat time series the amplitude looks a little shortened, whereas simultaneously the breathing amplitude is slightly increased. The data in the time domain, as well as the data in the frequency domain, appear very regular and smooth in general. The separation seems to have succeeded judging by optical inspection.

Generally, the heartbeat oscillation seems to be more easily extractable, since mode mixing in the breathing mode, stemming from the heartbeat with its high amplitude, disturbs the breathing more than the other way around. Furthermore, the amplitude ratios of the breathing and heartbeat mode is different in the ABP and ICP. For the ABP it amounts to approximately 0.15, whereas it adds up to about 0.4 for the ICP.

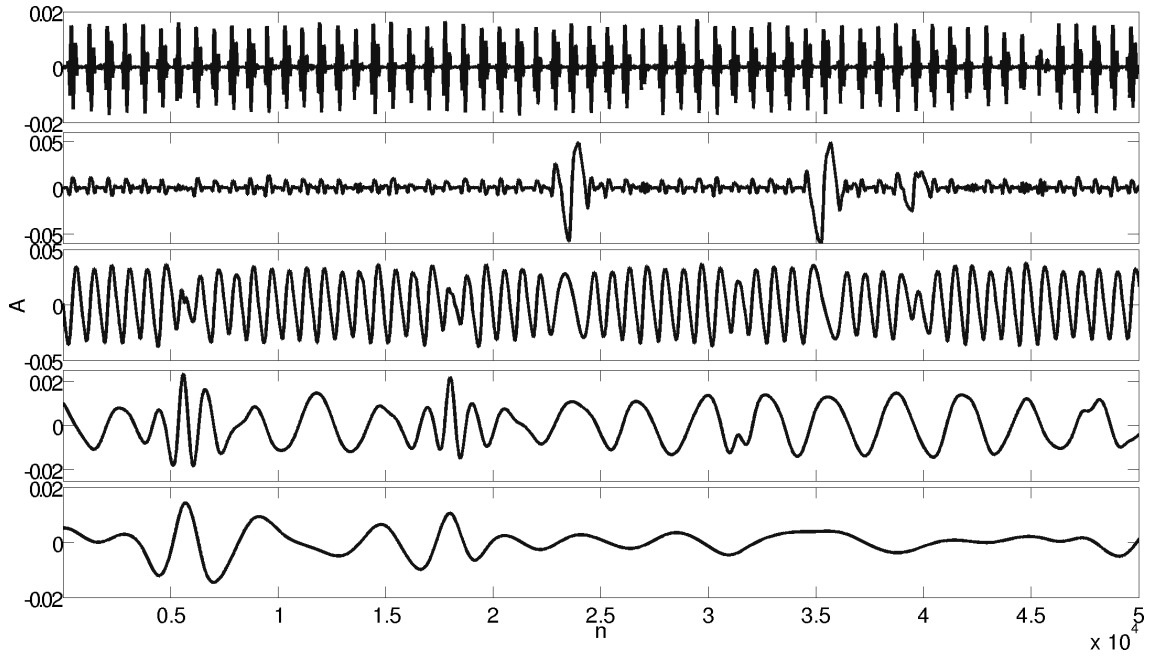

Figure 7.18 IMFs 1-5 of wSEMD ($K = 1, M = 15\,000$, preprocessed with SSA $L = 50$, 3 EVs) of an ICP segment of PAT 14 are shown containing the heartbeat and breathing modes. The ordinate shows the amplitude A and the abscissa the samples n of the data.

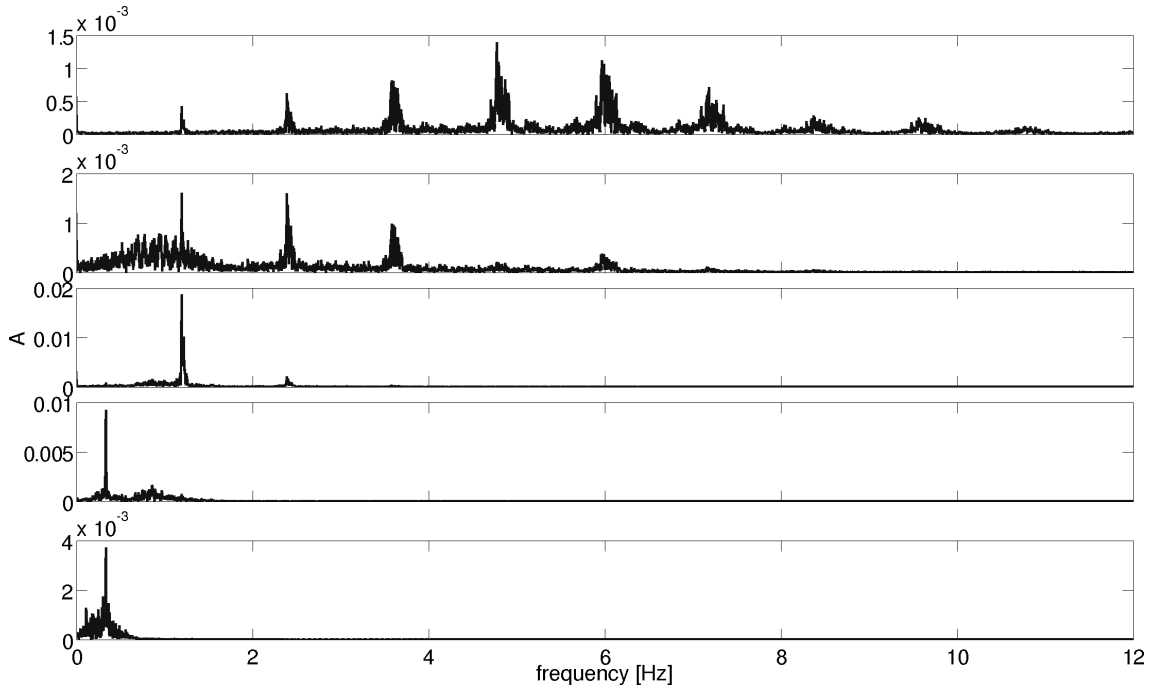

Figure 7.19 The FFTs of IMFs 1-5 of an ICP segment of PAT 14 are shown, featuring the heartbeat and breathing modes. The ordinate holds the amplitude A and the abscissa the frequency of the time series measured in Hz.

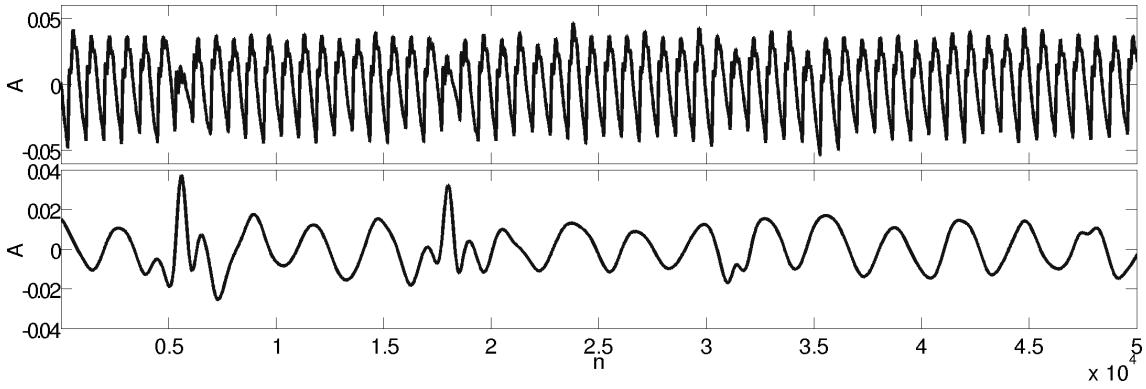

Figure 7.20 The heartbeat composed of IMFs 1-3 (top) and the breathing mode constructed by IMFs 4-5 (bottom) of the ICP time series of PAT 14 is illustrated. The ordinate illustrates the amplitude A and the abscissa the samples n of the data.

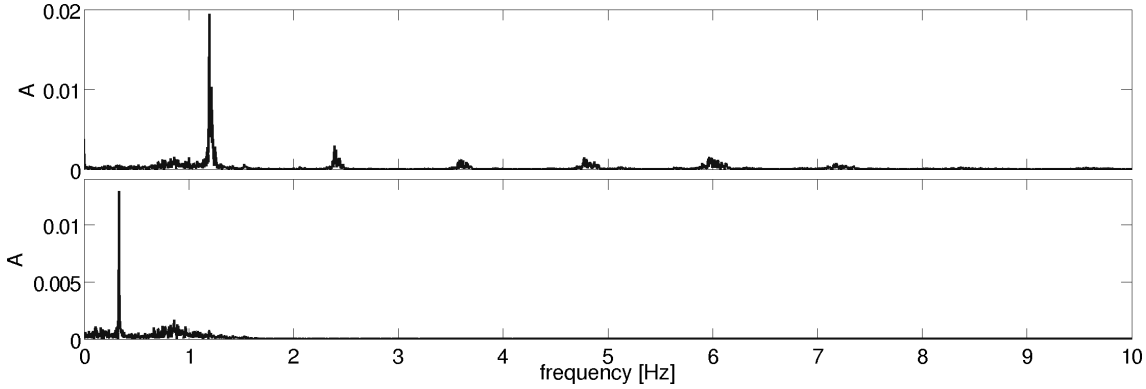

Figure 7.21 The FFT of the heartbeat composed of IMFs 1-3 (top) and the breathing mode constructed by IMFs 4-5 (bottom) of the ICP data of PAT 14 is depicted. The ordinate holds the amplitude A and the abscissa the frequency of the time series in Hz.

This may also render the decomposition of the ICP into heartbeat and breathing mode easier.

However, in the following a thorough analysis concerning the separation of heartbeat and breathing mode will be operated.

7.6.3 Analysis of the Separability

In order to examine the quality of the heartbeat and breathing mode separation of the ABP and ICP, both will be compared in the following. The whole data set PAT 14 with the sample size $N = 74\,100\,000$, corresponding to approximately 21 h of data, constitutes a rather short data set. It is utilized in the following and first

preprocessed with SSA using, again, a lag parameter of $L = 50$ and 3 eigenvectors to reconstruct the data. ABP and ICP are decomposed employing a window size of $M = 15\,000$ and an ensemble size of $E = 50$ so that $K = 300$, as those parameters offer a reasonable number of estimates for practical applications (see section 7.5).

Original Data/IMFs $1-5$: ABP compared to ICP

Before the heartbeat and breathing mode are decomposed, the general benefit of the wSEMD separation is tested first. Therefore, the whole original ABP and ICP time series are split up into segments of $N_i = 300\,000$ samples, respectively, 300 s. For every of those 300 000 sample intervals of the data the correlation and mutual information (MI) [74] (for the algorithm see [75]) between the isochronic segments of the ABP and ICP time series of PAT 14 is computed, in order to evaluate the amount of interdependencies present within the data. In contrast to the original data, the same correlational calculations are applied for the SSA/wSEMD preprocessed data between the summed up IMFs $1-5$ of the ABP and ICP time series of PAT 14, which represent the heartbeat plus the breathing mode. Note that for the parts of the time series exhibiting a failure of the sensor the correlation and MI coefficient is set to -1.

The correlation and MI between the ABP and ICP of the original data is depicted in figure 7.22. The analysis results between IMFs $1-5$ (heartbeat and breathing mode) of ABP and ICP are shown in figure 7.23. Note that the upper limit for

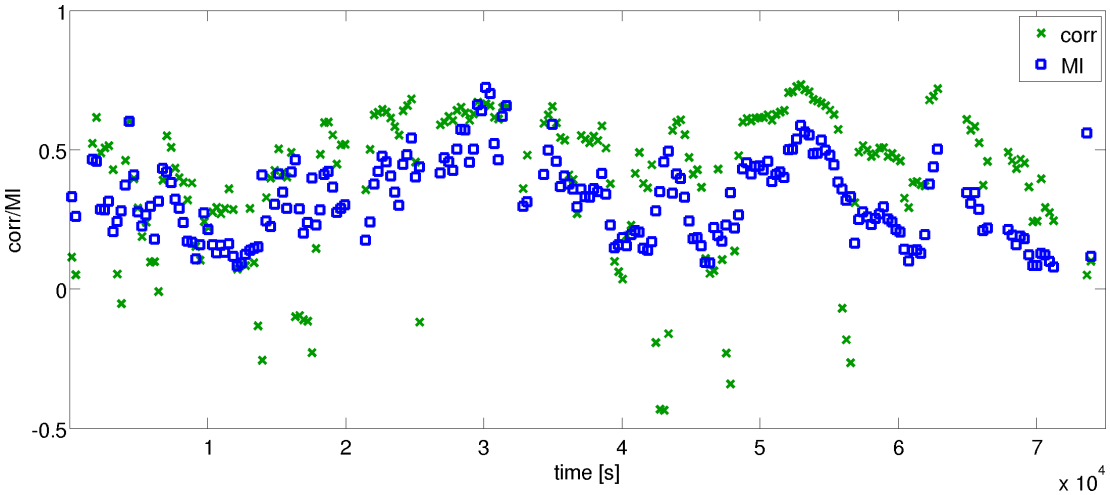

Figure 7.22 The figure presents the correlation and MI coefficients for intervals of 300 000 samples, respectively, between the original ABP and ICP data of PAT 14. The ordinate denotes the correlation, respectively, MI coefficients and the abscissa time in seconds.

the mutual information is larger than 1, in contrast to the correlation, which can also adopt negative values. It is obvious that the correlation graphs obtained for the wSEMD filtered data appear smoother and exhibit a smaller amount of outliers. Moreover, the correlation values are quantitatively much lower for the raw original ABP and ICP data and are spread over a wider range. The two test methods, correlation and mutual information, are well in accord. Generally very high values are obtained for the wSEMD filtered time series. The mean of the correlation time series of the original data amounts to 0.40, the MI to 0.33, whereas for the wSEMD filtered data the average correlation accounts 0.64 and the MI 0.62. The filtering, therefore, seems to be able to remove noise and other undesired signal modes, which results in increased correlation and MI coefficients.

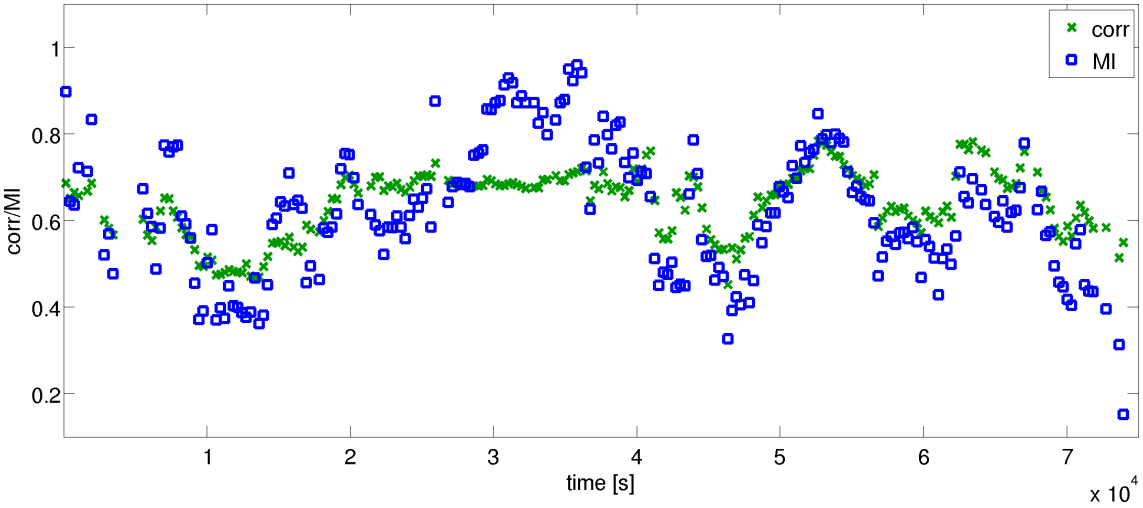

Figure 7.23 The figure presents the correlation and MI coefficients for intervals of 300 000 samples, respectively, between the summed first 5 IMFs (heart and breathing mode) of ABP and ICP of PAT 14. The ordinate denotes the correlation, respectively, MI coefficients and the abscissa time in seconds.

Heartbeat/Breathing Mode: ABP compared to ICP

Now it will be tested, if similar results can be obtained considering the heartbeat, respectively, breathing mode separately. After the decomposition, the whole time series is split up in segments of $N_i = 300\,000$ samples again and for every interval a separation of heartbeat and breathing mode is performed. Since with the condition of the patient also the time series change over time, it cannot be guaranteed that the heartbeat modes are always found in IMFs $1-3$ and the breathing in $4-5$. It is, for example, possible that IMFs $1-2$ suffice to reconstruct the heartbeat

and the breathing is divided into IMFs $3-5$. Therefore, an automatic test is done first to evaluate the single IMFs. The analysis algorithm is based on the FFTs of the individual IMFs in which the highest peak and thus the largest frequency contribution is detected. With the previous knowledge of the heartbeat occurring at around $1-2$ Hz and the breathing at around $0.2-0.3$ Hz, the IMFs can be classified as one or the other via their main oscillation. Afterwards the oscillations belonging to the heartbeat and the ones of the breathing are summed up in two time series.

The correlation and mutual information coefficients between the heartbeat of ABP and ICP are calculated and the correlation and MI of the breathing modes of ABP and ICP likewise. In figure 7.24 and figure 7.25 these coefficients are illustrated.

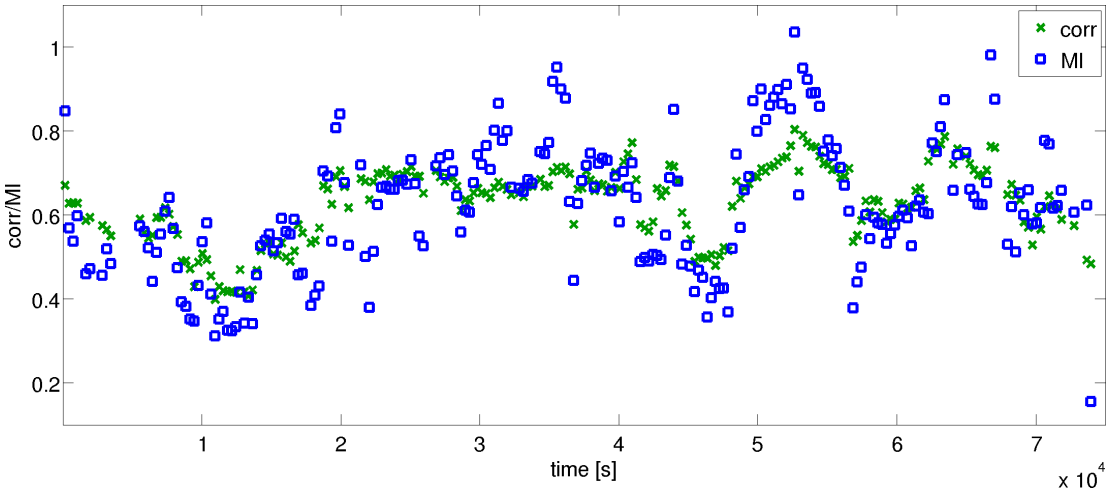

Figure 7.24 The figure presents the correlation and MI coefficients for intervals of 300 000 samples, respectively, between the heartbeat of ABP and ICP of PAT 14. The ordinate denotes the correlation, respectively, MI coefficients and the abscissa time in seconds.

For both analyses the two test methods, correlation and mutual information, are well in accord and exhibit high values universally. Especially for the heartbeat the single coefficients illustrate an almost continuous signal denoting more or less interdependencies between the ABP and ICP. The average correlation of the heartbeat modes amounts to 0.63 and the MI to 0.62. The average correlation of the breathing modes accounts 0.61 and 0.43 for the MI. The coefficients for the breathing mode show a graph which is a little more fuzzy suggesting that the extraction of the heartbeat is more robust.

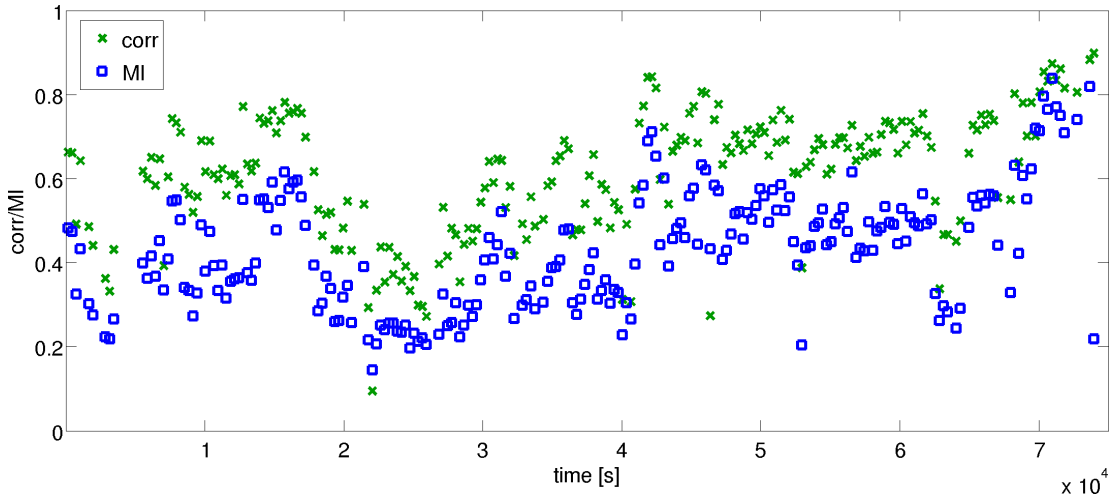

Figure 7.25 The figure presents the correlation and MI coefficients for intervals of 300 000 samples, respectively, between the breathing mode of ABP and ICP of PAT 14. The ordinate denotes the correlation, respectively, MI coefficients and the abscissa time in seconds.

ABP/ICP: Heartbeat compared to Breathing Mode

Finally, the separability of the heartbeat and breathing mode within the ABP, respectively, ICP time series is examined. Again, the heartbeat and breathing mode are separated and for every 300 s interval of the data the correlation and mutual information between the heartbeat and breathing time series of the ABP is computed in order to evaluate, if interdependencies are still present. If not we assume that both time series are independent and the separation was successfully performed with wSEMD. Note that in case of sensor failures the correlation and MI coefficients are set to -1 again.

Figure 7.26 depicts the correlation and mutual information coefficients for the 247 segments of $N_i = 300\,000$ samples of the ABP, presented with respect to the time in seconds. Note that the correlation can adopt negative values and the maximal mutual information is larger than 1. Both, the correlation and MI coefficients, exhibit very small values, especially in contrast to the previous analyses. The correlation values even display a negative correlation of the two time series. The average correlation accounts -0.09 and the mean MI amounts to 0.14. Both methods of evaluation agree in their assessment of the interdependencies of the heartbeat and breathing, since the resulting values run almost completely symmetrically. The coefficients for the ICP time series are equally symmetric and even smaller (c.f. figure 7.27). The mean correlation amounts to -0.05 and the average MI is 0.10.

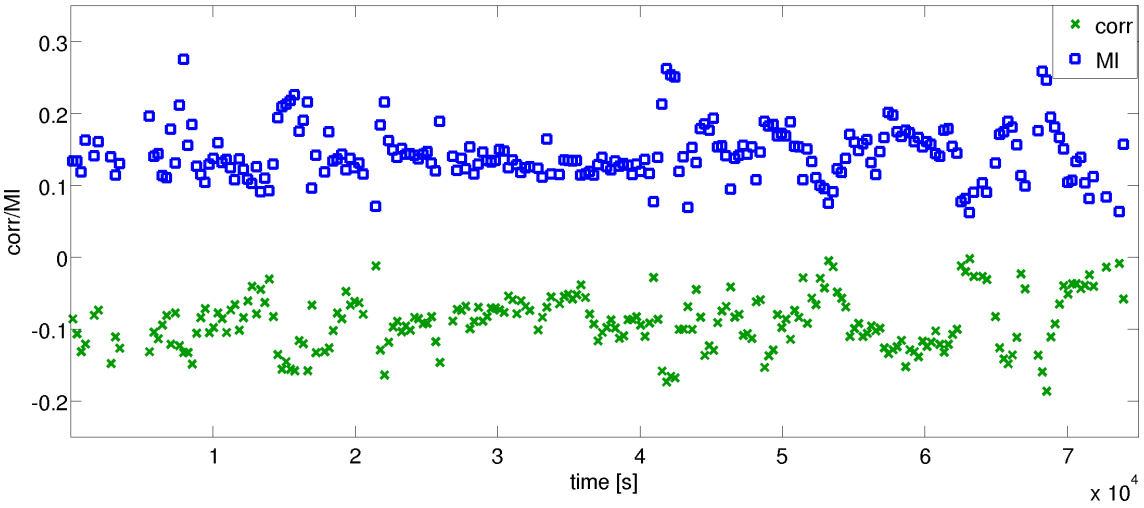

Figure 7.26 The diagram illustrates the correlation and mutual information coefficients for intervals of 300 000 samples (300 s), respectively, between the heartbeat and breathing mode of the ABP of PAT 14. The ordinate denotes the correlation, respectively, MI coefficients and the abscissa time in seconds.

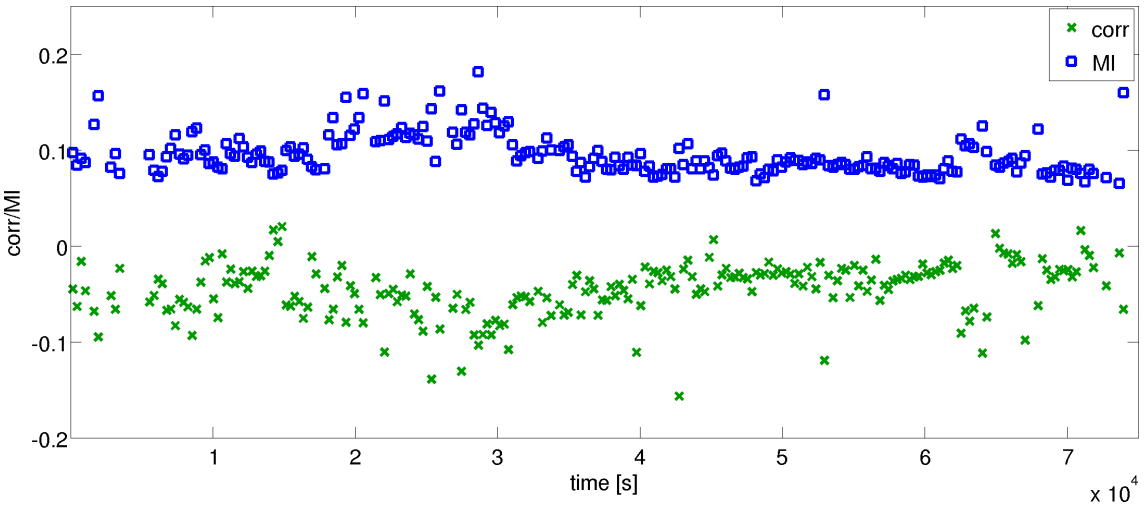

Figure 7.27 The diagram depicts the correlation and mutual information coefficients for intervals of 300 000 samples (300 s), respectively, between the heartbeat and breathing mode of the ICP of PAT 14. The ordinate shows the correlation, respectively, MI coefficients and the abscissa time in seconds.

The deviations from zero may originate from mode mixing in the neuromonitoring data decomposition. However, judging by the FFTs illustrated in figures 7.17 and 7.21 that effect is supposed to be very small. The correlation and MI values may also stem from an amplitude modulation of the heartbeat signal by the breathing

mode. Thus, a closer look on the heartbeat amplitude of the time series will be taken subsequently.

7.7 Examination of the Heartbeat Amplitude

The above detected interdependencies between the heartbeat and breathing mode of the ABP and ICP, respectively, are very small, but still exist. Due to this weak coupling further evaluations concerning the amplitudes are conducted. To be able to examine the developing of the ABP and ICP neuromonitoring time series the amplitude of the heartbeat is selected as parameter to observe. Furthermore, it would be very interesting to find discrepancies between the behavior of the ABP and ICP. Such differences might indicate a change of the state of the patient's brain.

To learn more about the heartbeat a closer look at the IMFs, extracted with wSEMD ($M = 15\,000, K = 300$), is taken. Again, the ABP and ICP of the data set PAT 14 are used after preprocessing with SSA, using a lag parameter of $L = 50$ and 3 eigenvectors to reconstruct the time series. In the following the amplitude of the heartbeat in the ABP and ICP is analyzed thoroughly. Sensor failures are omitted as before in the tests.

The examined amplitude is first presented on a time scale covering every single oscillation period individually and second, averaged over a wider time range, so that one mean amplitude data point is obtained for every 300 s of data.

7.7.1 Amplitude of the Heartbeat Periods

First, the amplitudes of the single heartbeat periods will be examined. On that account, the maximum and minimum of every heartbeat period of the time series is determined. The heartbeat amplitudes A_i of the individual periods are calculated by averaging over the y-values of both minima at the beginning $A(\min_i)$ and end $A(\min_{i+1})$ of a period. Then, this value is subtracted from the y-value of the maximum $A(\max_i)$ located between the two minima and the result is divided by the factor 2:

$$A_i = \frac{1}{2}\left(A(\max_i) - \frac{1}{2}\big(A(\min_i) + A(\min_{i+1})\big)\right) \tag{7.10}$$

This procedure is applied to all heartbeat periods of the ABP and ICP of the data set PAT 14, omitting the sensor failures. Thus, a time series is obtained denoting the changing heartbeat amplitude over time. To be able to compare, this analysis

is conducted for the heartbeat mode alone and additionally for the heartbeat plus the breathing mode. The heartbeat amplitude of the heartbeat plus breathing mode (IMFs 1−5) of the ABP is depicted in figure 7.28 (top trace), and solely the heartbeat mode of the ABP, is presented in figure 7.28 (second trace). Furthermore, the heartbeat amplitude of the heartbeat plus breathing mode of the ICP is illustrated in figure 7.28 (third trace) and additionally only the heartbeat amplitudes of the heartbeat mode of the ICP in figure 7.28 (bottom trace). The temporal resolution amounts to approximately 1 Hz, respectively, the momentary heartbeat frequency. The heartbeat amplitude development over time is fluctuating quite strongly. It changes severely within small amounts of time. Depicted is a total of approximately 21 h of data. Due to the slight mode mixing more outliers are observable, when only the heartbeat mode is taken into account, than when heartbeat and breathing mode (IMFs $1-5$) are considered, which applies particularly for the ICP. However, the general runs of the time series, with and without the breathing mode, are nearly identical. Between the ABP and ICP, differences can be observed, which may indicate a change within the system. Note, for example, the discrepancy between the ABP and ICP at around $5.8 \cdot 10^4$ s. First, the heartbeat amplitude development time series are examined in a detailed view, though.

Figure 7.29 presents a detailed view of the time series of figure 7.28. Again in the top trace the heartbeat plus breathing mode, namely IMFs $1-5$, of the ABP are shown, in the second trace solely the heartbeat mode of ABP is depicted. Presented in the third trace is the heartbeat amplitude development of the heartbeat plus breathing mode of the ICP and in the bottom trace only the heartbeat mode of the ICP is shown. Depicted is the part of the ABP and ICP data, that is also shown in figures 7.16 and 7.17 (ABP) and figures 7.20 and 7.21 (ICP). Note that in those FFTs, no frequency mode mixing is observable.

In figure 7.29 an amplitude modulation is detectable, though. The heartbeat amplitude fluctuates with a period of approximately four heartbeats, since every marker in the graph denotes one beating of the heart. Hence, the frequency of this modulation is about 0.25 Hz, assuming a heartbeat frequency of 1 Hz. This is observable not only for the representation of the heartbeat together with the breathing mode, but also for that of the heartbeat mode alone and for both time series, the ABP and ICP. Although the amplitude modulation is not quite as regular as in traces one and three, traces two and four exhibit the same oscillations. Obviously, after the separation of the heart and breathing mode an amplitude modulation of the latter is still detectable in the heartbeat time series. Judging from the FFTs of both separated signals (see figures 7.17 and 7.21), however, the frequencies are clearly

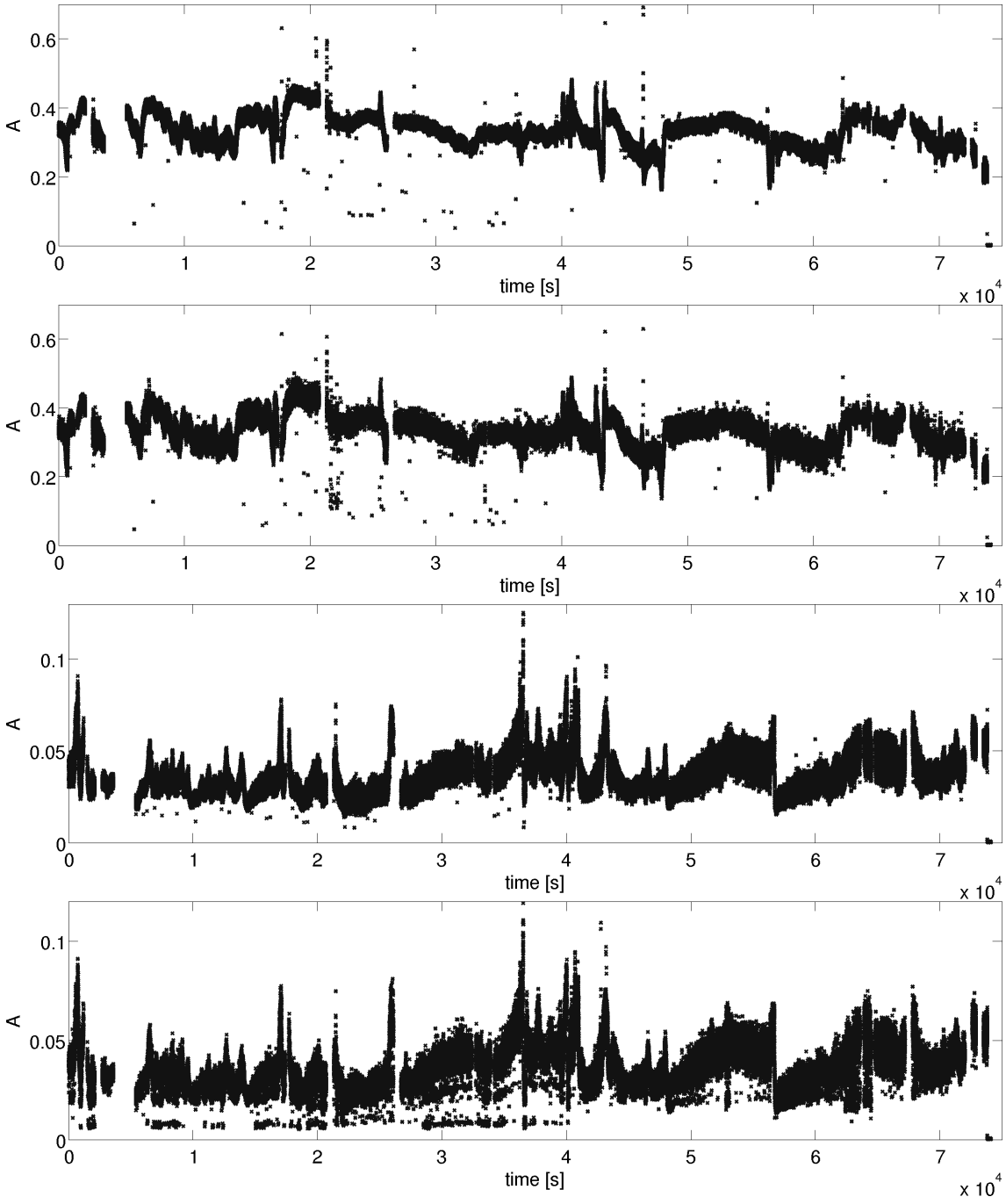

Figure 7.28 The heartbeat amplitude development of the heartbeat plus breathing mode of ABP (top trace), solely the heartbeat mode of ABP (second trace), the heartbeat plus breathing mode of ICP (third trace), and only the heartbeat mode of ICP (bottom trace) are depicted. The ordinate denotes the heartbeat amplitude A and the abscissa time in seconds.

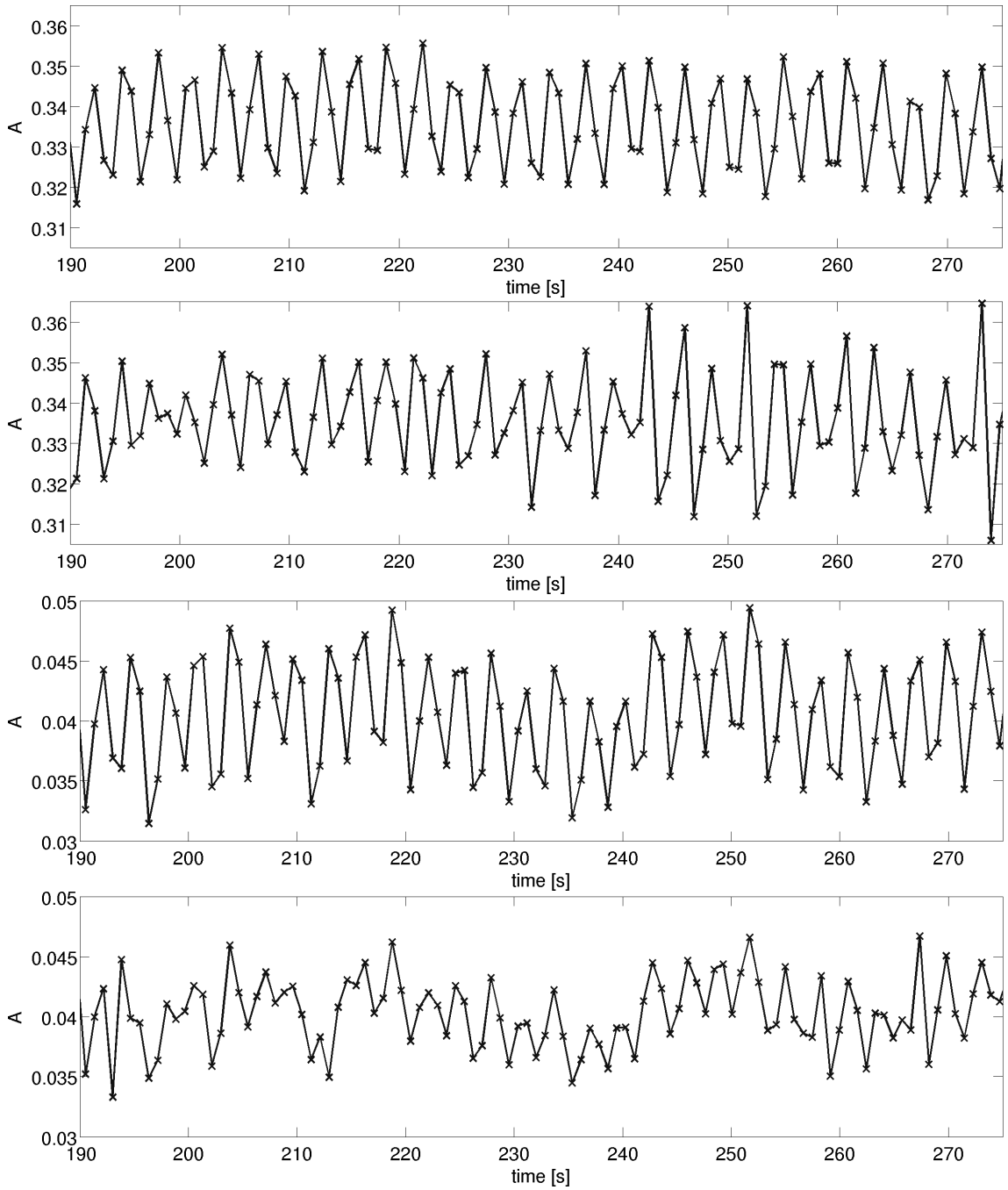

Figure 7.29 A detailed view of the heartbeat amplitude of the heartbeat plus breathing mode of ABP (top trace), solely the heartbeat mode of ABP (second trace), the heartbeat plus breathing mode of ICP (third trace), and only the heartbeat mode of ICP (bottom trace) are depicted. The ordinate denotes the heartbeat amplitude A and the abscissa time in seconds.

decomposed.
Therefore, one can assume that both oscillations, the heartbeat and breathing mode, cannot be completely separated, respectively, are not entirely independent.

7.7.2 Mean Amplitude of the Heartbeat

In order to avoid the influence of the breathing amplitude modulation and to only consider the developing of the heartbeat, its amplitude is examined on a larger time scale now. Therefore, the mean amplitude is computed as described in section 7.4.2 in equation (7.9), which also renders it more robust concerning amplitude outliers in case of slight mode mixing. Thus, every marker in figures 7.30 stands for the mean amplitude of 300 s, respectively, 5 minutes of data. Due to sensor failures some data points are omitted.
Figure 7.30 visualizes the mean amplitude of the extracted heartbeat mode of the ABP and ICP neuromonitoring time series. The mean heartbeat amplitude of the ABP features much higher values than the one of the ICP. Comparing the graphs to figure 7.28 the main characteristics of the curves are maintained, considering the mean amplitude representation. The developing is almost identical for both corresponding graphs, respectively, independent of their different temporal scales, which can be observed for both, the ABP and ICP data. Therefore, no main characteristics are lost via averaging the amplitude values over longer time intervals, whereby the temporal resolution of one data point per 300 s is still very good.

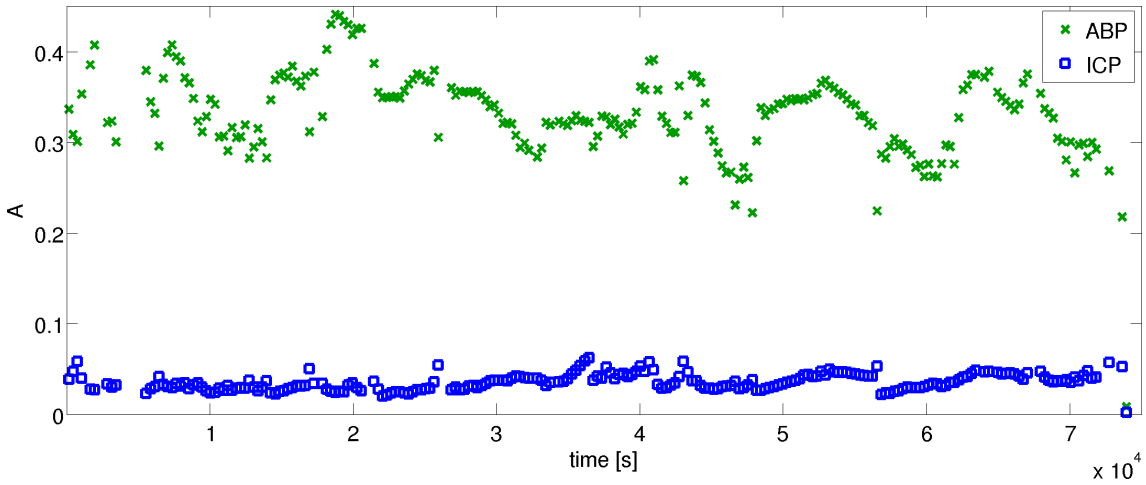

Figure 7.30 The diagram illustrates the mean amplitudes for intervals of 300 s of the heartbeat mode of the ABP and ICP of PAT 14. Intervals with sensor failures are omitted. The ordinate denotes the mean amplitude A and the abscissa time in seconds.

Equal amplitudes of the heartbeat mode in the ABP and ICP cannot be expected, since the damping of the heartbeat amplitude of the ICP with respect to the ABP variations is estimated to be much higher in the brain tissue. However, the variations of the amplitudes of the ABP and ICP in comparison, may comprehend information about the intracranial environment. To be able to observe the characteristics of the data and the developing of the two curves better in contrast, both mean amplitude time series are normalized via subtraction of their mean values and division by their standard deviations (see equation (6.6)).
Figure 7.31 presents the normalized mean amplitudes of the heartbeat mode of the ABP and ICP with a resolution of one data point per 300 s of neuromonitoring time series. Again, in case of the failure of a sensor, the amplitude value is omitted in the figure.

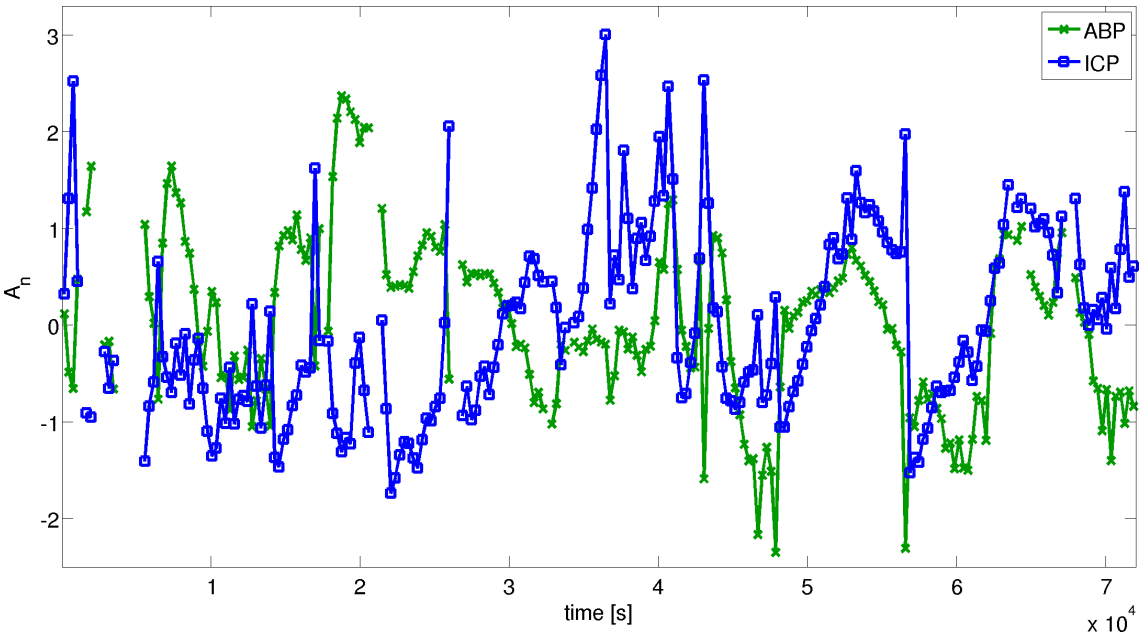

Figure 7.31 The figure depicts the normalized mean amplitudes for intervals of 300 000 samples (300 s) of the heartbeat mode of the ABP and ICP of PAT 14. Segments with sensor failures are omitted. The ordinate denotes the normalized mean amplitude A_n and the abscissa time in seconds.

Several intervals of different behavior are featured in figure 7.31. It is ostentatious, that segments exist, in which both curves run parallel, respectively, antiparallel. Two different very distinct intervals of the graph are observable. Whereas both graphs run in the opposite direction especially at the beginning and in the middle part of the time series, they become parallel towards the end. This behavior could

indicate a severe change within the observed ICP environment, which then alters the pressure transmission through the tissue.
These analyses constitute a first approach to evaluate the pulsatile neuromonitoring data. One has to keep in mind, that a variation of the ABP naturally causes a variation of the ICP. Therefore, it does not suffice to only examine the intracranial pressure, but rather both time series, the ABP input signal and the ICP, simultaneously and in contrast.
Further research could focus on the investigation of different parameters of the system, their developments and their differences between the ABP and ICP time series. However, the interdependencies of the heartbeat and breathing mode has to be taken into account for all analyses to follow.

Chapter 8

Conclusion and Outlook

Biomedical data consist mostly of nonlinear, nonstationary time series, therefore, their analysis is challenging. For the evaluation of brain status data acquired during neuromonitoring, Empirical Mode Decomposition (EMD) was used in this thesis, since EMD is capable of analyzing such complex data. EMD is based on the local properties of the data and thus adaptively decomposes time series into different zero-mean oscillations called Intrinsic Mode Functions (IMFs). Further, the IMFs are defined as functions with only one extremum between two subsequent zero crossings.

The analysis of long time series, recorded for example during neuromonitoring, is challenging. Main memories of conventional computers are not able to deal with such massive amounts of data on an acceptable time scale for practical applications. Furthermore, for the medical care of coma patients in the intensive care unit, it is vital to acquire and process the data in real-time as the results are needed instantly. Hence, in a cooperation with the Department of Neurosurgery of the University Hospital Regensburg the so-called Sliding Empirical Mode Decomposition (SEMD) was developed allowing for an online application of the EMD algorithm. The time series is split up into overlapping segments and then in every window the conventional EMD algorithm is operated, resulting in a large amount of estimates for every sample of the decomposition. The final result is reached via averaging over the ensemble of suggestions for every IMF and the residuum, respectively. The ensemble size E is composed of the quotient of window size M and step size K of the sliding window, yielding $E = M/K$. As practical constraint the number of IMFs and decomposition steps within the EMD algorithm has to be kept constant, which leads to omitting the verification if the IMF criteria are fulfilled. Deviations should, however, be small.

Additionally, an improved version of the method was presented called weighted Sliding Empirical Mode Decomposition (wSEMD), which features an enhanced handling

of the occurring boundary artifacts. A discrete Gaussian distribution is employed as a weighting function in order to suppress the boundary effects strongly and weight the samples near the borders with small values. Equivalently, the estimates for a data point originating from the middle of the windows are multiplied by a large coefficient. Two different techniques to implement the weighting process were compared and evaluated, whereas the approach to weight the particular windows, instead of the estimates, clearly presents the preferable alternative.

With these new algorithms the EMD method is applicable to data via a sliding window technique and is able to process arbitrary quantities of data, which is required for analyzing neuromonitoring time series. Moreover, the (w)SEMD produces very stable results, as it is based on an ensemble of many estimates. In contrast to conventional EMD, the global (w)SEMD residuum may contain oscillations after the decomposition. The local residua of the individual sliding windows still cover only the non-oscillating trends of the time series, when joined to the global residuum they may contain low-frequency oscillations, though. On the other hand this property of wSEMD to supplementary work as a low-pass filter for data sets, can be beneficial for certain applications.

In a next step SEMD and wSEMD were thoroughly tested using toy data. The adherence of the defining criteria of the heuristic EMD algorithm – the completeness and the IMF criteria – were as much seen to, as the influence of the various decomposition parameters, for example the window size and the ensemble size. Moreover, the performance and the computational load of (w)SEMD were surveyed. The tests yielded that the introduced Sliding EMD methods fulfills the IMF criteria, except for small deviations, which also occur for plain EMD. Those deviations emerge due to the practical constraint of keeping the number of sifting steps of the algorithm constant

Additionally, the mode extraction can be regarded numerically accurate, no information loss could be observed applying the algorithm. The reconstruction quality of the toy data using SEMD increases with increasing number of estimates per sample, as anticipated, whereas wSEMD already produces very good results for small ensemble sizes. Moreover, the highest frequency of the oscillations contained in the residuum can be controlled with the window size parameter. The performance of both algorithms, especially of wSEMD, is very good particularly in comparison to other EMD techniques and even conventional EMD. Finally, the investigations yielded that the computational demand increases only linearly with the sample sizes for large amounts of data, in contrast to other EMD techniques. In general both algorithms perform very well, but wSEMD is to be preferred, due to its higher

accuracy in general.
Following that, wSEMD was applied to neuromonitoring data. Correlations within the low-frequency oscillations between the arterial blood pressure (ABP), intracranial pressure (ICP) and partial oxygen pressure in brain tissue (TPO) indicate a severe brain swelling. Therefore, such interdependencies have to be located as early as possible. Such correlation analyses have already been conducted with a method based on Fourier transform in the frequency domain (MTM) in [10], however an observation time of more than 2.8 h is needed to gain information about the time series.
In this thesis the interdependencies between the brain status data were located in the time domain utilizing the Pearson correlation. Thus, wSEMD's property to serve as a low-pass filter was exploited, applying it to neuromonitoring data with a sampling rate of 0.2 Hz. After an appropriate window size was found, the wSEMD method extracted the desired slowly varying oscillations, constituting the homeostasis, into the residuum, which were then analyzed further. At the beginning a significance test was done in order to learn, starting with which correlation coefficient, interdependencies can be regarded significant.
Then, a comparison of the correlation and MTM approaches, both applied in a sliding window technique, was done, applying the same temporal resolution, respectively, window size of ca. 2.8 h of data in both cases. Since the correlation detected more or less the same interdependent segments within the data, plus a few additional ones MTM did not find, a closer look on the latter was taken. It turned out that, although the correlation detects a few more interdependencies than the MTM, this can only be attributed to the conservative estimation of MTM.
Afterwards the temporal resolution of the correlation analyses was increased to a demand of only 1 h of monitoring time, to start the evaluations, which yielded a segment size of 720 samples for the correlation method. This presents an improvement of almost 300 %, in contrast to MTM. Another advantage of the correlation is that the calculation of the Hilbert phase difference is not necessary, since the Pearson correlation automatically distinguishes between a positive and negative correlation.
Finally, wSEMD's property as an online technique of being able to deal with large amounts of data was used to decompose brain status data with a sampling rate of 1 kHz, namely the ABP and the ICP. The neuromonitoring data were preprocessed with Singular Spectrum Analysis (SSA) in each window, in order to remove the noise. Again, the completeness of the decomposition and the compliance of the IMF criteria was successfully tested, except for small aberrations. Additionally, the influence of the ensemble size was examined, approving $E = 50$ as a reasonable

trade-off between precision and computational load for practical applications.

Following the windowed SSA preprocessing and the wSEMD decomposition of the ABP and ICP, their pulsatile components, the heartbeat and breathing mode, were extracted. Automatically the IMFs representing the heartbeat mode were determined and summed up. The same procedure was applied for the breathing mode. Both oscillations could be separated very well concerning their frequency and the whole process functions automatically and online. The correlation between isochronic segments of the heartbeat mode of ABP and ICP and the breathing mode of ABP and ICP were computed over time, which exhibited a large correlation, as expected. In comparison, the correlational analyses between the heartbeat and breathing mode of ABP and ICP, respectively, yielded very low coefficients. However, they were not entirely zero, which was suspected to be caused by an amplitude modulation producing those remaining interdependencies.

Therefore, the neuromonitoring time series were investigated upon, concerning the developing of the heartbeat amplitude over time. The heartbeat mode, extracted with wSEMD, was considered for the analyses. First, this was conducted on a very short time scale, namely the amplitudes of the individual periods of the heartbeat were analyzed. Thereby, the large variability of the heartbeat became apparent. Furthermore, it was observed, that, even though the frequencies of the heartbeat and breathing mode are clearly separable, an amplitude modulation remains on the heartbeat time series, oscillating with the frequency of the breathing mode. Therefore, it is apparent that the heartbeat and breathing mode are not entirely independent.

To avoid the influence of the breathing on the heartbeat amplitude, the mean amplitude of the heartbeat averaged over 300 s, respectively, with respect to time was examined. It was discovered that comparing the developing of the mean amplitudes of the ABP and the ICP, different phases within the behavior of the two time series could be determined. Partly both run antiparallel and in other intervals, they develop parallely, which indicates a change within the underlying system, namely the cerebral environment of the arterial vessels.

The high variability of the ABP naturally causes variations in the ICP. Therefore, both time series always have to be evaluated in comparison. Further research could focus on the examination of different parameters obtained with the neuromonitoring data and screen especially for differences between the behavior of the ABP and ICP, which could indicate a changed ICP environment. However, one has to keep in mind, that the heartbeat and breathing mode are not entirely independent.

All in all the weighted Sliding Empirical Mode Decomposition method constitutes a valuable extension and improvement of the EMD algorithm and proved to be very useful for the application to neuromonitoring data.

Bibliography

[1] J. Sahuquillo. Does multimodality monitoring make a difference in neurocritical care? European Journal of Anaesthesiology, Supplement, 42(Suppl 42), 83–86, 2008.

[2] E. P. S. Neto, M. A. Custaud, C. J. Cejka, P. Abry, J. Frutoso, C. Gharib, and P. Flandrin. Assessment of cardiovascular automatic control by empirical mode decomposition. In 4th Int. Workshop on Biosignal Interpretation, pp. 123–126. 2002.

[3] M.-C. Wu and C.-K. Hu. Empirical mode decomposition and synchrogram approach to cardiorespiratory synchronization. Phys. Rev. E, 73, 051917, 2006.

[4] M.-T. Lo, K. Hu, Y. Liu, C.-K. Peng, and V. Novak. Multimodal pressure-flow analysis: Application of hilbert-huang transform in cerebral blood flow regulation. EURASIP J. Adv. Sig. Proc., 2008.

[5] V. Novak, A. Yang, L. Lepicovsky, A. Goldberger, and L. Lipsitz. Multimodal pressure-flow method to assess dynamics of cerebral autoregulation in stroke and hypertension. Biomedical Engineering Online, 3(39), 2004.

[6] M. Blanco-Velasco, B. Weng, and K. E. Barner. Ecg signal denoising and baseline wander correction based on the empirical mode decomposition. Comput. Biol. Med., 38(1), 1–13, January 2008.

[7] S. Pal and M. Mitra. Empirical mode decomposition based ecg enhancement and qrs detection. Comput. Biol. Med., 42(1), 83–92, January 2012.

[8] M. Böhm. Mathematical modeling of human brain physiological data. Ph.D. thesis, Universität Regensburg, 2011.

[9] A. Jung, R. Faltermeier, R. Rothoer, and A. Brawanski. A mathematical model of cerebral circulation and oxygen supply. J. Math. Biol., 51(5), 491–507, 2005.

[10] R. Faltermeier, M. A. Proescholdt, and A. Brawanski. Computerized data analysis of neuromonitoring parameters identifies patients with reduced cerebral compliance as seen on ct. Acta Neurochir Suppl, 114, 35–38, 2012.

[11] F. Netter. Farbatlanten der Medizin, Band 5, Nervensystem. Georg Thieme Verlag Stuttgart, 1987.

[12] A. Jung. Statistical analysis of biomedical data. Ph.D. thesis, Universität Regensburg, 2003.

[13] N. E. Huang, Z. Shen, S. R. Long, M. L. Wu, H. H. Shih, Q. Zheng, N. C. Yen, C. C. Tung, and H. H. Liu. The empirical mode decomposition and hilbert spectrum for nonlinear and nonstationary time series analysis. Proc. Roy. Soc. London A, 454, 903–995, 1998.

[14] Z. Wu and N. Huang. Ensemble empirical mode decomposition: A noise assisted data analysis method. Advances in Adaptive Data Analysis, 1, 1 – 41, 2009.

[15] G. Rilling, P. Flandrin, and P. Goncalès. On empirical mode decomposition and its algorithms. In Proc. 6th IEEE-EURASIP Workshop on Nonlinear Signal and Image Processing. 2003.

[16] R. Q. Quiroga, J. Arnhold, and P. Grassberger. Learning driver-response relationship from synchronization patterns. Phys. Rev. E, 61, 5142, 2000.

[17] R. Q. Quiroga, A. Kraskov, T. Kreuz, and P. Grassberger. Performance of different synchronization measures in real data: A case study on electroencephalographic signals. Phys. Rev. E, 65, 041903, 2002.

[18] N. E. Hunag and S. S. P. Shen. Hilbert Huang Transform and its Applications. World Scientific Publishing Company, 2005.

[19] N. E. Hunag and N. Attoh-Okine. Hilbert Huang Transform in Engineering. Taylor and Francis Group, 2005.

[20] P. J. Brockwell and R. A. Davis. Time series: theory and methods. Springer-Verlag New York, Inc., New York, NY, USA, 1986.

[21] Z. Wu. `http://rcada.ncu.edu.tw/eemd.m`, visited last December 2012.

[22] G. Rilling and P. Flandrin. On the influence of sampling on the empirical mode decomposition. In Proceedings of IEEE International Conference on Acoustic, Speech and Signal Precessing, ICASSP-06, volume 3, pp. 444–447. 2006.

[23] G. Rilling and P. Flandrin. Sampling effects on the empirical mode decomposition. Advances in Adaptive Data Analysis, 1(1), 43–59, 2009.

[24] P. Flandrin, G. Rilling, and P. Gonçalvès. Empirical mode decomposition as a filter bank. IEEE Signal Processing Lett., 11, 112–114, 2004.

[25] G. Rilling, P. Flandrin, and P. Gonçalvès. Empirical mode decomposition, fractional gaussian noise and hurst exponent estimation. In Proceedings of IEEE International Conference on Acoustic, Speech and Signal Precessing, ICASSP-05. 2005.

[26] Z. Wu and N. Huang. A study of the characteristics of white noise using the empirical mode decomposition method. Proc. Roy. Soc. London, A460, 1597 – 1611, 2004.

[27] G. Rilling and P. Flandrin. One or two frequencies? the empirical mode decomposition answers. IEEE Trans. on Signal Proc., 56(1), 85–95, 2008.

[28] A. Zeiler, R. Faltermeier, I. R. Keck, A. M. Tomé, C. G. Puntonet, and E. W. Lang. Empirical mode decomposition - an introduction. In Proc. IEEE WCCI-IJCNN 2010. IEEE, 2010.

[29] A. Zeiler, R. Faltermeier, M. Böhm, I. R. Keck, A. M. Tomé, C. G. Puntonet, A. Brawanski, and E. W. Lang. Empirical Mode Decomposition Techniques for Biomedical Time Series Analysis, chapter 4, pp. 60–81. Bentham Publishers, 2010.

[30] M. C. Peel, G. G. S. Pegram, and T. A. McMahon. Empirical mode decomposition: improvement and application. In Proc. Int. Congress Modelling Simulation, Vol. 1, pp. 2996 – 3002. Modelling and Simulation Society of Australia, Canberra, 2007.

[31] Y. Washizawa, T. Tanaka, D. P. Mandic, and A. Cichocki. A flexible method for envelope estimation in empirical mode decomposition. In Knowledge-based Intelligent Information and Engineering Systems, Vol. 4253, pp. 1248 – 1255. Springer, Berlin, 2006.

[32] Q. Chen, N. Huang, S. Riemenschneider, and Y. Xu. A b-spline approach for empirical mode decompositions. Adv. Comput. Math., 24(1-4), 171–195, 2006.

[33] Y. Kopsinis and S. McLaughlin. Improved emd using doubly-iterative sifting and high order spline interpolation. EURASIP J. Advances Signal processing, 2008.

[34] Y. Kopsinis and S. McLaughlin. Investigation and performance enhancement of the empirical mode decomposition method based on a heuristic search optimization approach. IEEE Trans.Signal Processing, 56(1), 1 – 13, 2008.

[35] S. Meignen and V. Perrier. A new formulation for empirical mode decomposition based on constrained optimization. IEEE Signal processing Letters, 14, 932 – 935, 2007.

[36] J.-C. Lee, P. S. Huang, T.-M. Tu, and C.-P. Chang. Recognizing human iris by modified empirical mode decomposition. In Adv. Image Video technology, Springer Berlin, volume 4872, pp. 298 – 310. 2007.

[37] F. H. S. Chiew, M. C. Peel, G. E. Amirthanathan, and G. G. S. Pegram. Identification of oscillations in historical global streamflow data using empirical mode decomposition. In Proc. 7th IAHS Scientific Assembly, pp. 53–62. IAHS Publ. 296, 2005.

[38] M. C. Peel, G. E. Amirthanathan, G. G. S. Pegram, T. A. McMahon, and F. H. S. Chiew. Issues with the application of empirical mode decomposition analysis. In MODSIM 2005, Int. Congress Modelling Simulation, A. Zerger and R: M. Argent, eds., pp. 1681–1687. Modelling and Simulation Society of Australia and New zealand, 2005, 2005.

[39] A. Zeiler, R. Faltermeier, A. Tomé, I. Keck, C. Puntonet, A. Brawanski, and E. Lang. Sliding empirical mode decomposition-brain status data analysis and modeling. In P. Georgieva, L. Mihaylova, and L. C. Jain, eds., Advances in Intelligent Signal Processing and Data Mining, volume 410 of *Studies in Computational Intelligence*, pp. 311–349. Springer Berlin Heidelberg, 2013.

[40] Z. Wu, E. Schneider, Z. Hu, and L. Cao. The impact of global warming on enso variability in climate records. Technical report, Center for Ocean-Land-Atmosphere Studies, 110, 25, 2001.

[41] K. Coughlin and K. Tung. 11-year solar cycle in the stratosphere extracted by the empirical mode decomposition method. Advances in Space Research, 34, 323 – 329, 2004.

[42] Z. Wang, A. Maier, N. K. Logothetis, , and H. Liang. Single-trial classification of bistable perception by integrating empirical mode decomposition, clustering, and support vector machine. EURASIP J. Adv. Sig. Proc., 2008.

[43] M.-T. Lo, V. Novak, C.-K. Peng, Y. Liu, and K. Hu. Nonlinear phase interaction between nonstationary signals: A comparison study of methods based on hilbert-huang and fourier transforms. Phys. Rev. E, 79, 061924, 2009.

[44] F. Cong, T. Sipola, T. Huttunen-Scott, X. Xu, T. Ristaniemi, and H. Lyytinen. Hilbert-huang versus morlet wavelet transformation on mismatch negativity of children in uninterrupted sound paradigm. Nonlinear Biomedical Physics, 3, 2009.

[45] Z. Wu, N. E. Huang, and X. Chen. The multi-dimensional ensemble empirical mode decomposition method. Advances in Adaptive Data Analysis, 1(3), 339–372, 2009.

[46] N. Rehman and D. P. Mandic. Multivariate empirical mode decomposition. In Proceedings of the Royal Society A, volume 466, pp. 1291–1302. 2010.

[47] J. Nunes, S. Guyot, and E. Deléchelle. Texture analysis based on local analysis of the bidimensional empirical mode decomposition. Machine Vision and Applications, 16(3), 177–188, 2005.

[48] P. Flandrin, P. Gonçalvès, and G. Rilling. Emd equivalent filter banks: From interpretation to application. In Hilbert-Huang Transform: Introduction and Application, N. Huang and S. Shen, eds., pp. 67 – 87. World Scientific, Singapore, 2005.

[49] P. Flandrin and P. Gonçalvès. Empirical mode decomposition as data-driven wavelet-like expansion. International Journal of Wavelets Multiresolution and Information Processing, 2, 477–496, 2005.

[50] R. N. Meeson. Hilbert Huang Transform and its Applications, chapter HHT Sifting and Adaptive Filtering. World Scientific Publishing Company, 2005.

[51] F. L. Zarraga. On-line extraction of modal characteristics from power system measurements based on hilbert-huang analysis. In Proc. IEEE Conference on Electrical Engineering, Computing Science and Automatic Control 2009, pp. 1–6. 2009.

[52] F. H. Chou and J. C. Huang. Apply pipelining empirical mode decomposition to accelerate an emotionalized speech processing. In Proc. of ICWAPR 2009, pp. 229 – 234. 2009.

[53] N.-F. Chang, T.-C. Chen, C.-Y. Chiang, and L.-G. Chen. On-line empirical mode decomposition biomedical microprocessor for hilbert huang transform. In Biomedical Circuits and Systems Conference (BioCAS), IEEE, pp. 420 – 423. 2011.

[54] M. Hofreiter and P. Trnka. On-line empirical mode decomposition of environmental data. In D. E. T. Dr. Sabahudin Ekinović, Dr. Joan Vivancos Calvet, ed., Proceedings of the International Research/Expert Conference on Trends in the Development of Machinery and Associated Technology, pp. 825–828. 2011.

[55] M.-H. Lee, K.-K. Shyu, P.-L. Lee, C.-M. Huang, and Y.-J. Chiu. Hardware implementation of emd using dsp and fpga for online signal processing. IEEE Transactions on Industrial Electronics, 58(6), 2473 – 2481, 2011.

[56] P. Trnka and M. Hofreiter. The empirical mode decomposition in real-time. In M. Fikar and M. Kvasnica, eds., Proceedings of the 18th International Conference on Process Control, pp. 284–289. Slovak University of Technology in Bratislava, Tatranská Lomnica, Slovakia, 2011.

[57] L. A. Yip. Realtime empirical mode decomposition for intravascular bubble detection, 2010.

[58] A. Zeiler, R. Faltermeier, I. R. Keck, A. M. Tomé, A. Brawanski, C. G. Puntonet, and E. W. Lang. Brain status data analyzed by empirical mode decomposition. In Proc. IEEE WCCI-IJCNN 2010. IEEE, 2010.

[59] R. Faltermeier, A. Zeiler, A. M. Tomé, A. Brawanski, and E. W. Lang. Weighted sliding empirical mode decomposition. Advances in Adaptive Data Analysis, 3(4), 509–526, 2011.

[60] R. Faltermeier, A. Zeiler, I. R. Keck, A. M. Tomé, A. Brawanski, and E. W. Lang. Sliding empirical mode decomposition. In Proc. IEEE WCCI-IJCNN 2010. IEEE, 2010.

[61] A. Zeiler, R. Faltermeier, A. Tomé, C. Puntonet, A. Brawanski, and E. Lang. Weighted sliding empirical mode decomposition for online analysis of biomedical time series. Neural Processing Letters, pp. 1–12, 2012.

[62] P. Flandrin. `http://perso.ens-lyon.fr/patrick.flandrin/emd.html`, visited last December 2012.

[63] A. Zeiler, R. Faltermeier, A. Brawanski, A. M. Tomé, C. G. Puntonet, J. M. Górriz, and E. W. Lang. Brain status data analysis by sliding emd. In LNCS 6687, pp. 77–87. Springer, 2011.

[64] A. Zeiler, R. Faltermeier, A. M. Tomé, C. G. Puntonet, A. Brawanski, and E. W. Lang. Sliding empirical mode decomposition for online analysis of biomedical time series. In LNCS 6691, pp. 299–306. Springer, 2011.

[65] L. Sachs and J. Hedderich. Angewandte Statistik. Methodensammlung mit R. Springer, Berlin, 12., vollst. neu bearb. aufl. edition, 2006.

[66] A. Brawanski, R. Faltermeier, R. D. Rothoerl, and C. Woertgen. Comparison of near-infrared spectroscopy and tissue pO_2 time series in patients after severe head injury and aneurysmal subarachnoid hemorrhage. Journal of Cerebral Blood Flow & Metabolism, 22, 605–611, 2002.

[67] I. T. Jolliffe. Principal Component Analysis. Springer, 2002.

[68] D. Broomhead and G. King. Extracting qualitative dynamics from experimental data. Physica D: Nonlinear Phenomena, 20(2), 217–236, 1986.

[69] D. Broomhead and G. King. On the qualitative analysis of experimental dynamical systems. Nonlinear Phenomena and Chaos, 113, 114, 1986.

[70] N. Golyandina, V. Nekrutkin, and A. Zhigljavsky. Analysis of Time Series Structure: SSA and related techniques. Chapman and Hall/CRC, 2001.

[71] F. J. Alonso. `http://www.mathworks.com/matlabcentral/fileexchange/8115-singular-spectrum-analysis-smoother/content/ssa.m`, visited last December 2012.

[72] J. R. Partington. An Introduction to Hankel Operators. Cambridge University Press, 1988.

[73] W. H. Press, S. A. Teukolsky, W. T. Vetterling, and B. P. Flannery. Numerical recipes in C (2nd ed.): the art of scientific computing. Cambridge University Press, New York, NY, USA, 1992.

[74] T. M. Cover and J. A. Thomas. Elements of Information Theory 2nd Edition (Wiley Series in Telecommunications and Signal Processing). Wiley-Interscience, July 2006.

[75] R. Moddemeijer. `http://www.cs.rug.nl/~rudy/matlab/source/information.m`, visited last December 2012.

Danksagung

An dieser Stelle möchte ich allen herzlich danken, die zum Zustandekommen dieser Arbeit beigetragen haben. Insbesondere:

- Prof. Dr. Elmar Lang für die Bereitstellung dieses Themas, seine ausgezeichnete Betreuung und seine uneingeschränkte Hilfsbereitschaft
- Prof. Dr. Alexander Brawanski für die Zurverfügungstellung der Neuromonitoring Daten, die sehr gute Zusammenarbeit mit der Klinik und Poliklinik für Neurochirurgie des Universitätsklinikums Regensburg und die finanzielle Unterstützung während der Arbeit
- Dr. Rupert Faltermeier für die hervorragende Betreuung der Arbeit, seine Vermittlung zwischen Physik und Medizin und für seine Anmerkungen und Vorschläge
- Prof. Dr. Ana Maria Tomé für die bereichernden Diskussionen und ihre Gastfreundschaft
- Dr. Matthias Böhm und Dr. Dominik Senninger für das Korrekturlesen dieser Arbeit
- Allen Mitgliedern der AG Lang für die angenehme Arbeitsatmosphäre und die tolle Zeit, die ich hier hatte
- Meiner Familie für alles, was sie für mich getan haben und tun
- Dominik für unsere fachlichen Diskussionen bezüglich der Arbeit und seine Unterstützung in jeglicher Hinsicht